SYNTHESIS OF THE POLARIZATION PROPERTIES OF 3C10 AND 3C58 AT 1420 AND 2880 MEGAHERTZ

Thesis by

Kurt Walter Weiler

In Partial Fulfillment of the Requirements

For the Degree of

Doctor of Philosophy

California Institute of Technology

Pasadena, California

1970

(Submitted September 12, 1969)

The stars
That nature hung in Heav'n, and fill'd their
lamps
With everlasting oil, to give due light
To the misled and lonely traveller.

Milton, Comus, 1. 197.

To Sirius,
brightest star of the heavens.

ACKNOWLEDGMENTS

It is impossible to name but a few of the many people to whom I am indebted. First and foremost, I wish to thank G. A. Seielstad for initially recommending this project and then providing invaluable advice and assistance throughout its development. G. J. Stanley, the Director of the Owens Valley Radio Observatory, has been most kind and helpful and the members of both the observatory staff and the Radio Astronomy Department have given much aid and encouragement. Direct assistance with the rather strenuous observing program necessary for the project has been generously provided by K. Chu, G. S. Shostak, Mrs. Carol Walton, and K. B. W. Yip.

I am most grateful for the continued support of a Graduate Research Assistantship from the California Institute of Technology. This research at the Owens Valley Radio Observatory has been supported by the U. S. Office of Naval Research under Contract N00014-67-A-0094-0008.

ABSTRACT

An earth rotation aperture synthesis technique was combined with the methods of interference polarimetry to study the total intensity and polarization properties of the two radio sources 3C10 and 3C58 with a resolution of approximately one minute of arc at both 1420 and 2880 MHz. These data were then used to calculate the spectral index, rotation measure, intrinsic position angle, and depolarization distributions for the two sources. Source models were constructed and estimates obtained for the internal magnetic field strength and relativistic electron density. The origins of the rotation measure and depolarization were studied and estimates of the internal thermal electron density obtained. Attempts were made to compare the present results with the several theories of supernova remnants.

3C10, the remnant of a Type I supernova, in the total radiation is an annular source with a sharp outer edge and little emission from the central regions. The polarized flux density distribution has a similar, but less well defined, ring shape which exhibits a relatively high degree of polarization in many areas. The intrinsic position angle distribution implies a radial component of the magnetic field. 3C58, also believed to be the remnant of a Type I supernova, has a simple shape in the total radiation, brightest in the center and falling off slowly to zero on the edges with an elongation in the east-west direction. The polarized emission shows considerable structure having many areas with relatively high degrees of polarization. The intrinsic position angle distribution implies the existence of a component of the magnetic field lying parallel to the major east-west axis over the full extent of the source.

TABLE OF CONTENTS

CHAPTER I

INTRODUCTION

Since the discovery of polarized radio emission from the Galactic supernova remnant Taurus A by Mayer et al. in 1957 [1] and the detection of polarization in the extragalactic radio source Cygnus A five years later [2], considerable work has been devoted to the measurement and study of the polarization properties of discrete radio sources. These observations have generally been limited to investigating only the integrated properties, since sufficient resolution can be obtained for single antenna studies only if the source is very large or the observing frequency is very high. It is possible to obtain information on smaller sources at lower frequencies through the use of interferometric techniques, but this has been done in only a few cases [3], [4], [5], [6], [7], [8], [9]. In general, detailed two-dimensional studies of the polarization properties of intermediate sized radio sources at decimeter wavelengths are not available.

The most promising means for obtaining such results lie in the earth rotation or "supersynthesis" technique. This method was first applied by O'Brien [10] to the study of the sun, and has been subsequently developed and used to determine radio source structure by Sir Martin Ryle and his colleagues [11], [87], [88], [89]. When combined with the methods of interference polarimetry developed by Morris et al. [12], the technique becomes a powerful tool for investigating the total intensity and polarization properties of cosmic radio sources.

The present work involves the application of these methods to study two radio sources, 3C10 and 3C58, to a resolution of approximately one minute of arc at both 1420 and 2880 MHz. The resulting total intensity and polarization maps are used to determine the spectral index, rotation measure, intrinsic position angle, and depolarization distributions. These are combined with models for the objects to study the physical processes occurring in the sources and in the Galactic medium. Also, comparison of the results with several theories of radio source structure is attempted.

CHAPTER II

MATHEMATICAL TECHNIQUES

Before discussing polarization supersynthesis, one must first develop the methods of two-dimensional synthesis with the Owens Valley interferometer.

Supersynthesis

The response of the Owens Valley Radio Observatory interferometer to an unpolarized radio source has been ably described by Read [13]. Additionally, the possibility for two-dimensional interferometric synthesis has been mentioned by Moffet [14].

Beginning with Moffet's Equation (13) we have

$$\beta'(u,v) = V\, e^{i\Phi} = \frac{\iint T'(x,y)\, e^{i2\pi(ux + vy)}\, dxdy}{\iint T'(x,y)\, dxdy} \qquad (1)$$

where x,y are the distances from an arbitrarily defined origin in the real plane of the sky and u,v are the coordinates in the Fourier transform plane. $\beta'(u,v)$ represents the complex visibility function defined by V and Φ where V is the normalized visibility amplitude and Φ is the phase of the interferometer. Both V and Φ are real quantities. $T'(x,y)$ is the source brightness distribution $T(x,y)$ multiplied by the antenna power pattern. Assuming that the antenna response is approximately constant over the extent of the objects considered here, we can let $T(x,y) \simeq T'(x,y)$.

According to the Rayleigh-Jeans law, flux density and effective temperature are related by $S = 2kT/\lambda^2$, where k is the Boltzmann constant and λ the observing wavelength. Hence

$$\beta'(u,v) = V\, e^{i\Phi} = \frac{\iint S(x,y)\, e^{i2\pi(ux + vy)} dxdy}{\iint S(x,y)\, dxdy} \quad . \tag{2}$$

The integrated flux density observed for a discrete radio source is obviously

$$S = \iint S(x,y)\, dxdy \tag{3}$$

so that we can define an unnormalized complex visibility function $\beta(u,v) = S\, \beta'(u,v) = S\, V\, e^{i\Phi}$. Inverting the transform, the desired result becomes

$$S(x,y) = \int_{-\infty}^{\infty}\int V(u,v)\, e^{i\Phi}\, e^{-i2\pi(ux + vy)}\, dudv \tag{4}$$

where $S(x,y)$ is the flux density distribution across the radio source, $V(u,v) = S\, V$ is the observed unnormalized visibility amplitude, and $\Phi(u,v)$ is the observed visibility phase. Thus it is seen that the brightness distribution is the two-dimensional Fourier transform of the complex visibility function $\beta(u,v)$.

Because a tracking interferometer describes an elliptical path in the Fourier (u,v) plane, it is useful to convert Equation (4) to an elliptical coordinate system. For the general case of an ellipse not centered at the origin

$$\begin{aligned} u &= c\rho + a\rho \cos\Theta \\ v &= d\rho + b\rho \sin\Theta \\ dudv &= \rho(ab + cb\cos\Theta + ad\sin\Theta)\, d\rho\, d\Theta \end{aligned} \tag{5}$$

so that Equation (4) becomes

$$S(x,y) = \int_0^{\infty} \rho \, d\rho \int_0^{2\pi} \beta(\rho,\theta) \, e^{-i2\pi\rho[x(c + a\cos\theta) + y(d + b\sin\theta)]} \times (ab + cb\cos\theta + ad\sin\theta)\, d\theta \qquad (6)$$

Using the property that integration is associative, and measuring angles positive east through north, we can write

$$\int_0^{2\pi} = \underbrace{\int_{-\gamma}^{\gamma} + \int_{\pi-\gamma}^{\pi+\gamma}}_{\text{Region I}} + \underbrace{\int_{\gamma}^{\pi-\gamma} + \int_{\pi+\gamma}^{2\pi-\gamma}}_{\text{Region II}} \qquad (7)$$

or $S(x,y) = S_I(x,y) + S_{II}(x,y)$. These two regions will later be shown to correspond roughly to the areas covered by a tracking interferometer spaced east-west (E/W) and north-south (N/S), respectively.

By employing the relation that

$$\beta(-u,-v) = \beta^*(u,v)$$

or (8)

$$\beta(\rho,\theta+\pi) = \beta^*(\rho,\theta)$$

it can be shown that Region I can be expressed as

$$S_I(x,y) = 2\,\mathrm{Re}\left\{ \int_0^{\infty} \rho \, d\rho \int_{-\gamma}^{\gamma} \beta(\rho,\theta) \, e^{-i2\pi\rho[x(c+a\cos\theta) + y(d+b\sin\theta)]} \times (ab + cb\cos\theta + ad\sin\theta)\, d\theta \right\} \qquad (9)$$

and Region II as

$$S_{II}(x,y) = 2\,\mathrm{Re}\left\{ \int_0^{\infty} \rho\, d\rho \int_{\gamma}^{\pi-\gamma} \beta(\rho,\theta)\, e^{-i2\pi\rho[x(c+a\cos\theta)+ y(d+b\sin\theta)]} \times (ab + cb\cos\theta + ad\sin\theta)\, d\theta \right\} . \quad (10)$$

Considering an interferometer with the antennas arbitrarily placed with respect to one another, it can be shown that

$$\begin{aligned} u &= -s\cos\Delta\sin(h - H) \\ v &= -s\cos\delta\sin\Delta + s\sin\delta\cos\Delta\cos(h - H) \end{aligned} \quad (11)$$

where s is the antenna spacing in wavelengths, h is the hour angle of the source, H is the hour angle of the interferometer pole, δ is the declination of the source, and Δ is the declination of the interferometer pole. In the present set of observations, only two orientations of the interferometer were used: east-west (E/W) ($H = 90^{\circ}$, $\Delta = 0^{\circ}$) and north-south (N/S) ($H = 0^{\circ}$, $\Delta = -52^{\circ}\ 46'\ 06.2'' \equiv \omega$) . Also, because of the physical construction of the antennas, hour angle coverage was limited to the range -4^{h} to $+4^{h}$.

Using the parameters of an E/W and a N/S interferometer in Equation (11) and comparing these with Equation (5), it is obvious that the interferometer tracks on the u,v plane are ellipses with the constants evaluated as follows:

For an E/W interferometer

$$\begin{aligned} a &= 1 & c &= 0 \\ b &= \sin\delta & d &= 0 \\ \rho &= s & \theta &= h \end{aligned} \quad (12)$$

and for a N/S interferometer

$$\begin{aligned} a &= \cos\omega & c &= 0 \\ b &= \sin\delta\cos\omega & d &= -\cos\delta\sin\omega \\ \rho &= s & \Theta &= h + \pi/2 \end{aligned} \qquad (13)$$

The portion of the u,v plane covered during the available hour-angle range is illustrated in Figures 1 and 2. Figure 1, top and bottom, displays the coverage obtained for 3C10 with the spacings used at 1420 MHz (21.1 cm) and 2880 MHz (10.4 cm), respectively. Figure 2 shows the same for 3C58.

Comparison with the areas covered in the two integrals above indicate that we can relate Region I (or Equation 9) to the section of the Fourier plane covered by an E/W tracking interferometer, and Region II (or Equation 10) to that covered by a N/S tracking interferometer. The only provision necessary is that no overlap of the two regions can be allowed. Thus, Region I is extended to the full ± 4 hour limit, and Region II extends only to the point where overlap begins to occur.

For actual use in the reduction of the observational data taken with the Owens Valley interferometer, Equations (9) and (10) must be modified and converted for use on a high-speed computing machine such as the IBM 7094. The necessary changes are described in Chapter IV on data handling.

Interference Polarimetry

The above derivations demonstrate that it is possible to use an interferometer such as exists at Owens Valley to determine the structure of an unpolarized radio emission region. To apply these techniques

Figure 1

Portion of the Fourier (u,v) plane covered for 3C10 with the Owens Valley interferometer.

(a) 1420 MHz; 0 to 1600 ft. E/W in increments of 200 ft.; 0 to 1600 ft. N/S in increments of 200 ft.; X's mark every hour of hour angle; scales in thousands (10^3) of wavelengths.

(b) 2880 MHz; 0 to 800 ft. E/W in increments of 100 ft.; 0 to 800 ft. N/S in increments of 200 ft.; X's mark every hour of hour angle; scales in thousands (10^3) of wavelengths.

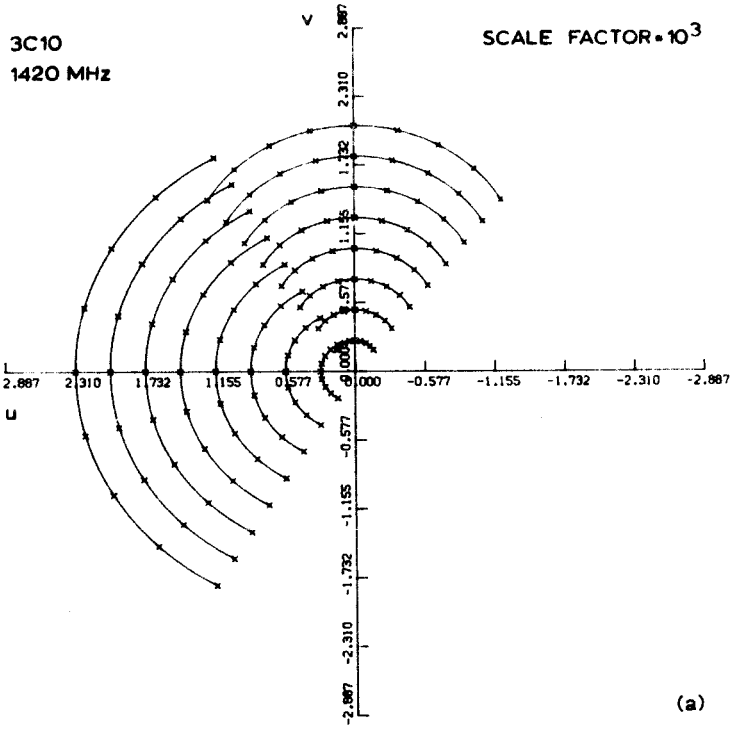
3C10
1420 MHz
SCALE FACTOR = 10^3
v
u
2.887
2.310
1.732
1.155
0.577
0.000
-0.577
-1.155
-1.732
-2.310
-2.887
(a)

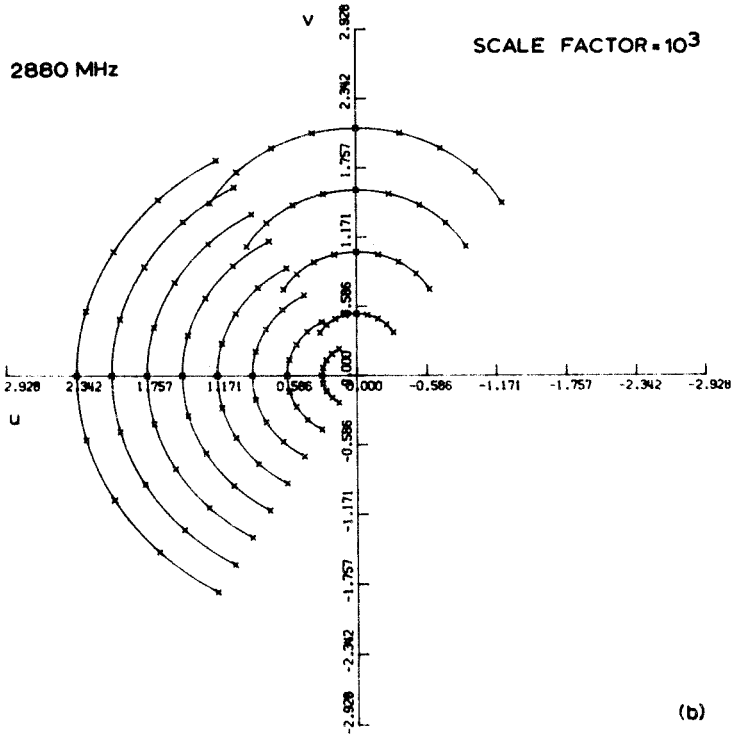
2880 MHz
SCALE FACTOR = 10^3
v
u
2.928
2.342
1.757
1.171
0.586
0.000
-0.586
-1.171
-1.757
-2.342
-2.928
(b)

Figure 2

Portion of the Fourier (u,v) plane covered for 3C58 with the Owens Valley interferometer.

(a) 1420 MHz; 0 to 1600 ft. E/W in increments of 200 ft.; 0 to 1600 ft. N/S in increments of 200 ft.; X's mark every hour of hour angle; scales in thousands (10^3) of wavelengths.

(b) 2880 MHz; 0 to 800 ft. E/W in increments of 100 ft.; 0 to 800 ft. N/S in increments of 200 ft.; X's mark every hour of hour angle; scales in thousands (10^3) of wavelengths.

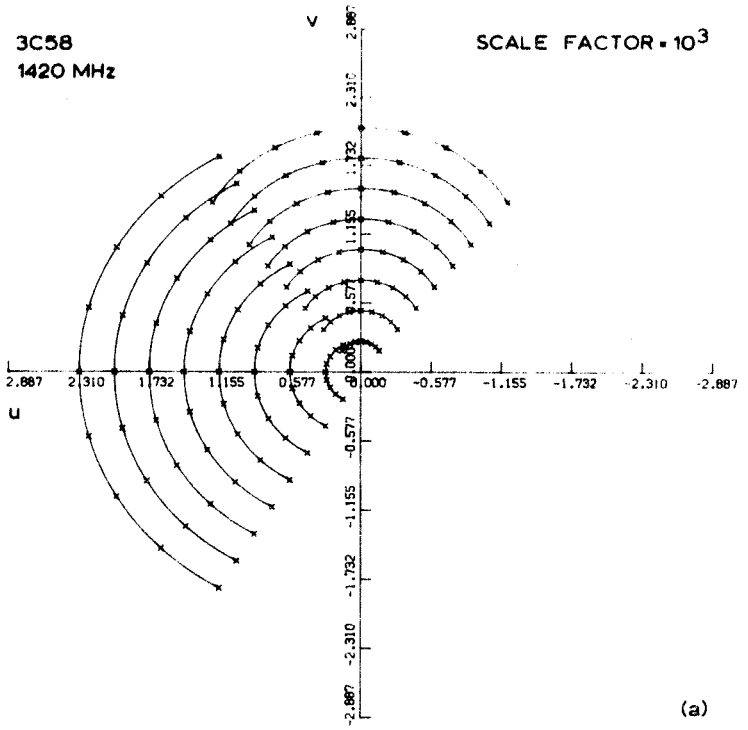
3C58
1420 MHz
SCALE FACTOR = 10^3
v
u
2.887
2.310
1.732
1.155
0.577
0.000
-0.577
-1.155
-1.732
-2.310
-2.887

(a)

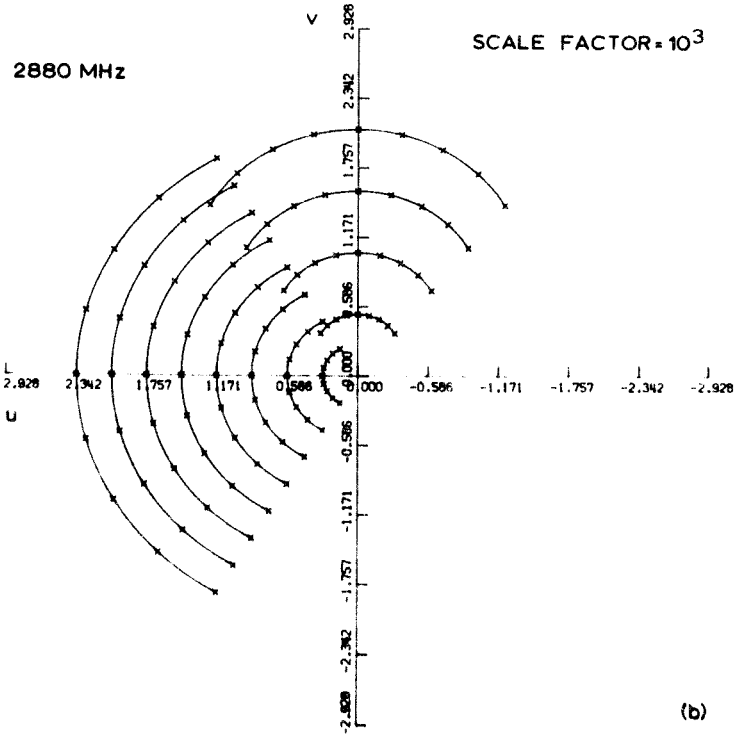
2880 MHz
SCALE FACTOR = 10^3
v
u
2.928
2.342
1.757
1.171
0.586
0.000
-0.586
-1.171
-1.757
-2.342
-2.928

(b)

to the measurement of the distribution of polarized radio radiation, it is possible to employ the methods of interference polarimetry as described by Morris et al. [12]. Starting from Equation (8) in that paper, it is shown that the response of a twin element interferometer with nearly linearly polarized receiving horns is

$$\begin{aligned}\underline{R}(t) = \frac{1}{2}\, k(t)[&\underline{I}\{\cos(\phi_1-\phi_2)\cos(\theta_1-\theta_2)+ i \sin(\phi_1-\phi_2)\sin(\theta_1+\theta_2)\} \\ &+ \underline{Q}\{\cos(\phi_1+\phi_2)\cos(\theta_1+\theta_2)+ i \sin(\phi_1+\phi_2)\sin(\theta_1-\theta_2)\} \\ &+ \underline{U}\{\sin(\phi_1+\phi_2)\cos(\theta_1+\theta_2)- i \cos(\phi_1+\phi_2)\sin(\theta_1-\theta_2)\} \\ &+ \underline{V}\{\cos(\phi_1-\phi_2)\sin(\theta_1+\theta_2)+ i \sin(\phi_1-\phi_2)\cos(\theta_1-\theta_2)\}] \qquad (14)\end{aligned}$$

where the function $k(t)$ describes the characteristic pattern of the interference fringes; $\underline{I}$, $\underline{U}$, $\underline{Q}$, and $\underline{V}$ represent the Fourier transforms of the appropriate Stokes' parameters, e.g.,

$$\underline{I} = \underline{I}(u,v) = \int_{-\infty}^{\infty}\int I(x,y)\, e^{i2\pi(ux + vy)}\, dxdy \quad ; \qquad (15)$$

the angles ϕ and θ represent, respectively, the position angle and ellipticity of the receiving horn; and the numbers 1 and 2 distinguish the two antennas of the interferometer.

The circularly polarized component of the radiation, whose Fourier transform is represented by $\underline{V}$, has been theoretically predicted to be negligibly small [15],[16] or, according to more recent work [17], is likely to be measurable only at low radio frequencies. Additionally, there has as yet been no generally accepted detection of

circular polarization from a cosmic source of continuum radiation. Upper limits to the amount of circular polarization have been placed by a number of observers. Cygnus A has less than 5% at 3.75 meter wavelength [18], less than 4% at 1.9 meter wavelength [19], less than 2% at 3.15 centimeter wavelength [20], and 2 ± 2 percent at 1.55 centimeter wavelength [21]. Mayer et al. [20] have also placed upper limits of 5 percent to the degree of circular polarization of the 3.15 centimeter radiation from Centaurus A and Virgo A. Recently, very low limits to the amount of circular polarization for a large number of radio sources have been set by Seielstad and Weiler [22] at 1418 MHz.

Because of the extended observing time required to synthesize the circularly polarized component of the radiation and because of the evidence indicating that any circular polarization, if present, would be too small to detect, the simplifying assumption was made that $\underline{V} \equiv 0$. Allowing for the possibility of a horn setting error ε and utilizing the information that ε and θ will be small, the following approximations can be used

$$\begin{aligned} &\cos(\theta_1 \pm \theta_2) \simeq 1 \qquad && \sin(\theta_1 \pm \theta_2) \simeq \theta_1 \pm \theta_2 \equiv \theta^{\pm} \\ &\cos \varepsilon \simeq 1 \qquad && \sin \varepsilon \simeq \varepsilon \end{aligned} \tag{16}$$

Employing these assumptions and neglecting all second order terms, the response of the interferometer to polarized radiation becomes

$$\phi_1 = 0 \ , \quad \phi_2 = \varepsilon_o$$

$$\underline{R}_o(t) = \tfrac{1}{2} k(t) \left[\underline{I} + \underline{Q} + \underline{U}\{\varepsilon_o - i\,\theta_o^-\}\right]$$

$$\phi_1 = 0 \ , \quad \phi_2 = 90^\circ + \varepsilon_{90}$$

$$\underline{R}_{90}(t) = -\tfrac{1}{2} k(t) \left[\underline{I}\{\varepsilon_{90} + i\,\theta_{90}^+\} + \underline{Q}\{\varepsilon_{90} - i\,\theta_{90}^-\} - \underline{U}\right] \qquad (17)$$

$$\phi_1 = 45^\circ \ , \quad \phi_2 = 135^\circ + \varepsilon_{135}$$

$$\underline{R}_{135}(t) = -\tfrac{1}{2} k(t) \left[\underline{I}\{\varepsilon_{135} + i\,\theta_{135}^+\} + \underline{Q} + \underline{U}\{\varepsilon_{135} - i\,\theta_{135}^-\}\right] .$$

Since the radio sources in question are only partially polarized ($\sqrt{Q^2 + U^2} < 0.3I$) and since ε and θ are small (see Table IV), $\underline{Q}\{\varepsilon - i\theta^-\}$ and $\underline{U}\{\varepsilon - i\theta^-\}$ can be neglected.

A redefinition of terms will be useful at this point. Since the output of the interferometer is generally given as an amplitude (V) and a phase (Φ) , let

$$\underline{R}_o(t) = \tfrac{1}{2} k(t)\, V_o\, e^{i\Phi_o}$$

$$\underline{R}_{90}(t) = \tfrac{1}{2} k(t)\, V_{90}\, e^{i\Phi_{90}}$$

$$\underline{R}_{135}(t) = \tfrac{1}{2} k(t)\, V_{135}\, e^{i\Phi_{135}} \qquad (18)$$

$$\underline{I} = V_I\, e^{i\Phi_I} \quad , \quad \eta_{90} = \{\varepsilon_{90} + i\theta_{90}^+\}$$

$$\underline{U} = V_U\, e^{i\Phi_U} \quad , \quad \eta_{135} = \{\varepsilon_{135} + i\theta_{135}^+\}$$

$$\underline{Q} = V_Q\, e^{i\Phi_Q} \quad .$$

Substituting into Equations (17) and solving for the quantities of interest in terms of the quantities measured, we have

$$V_I\, e^{i\Phi_I} = \{V_o\, e^{i\Phi_o} + V_{135}\, e^{i\Phi_{135}}\} \,/\, \{1 - \eta_{135}\}$$

$$V_U\, e^{i\Phi_U} = V_{90} e^{i\Phi_{90}} + \{\eta_{90}/(1-\eta_{135})\}\{V_o e^{i\Phi_o} + V_{135} e^{i\Phi_{135}}\} \qquad (19)$$

$$V_Q\, e^{i\Phi_Q} = -\{V_{135} e^{i\Phi_{135}} + \eta_{135} V_o e^{i\Phi_o}\} \,/\, \{1 - \eta_{135}\} \quad .$$

These results, used in Equations (9) and (10), permit the determination of the I, U, and Q distributions across a radio source.

CHAPTER III

OBSERVATIONAL TECHNIQUES

In Chapter II, general equations for the inversion of data from an E/W or N/S tracking interferometer were developed. However, in order to select sources suitable for observation, the parameters of the available observing instrument must be taken into account.

Source Selection

The Owens Valley radio telescope is a correlation-type interferometer consisting of two identical paraboloids of revolution, each ninety feet in diameter and mounted on rails. The railroad tracks allow the two antennas to be separated in an E/W or a N/S direction with spacings varying from 100 feet to 1600 feet. The physical construction of each antenna is such that only the hour angle range between -4 hours and +4 hours can be covered.

Observations at two frequencies were desired to obtain the astrophysical information available from comparing the results. Thus bands near 21 cm and 10 cm were chosen, since dependable crystal mixers and receiving horns already existed for these wavelengths. This choice allowed the specification of one observing frequency at very close to twice the other, gaining certain advantages in the preparation of comparable pictures.

The half power beam width of a single ninety foot antenna is approximately 15 minutes of arc at an observing wavelength of 10 cm, and the maximum resolution obtained with the two antennas separated by 1600 feet at 21 cm observing wavelength is approximately one minute of arc. Thus, definite size limits are imposed on a source useful for

supersynthesis at these two frequencies.

The hour angle at which the E/W and N/S data points begin to overlap in the Fourier plane can be determined from

$$(\tan \omega/\tan \delta) = (\cos(h - h')/\cos h) \qquad (20)$$

where $\omega = -52^{\circ}\ 46'06''.2$, δ is the declination of the source as defined earlier, h is the hour angle E/W, and h' is the hour angle N/S. Given a 4^{h} hour angle limit E/W, the overlap cannot occur for a source with $\delta < -\omega$. Thus, a source must be farther north than 53° in order to obtain complete coverage of the Fourier plane with the Owens Valley interferometer. Finally, for observation of the polarized flux density from the source to be feasible, assuming the usual few percent polarization, a source must have a large (> 5 f.u.*) total flux density (I) at both frequencies.

Summarizing, a suitable source must have the following properties:

(1) Smaller than 10'
(2) Larger than 1'
(3) Far north, preferably $\delta > 53^{\circ}$
(4) I > 5 f.u. at 21 cm and 10 cm
(5) Evidence of polarization.

Sizes were determined mainly from Fomalont [23], and Maltby and Moffet [24]. Accurate positions were obtained from Fomalont [23],

---

* 1 f.u. = 1 flux unit

1 f.u. = 10^{-26} Wm^{-2} Hz^{-1}

Pauliny-Toth et al. (the NRAO catalogue) [25], and the Parkes Catalogues [26], [27], [28]. All 21 cm flux densities and most 10 cm flux densities were obtained from the same references. Additional 10 cm flux densities were obtained from Bartlett [29], Kellermann [30], [31] and Conway et al. [32]. Relevant polarization measurements were found in Seielstad and Wilson [33], Seielstad et al. [34], Morris and Berge [35], Bologna et al. [36], Gardner and Davies [37], Maltby and Seielstad [38], and Sastry et al. [39].

After an extensive search of lists of radio sources and their properties, two objects were found which satisfied the necessary conditions. These were 3C10, a Galactic supernova remnant (Tycho's supernova, S.N. 1572), and 3C58, an unidentified object believed by most observers to also be a Galactic supernova remnant. The properties of these two sources found in the literature are listed in Table I.

TABLE I. Properties of 3C10 and 3C58

Source	3C10	Reference	3C58	Reference
R.A. (1950.0)	$00^h22^m37^s.30$	[23]	$02^h01^m52^s.80$	[23]
Dec. (1950.0)	$+63^\circ51'42''.0$	[23]	$+64^\circ35'14''.0$	[23]
Component 21 cm flux	43.5 f.u.	[23]	34.2 f.u.	[23]
Component E/W Diameter	7'.2	[23]	4'.6	[23]
Flux Density (f.u.)	43.5(1425 MHz) 29.0(3200 MHz)	[23] [32]	34.2(1425 MHz) 33.5(3200 MHz) 28.1(2695 MHz) 27.6(2840 MHz)	[23] [32] [30] [29]
% Polarization	1.1±0.2(21.2 cm) 0.7±0.4(21.2 cm)	[35] [36]	0.8±0.6(21.2 cm) 6.7±0.1(6 cm)	[36] [39]

Study of the E/W brightness distribution work of Fomalont [23] and use of unpublished N/S brightness distribution results by Fomalont [40] yielded an estimate of the maximum source dimensions. These are shown in Table II.

TABLE II. Approximate Source Dimensions

Source	Size E/W	Size N/S
3C10	9'.5	9'.5
3C58	11'.3	5'.5

Bracewell [41] has demonstrated that the source brightness distribution is uniquely determined by the values of $\beta(u,v)$ at a lattice of points such that

$$\Delta u \leq 3437.75/(\text{diameter E/W in minutes of arc})$$
$$\Delta v \leq 3437.75/(\text{diameter N/S in minutes of arc}) \quad . \tag{21}$$

Solving this for the sizes given in Table II yields

$$\Delta u_{max}(3C10) = 362\lambda \qquad \Delta u_{max}(3C58) = 304\lambda$$
$$\Delta v_{max}(3C10) = 362\lambda \qquad \Delta v_{max}(3C58) = 625\lambda \quad . \tag{22}$$

For the Owens Valley interferometer, antenna spacings of 200 feet at 21 cm and 100 feet at 10 cm are approximately equal to 288λ . Thus, choosing the observing frequencies of 1420.0 MHz (21.1 cm) and 2880.0 MHz (10.4 cm), it is possible to synthesize 3C10 and 3C58 to a resolution of approximately one minute of arc by using antenna spacings both E/W and N/S of 200 feet to 1600 feet in increments of 200 feet at 21.1 cm and spacings of 100 feet to 800 feet in increments of 100 feet

at 10.4 cm. In practice, a lack of 100 ft. increments N/S will have detrimental effects to be discussed later.

Horn Calibration

In order to determine the polarization properties of the antennas we refer once again to Equation (17). Employing the same notation and approximations, for totally unpolarized radiation ($\underline{U} = \underline{Q} = \underline{V} \equiv 0$) the response of the interferometer becomes

$$\begin{aligned}
&\phi_1 = 0 \ , \quad \phi_2 = \varepsilon_o \\
&\underline{R}_o(t) = \tfrac{1}{2}\, k(t)\, \underline{I} \\
&\phi_1 = 0 \ , \quad \phi_2 = 90^o + \varepsilon_{90} \\
&\underline{R}_{90}(t) = -\tfrac{1}{2}\, k(t)\, \underline{I}\{\varepsilon_{90} + i\, \theta^+_{90}\} \\
&\phi_1 = 45^o \ , \quad \phi_2 = 135^o + \varepsilon_{135} \\
&\underline{R}_{135}(t) = -\tfrac{1}{2}\, k(t)\, \underline{I}\{\varepsilon_{135} + i\, \theta^+_{135}\} \quad .
\end{aligned} \tag{23}$$

With the definitions of Equation (18), solving for the unknown antenna parameters ε, θ^+ yields

$$\begin{aligned}
\varepsilon_{90,135} &= -\frac{V_{90,135}}{V_o} \cos(\Phi_{90,135} - \Phi_o) \\
\theta^+_{90,135} &= \theta_1 + \theta_2 = -\frac{V_{90,135}}{V_o} \sin(\Phi_{90,135} - \Phi_o) \quad .
\end{aligned} \tag{24}$$

Thus, by observing totally unpolarized radio sources, the instrumental corrections can be determined.

The list of horn calibration sources which are known to have little polarization at the frequencies under study or are thought to

be unpolarized for theoretical reasons is shown in Table III.

TABLE III. Unpolarized Horn Calibrators

Source	R.A. (1950.0) h m s	Dec. (1950.0) o ' "
3C123	04 33 55.3	29 34 13
Orion A	05 32 51.0	-05 25 00
3C147	05 38 43.5	49 49 43
Hydra A	09 15 41.3	-11 53 00
3C295	14 09 33.4	52 26 14
CTB52	18 17 40.0	-16 12 04
Cygnus A	19 57 44.5	40 30 02
Cassiopeia A	23 21 12.6	58 32 45

It is desirable to observe with the receiving horns alternating between the three positions ϕ_1/ϕ_2 of 0/0, 0/90, and 45/135. However, as with any instrument, horn construction errors, beam shape effects, and reflector defects cause the horn indicators to differ from their effective positions. As can be seen from Equation (17), a small horn setting error has little effect for parallel horns (0/0) so that calibration of this setting is not necessary. However, when the horns are crossed (0/90 or 45/135) a small setting error may be of considerable consequence so that it is useful to find the horn settings as accurately as possible initially. Thus the project commenced with observations of the unpolarized horn calibrators to determine the crossed horn positions and their hour angle and declination dependence. The hour angle dependence was small (see Errors section) and was neglected. The correct settings for 3C10 and 3C58 were determined from a straight line fit for the declination dependence.

At the conclusion of the observing project, to determine ε and θ^+ accurately, the unpolarized sources were again observed with the horns set at the calibrated positions. These values, which are shown in Table IV, were used to correct the observational data by Equations (19).

TABLE IV. Instrumental Corrections

Source	Wavelength (cm)	Horn Position ϕ_1/ϕ_2	ε (rad)	θ^+ (rad)
All spacings except 200 ft. E/W				
3C10 U	21.1	0/90.03	$0.00*10^{-3}$	$-1.44*10^{-3}$
3C10 Q	21.1	45/134.72	$2.79*10^{-3}$	$1.48*10^{-3}$
3C10 U	10.4	0/92.14	$1.57*10^{-3}$	$-6.04*10^{-3}$
3C10 Q	10.4	45/136.93	$1.05*10^{-3}$	$3.89*10^{-3}$
3C58 U	21.1	0/90.03	$0.00*10^{-3}$	$-1.45*10^{-3}$
3C58 Q	21.1	45/134.72	$2.79*10^{-3}$	$1.50*10^{-3}$
3C58 U	10.4	0/92.14	$1.40*10^{-3}$	$-6.03*10^{-3}$
3C58 Q	10.4	45/136.93	$1.05*10^{-3}$	$3.90*10^{-3}$
200 ft. E/W only				
3C10 U	21.1	0/90.15	$2.09*10^{-3}$	$-1.44*10^{-3}$
3C10 Q	21.1	45/134.87	$5.41*10^{-3}$	$1.48*10^{-3}$
3C10 U	10.4	0/92.08	$5.24*10^{-4}$	$-6.04*10^{-3}$
3C10 Q	10.4	45/136.43	$-7.68*10^{-3}$	$3.89*10^{-3}$
3C58 U	21.1	0/90.15	$2.09*10^{-3}$	$-1.45*10^{-3}$
3C58 Q	21.1	45/134.87	$5.41*10^{-3}$	$1.50*10^{-3}$
3C58 U	10.4	0/92.08	$3.49*10^{-4}$	$-6.03*10^{-3}$
3C58 Q	10.4	45/136.43	$-7.68*10^{-3}$	$3.90*10^{-3}$

Observations

An excellent discussion of the methods of calibration of the Owens Valley antenna system with respect to pointing errors, baseline position and gain and phase stability is given by Fomalont [42]. Similar methods were employed throughout this observing program.

The actual sequence of observations is shown in Table V.

TABLE V. Sequence of Observations

Spacing (feet)	Direction	Freq. (MHz)	Date Start	Date End	Program
200	E/W	1420	07/24/67	07/27/67	Horn Calibration
200	E/W	1420	07/27/67	07/30/67	Synthesis
200	E/W	2880	07/30/67	08/03/67	Horn Calibration
200	E/W	2880	08/03/67	08/07/67	Synthesis
100	E/W	1420	09/26/67	10/01/67	Horn Calibration
100	E/W	2880	10/01/67	10/05/67	Horn Calibration
100	E/W	2880	02/01/68	02/03/68	Synthesis
100	E/W	1420	02/03/68	02/05/68	Synthesis
1600	E/W	1420	02/05/68	02/09/68	Synthesis
800	E/W	1420	02/09/68	02/11/68	Synthesis
800	E/W	2880	02/11/68	02/14/68	Synthesis
400	E/W	2880	02/14/68	02/17/68	Synthesis
400	E/W	1420	02/17/68	02/19/68	Synthesis
1200	E/W	1420	02/19/68	02/22/68	Synthesis
200	N/S	2880	04/21/68	04/24/68	Synthesis
200	N/S	1420	04/24/68	04/26/68	Synthesis
400	N/S	1420	04/26/68	04/28/68	Synthesis
400	N/S	2880	04/28/68	05/01/68	Synthesis
800	N/S	2880	05/01/68	05/04/68	Synthesis
800	N/S	1420	05/04/68	05/07/68	Synthesis
1600	N/S	1420	05/07/68	05/10/68	Synthesis
600	E/W	1420	08/02/68	08/04/68	Synthesis
600	E/W	2880	08/04/68	08/07/68	Synthesis
300	E/W	2880	08/07/68	08/09/68	Synthesis
700	E/W	2880	08/09/68	08/12/68	Synthesis
1000	E/W	1420	08/12/68	08/14/68	Synthesis
1400	N/S	1420	08/14/68	08/16/68	Synthesis
600	N/S	1420	08/16/68	08/18/68	Synthesis
600	N/S	2880	08/18/68	08/21/68	Synthesis
1400	E/W	1420	09/03/68	09/06/68	Synthesis
100	E/W	1420	09/06/68	09/08/68	Horn Calibration
100	E/W	2880	09/08/68	09/10/68	Horn Calibration

At each frequency and each spacing data were collected for the two sources over the entire available hour angle range, using a four-minute integration time for the I measurement and ten-minute integration times for both the U and Q measurements.

At the time of observation the data were digitized and recorded on magnetic tape. Subsequently, the magnetic tape was reduced to calibrated amplitudes and phases on an IBM 7094 computer with the aid of reduction programs prepared by D. H. Rogstad and J. F. Bartlett.

CHAPTER IV

DATA ANALYSIS

With the data in the form of amplitudes and phases distributed over the Fourier plane, it was necessary to interpolate to a regular array of points, apply the instrumental polarization corrections, and perform the inversion.

Interpolation

It should be noted that the amplitude (V) and phase (Φ) which are obtained as data are not continuous functions. Thus, the interpolation over hour angle was applied to the two Cartesian components $V*\sin(\Phi)$ and $V*\cos(\Phi)$, which are known to be continuous, and the results reconverted to amplitude and phase.

Because it had been decided to perform the inversion in the elliptical coordinate frame defined by the interferometer, for each spacing observed only a one-dimensional interpolation was necessary to obtain the amplitude and phase at a series of points regularly spaced in hour angle. A smoothing technique employing an average of the nearby data points each weighted exponentially according to its distance was used for this purpose. This method serves well for a high density of data points and also allows control of the amount of smoothing simply by varying the decay length of the exponential weighting function. Unfortunately, it can be shown that a function of this type gives a poor representation of the data when the point density is low. To improve the results in this latter case, a pseudo data point linearly interpolated between the last two real data points is included in the weighted average with a weight of 0.5. Thus, when the data points

become sparse the interpolation effectively becomes linear. This provision also prevents sharp discontinuities in the interpolated curve. Once the smoothed curve is defined as an array of closely spaced points in hour angle, output values at any hour angle are determined by linear interpolation between the nearest array elements.

Shown in Table VI are the parameters used for interpolation of the data. Columns 1, 2, and 3 contain the source name, the observing frequency in MHz, the spacing in feet and the baseline orientation. Column 4 specifies the number of samples taken from the interpolated curve. Column 5 contains the limit to the hour angle region of interest which along with the number of samples completely specifies column 6, the time interval between consecutive samples. The last column is the interval (τ) in hours to the 1/e point of the exponential weighting function.

The maximum interval between samples for complete definition of an object is determined by the Bracewell criterion, so that samples in hour angle must be taken at least as often as indicated in Equations (22). Some redundancy of the information is desirable, so the sample interval was chosen to be 20 minutes of hour angle at the maximum spacing E/W and N/S for both sources at both frequencies. This is an interval of roughly 180λ . Since the highest frequency component present in the data decreases with the spacing, the sampling rate was decreased for the smaller spacings in order to shorten the computing time required for inversion. The exponential decay length (τ) was chosen empirically to yield the best fit of the smoothed curve to the data points.

TABLE VI. Interpolation Parameters

Source	Freq. (MHz)	Spacing (feet)	No. of Samples	H.A. Limit (hours)	Sample Interval (minutes)	Tau (hours)
3C10	1420	200 E/W	7	4.00	80.00	0.60
3C10	1420	400 E/W	9	4.00	60.00	0.40
3C10	1420	600 E/W	11	4.00	48.00	0.30
3C10	1420	800 E/W	15	4.00	34.29	0.30
3C10	1420	1000 E/W	17	4.00	30.00	0.24
3C10	1420	1200 E/W	19	4.00	26.67	0.20
3C10	1420	1400 E/W	23	4.00	21.82	0.17
3C10	1420	1600 E/W	25	4.00	20.00	0.15
3C10	1420	200 N/S	5	3.26	97.67	0.60
3C10	1420	400 N/S	7	3.26	65.12	0.49
3C10	1420	600 N/S	9	3.26	48.84	0.49
3C10	1420	800 N/S	13	3.26	32.56	0.33
3C10	1420	1000 N/S	7	3.26	65.12	0.33
3C10	1420	1200 N/S	9	3.26	48.84	0.24
3C10	1420	1400 N/S	19	3.26	21.71	0.20
3C10	1420	1600 N/S	21	3.26	19.53	0.20
3C10	2880	100 E/W	7	4.00	80.00	0.60
3C10	2880	200 E/W	9	4.00	60.00	0.40
3C10	2880	300 E/W	11	4.00	48.00	0.30
3C10	2880	400 E/W	15	4.00	34.29	0.30
3C10	2880	500 E/W	17	4.00	30.00	0.24
3C10	2880	600 E/W	19	4.00	26.67	0.20
3C10	2880	700 E/W	23	4.00	21.82	0.17
3C10	2880	800 E/W	25	4.00	20.00	0.15
3C10	2880	200 N/S	9	3.26	48.84	0.49
3C10	2880	400 N/S	13	3.26	32.56	0.33
3C10	2880	600 N/S	17	3.26	24.42	0.24
3C10	2880	800 N/S	21	3.26	19.53	0.20

TABLE VI (continued)

Source	Freq. (MHz)	Spacing (feet)	No. of Samples	H.A. Limit (hours)	Sample Interval (minutes)	Tau (hours)
3C58	1420	200 E/W	7	4.00	80.00	0.48
3C58	1420	400 E/W	9	4.00	60.00	0.32
3C58	1420	600 E/W	11	4.00	48.00	0.24
3C58	1420	800 E/W	15	4.00	34.29	0.24
3C58	1420	1000 E/W	17	4.00	30.00	0.19
3C58	1420	1200 E/W	19	4.00	26.67	0.16
3C58	1420	1400 E/W	23	4.00	21.82	0.14
3C58	1420	1600 E/W	25	4.00	20.00	0.12
3C58	1420	200 N/S	5	3.21	96.43	0.77
3C58	1420	400 N/S	7	3.21	64.29	0.39
3C58	1420	600 N/S	9	3.21	48.22	0.39
3C58	1420	800 N/S	11	3.21	38.57	0.26
3C58	1420	1000 N/S	7	3.21	64.29	0.26
3C58	1420	1200 N/S	9	3.21	48.22	0.19
3C58	1420	1400 N/S	19	3.21	21.43	0.15
3C58	1420	1600 N/S	21	3.21	19.29	0.15
3C58	2880	100 E/W	7	4.00	80.00	0.48
3C58	2880	200 E/W	9	4.00	60.00	0.32
3C58	2880	300 E/W	11	4.00	48.00	0.24
3C58	2880	400 E/W	15	4.00	34.29	0.24
3C58	2880	500 E/W	17	4.00	30.00	0.19
3C58	2880	600 E/W	19	4.00	26.67	0.16
3C58	2880	700 E/W	23	4.00	21.82	0.14
3C58	2880	800 E/W	25	4.00	20.00	0.12
3C58	2880	200 N/S	9	3.21	48.22	0.39
3C58	2880	400 N/S	13	3.21	32.14	0.26
3C58	2880	600 N/S	17	3.21	24.11	0.19
3C58	2880	800 N/S	21	3.21	19.29	0.15

In addition to the hour angle interpolations, it was necessary to determine the values for three spacings which were impossible to obtain with the interferometer. These were 500 feet E/W at 10.4 cm, and 1000 feet N/S and 1200 feet N/S at 21.1 cm. The two spacings smaller and the two spacings larger than the unknown were interpolated in hour angle and the results calculated at the interval proper for the missing spacing. For each hour angle, the sine and cosine components were plotted and a curve hand drawn through the four points to obtain an interpolated value. This same process was repeated for each hour angle for each missed spacing.

Instrumental Correction

Having obtained a grid of values in the Fourier plane with the different parameters of each source calculated for the same u,v points, it is possible to use Equations (19) to correct the measured values for instrumental effects and solve for the Fourier transforms of the Stokes' parameters I, U, Q. This was done and an array of points for each parameter obtained for each source at both observing frequencies.

Inversion

To perform the inversion, Equations (9) and (10) were modified to the form

$$S(x,y) = 2 \int_0^R \rho \, d\rho \int_{h_1}^{h_2} V(\rho,\theta)\cos[2\pi\rho\{x(c+a\cos\theta)+ y(d+b\sin\theta)\} - \Phi](ab + cb\cos\theta + ad\sin\theta)\, d\theta \quad . \qquad (25)$$

For the E/W case the constants are defined by Equation (12), R is the maximum spacing E/W, and h_1 and h_2 are -4^h and $+4^h$ of hour angle, respectively. For the N/S case the constants are defined by Equation (13), R is the maximum spacing N/S, and h_1 and h_2 are $\pi/2$ minus and $\pi/2$ plus the maximum hour angle before overlap with the E/W data.

After performing the integration in θ by Simpson's rule, the integration in ρ was computed as a sum of the values for the individual spacings each weighted according to its area on the u,v plane. The zero spacing fluxes used are shown in Table VII.

TABLE VII. Zero Spacing Fluxes

Source	21.1 cm Flux Density (f.u.)	Ref.	10.4 cm Flux Density (f.u.)	Ref.
3C10 I	43.5	[23]	28.2	[46]
3C10 U	-0.30	[36]	-0.22	--
3C10 Q	0.04	[36]	-0.13	--
3C58 I	34.2	[23]	30.2	[46]
3C58 U	-0.12	[36]	-1.43	--
3C58 Q	0.25	[36]	-0.22	--

The fluxes for which no reference is given are interpolations from the polarization results of other observers [36], [39], [47], [48], [49]. Although these estimates are uncertain at best, the zero spacing flux density is merely a level shift of the whole matrix, having little effect on the detailed source structure.

The two matrices resulting from the N/S and E/W integrations were then superposed point by point to obtain the final map of the radio source on the plane of the sky.

Before inversion, the option was available to weight the data radially with an elliptical Gaussian to attenuate the deleterious effects of artificially terminating the ρ integration. This has the effect of convolving the source with an elliptical Gaussian (see Bracewell [43]). All inversions shown here have been smoothed by convolution with an elliptical Gaussian having full width at half maximum of 0.'70 E/W and 0.'80 N/S.

In order to study the results of this inversion method, the response of the synthesized array to a point source ($V = 1$, $\Phi = 0$ $\forall$ u,v) was calculated. This is shown in Figures 3 through 6. The top drawing in each case demonstrates the response over an area 20' by 20' and the lower drawing the more detailed response over an area 10' by 10'. In Figures 3 and 4 the areas are centered at the position of 3C10 and illustrate the results at 21.1 and 10.4 cm, respectively. Figures 5 and 6 show the same for the position of 3C58. These maps indicate the distortion which will affect the final pictures of the radio sources.

The inversion of the data produced maps of the Stokes' parameters I, U, Q for both 3C10 and 3C58 at 21.1 and 10.4 cm. These were completed in squares 10' on a side with a point every 0.'25, yielding a 41×41 output matrix. From these results, the polarized flux density ($\sqrt{U^2 + Q^2}$) and the position angle ($\frac{1}{2} \tan^{-1}(U/Q)$) distributions were calculated.

Figure 3

Response of the synthesized array at 1420 MHz to a point source at the declination of 3C10.

(a) 20' by 20' area; contour interval of 1; peak value of 10.

(b) 10' by 10' area; Half Power Beam Width contour darkened; contour interval of 1; peak value of 10.

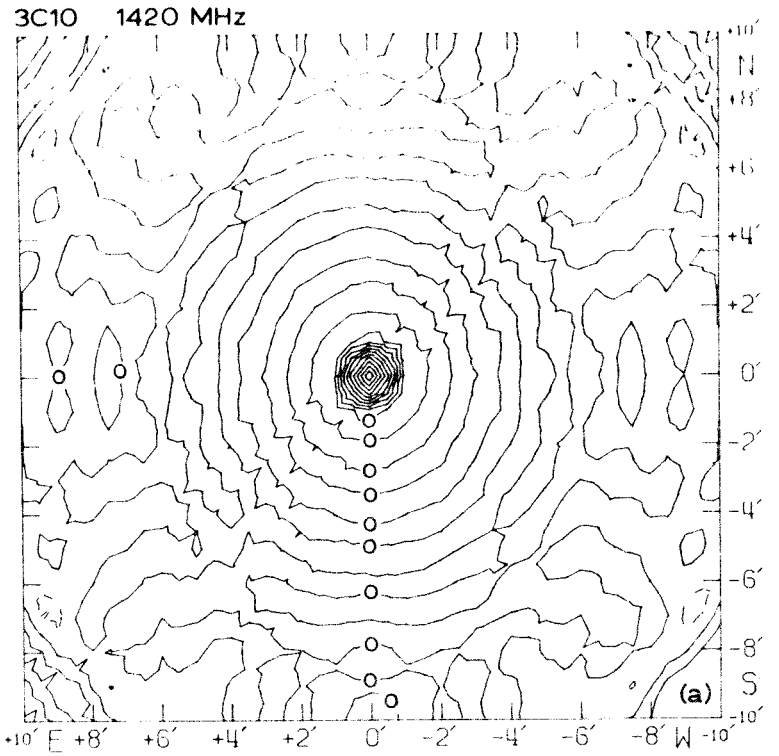
3C10 1420 MHz
+10′ N +8′ +6′ +4′ +2′ 0′ -2′ -4′ -6′ -8′ S -10′
+10′ E +8′ +6′ +4′ +2′ 0′ -2′ -4′ -6′ -8′ W -10′
(a)

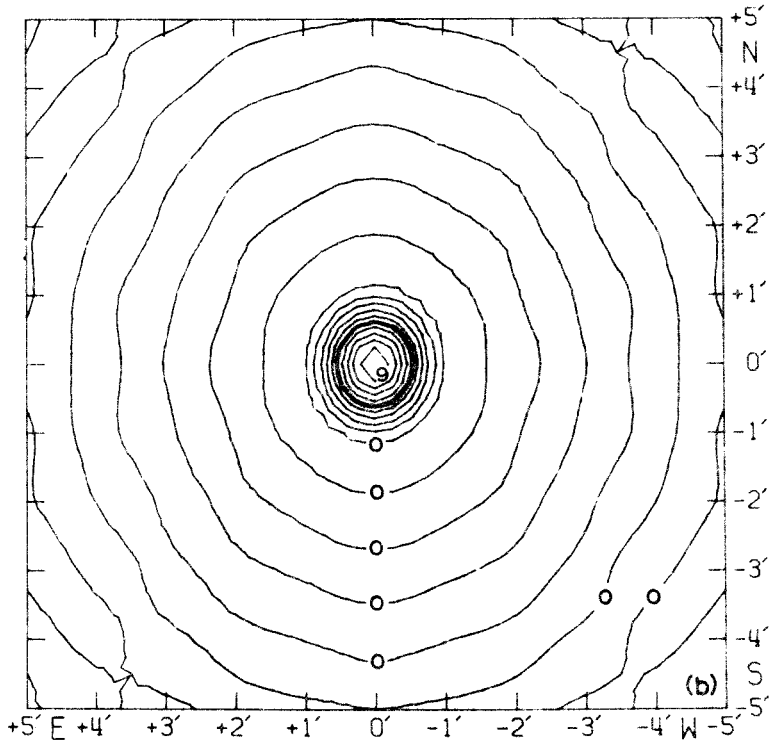
+5′ N +4′ +3′ +2′ +1′ 0′ -1′ -2′ -3′ -4′ S -5′
+5′ E +4′ +3′ +2′ +1′ 0′ -1′ -2′ -3′ -4′ W -5′
(b)

Figure 4

Response of the synthesized array at 2880 MHz to a point source at the declination of 3C10.

(a) 20' by 20' area; contour interval of 1; peak value of 10.

(b) 10' by 10' area; Half Power Beam Width contour darkened; contour interval of 1; peak value of 10.

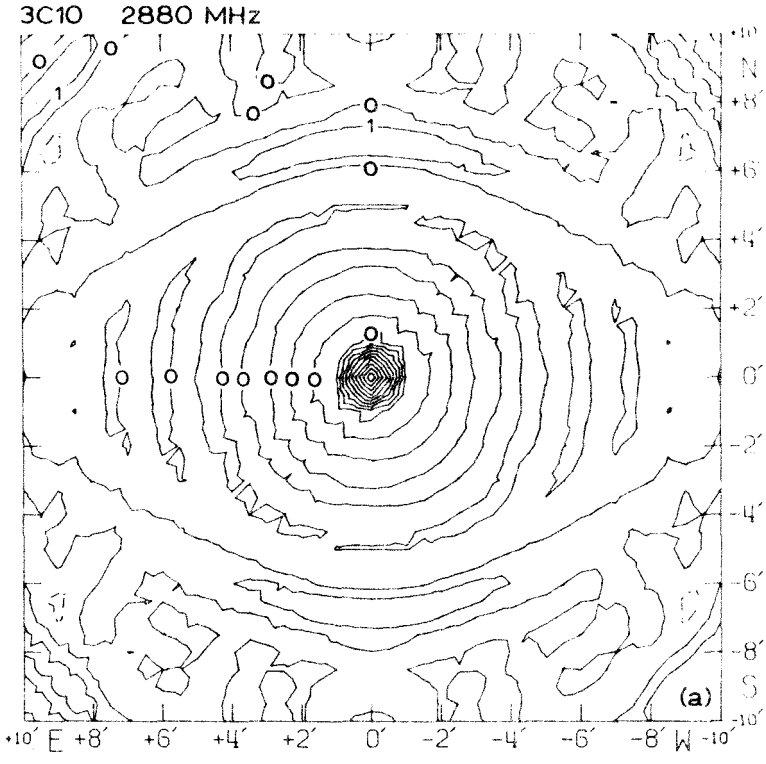
3C10 2880 MHz
+10′ E +8′ +6′ +4′ +2′ 0′ -2′ -4′ -6′ -8′ W -10′
+10′ N +8′ +6′ +4′ +2′ 0′ -2′ -4′ -6′ -8′ S -10′
(a)

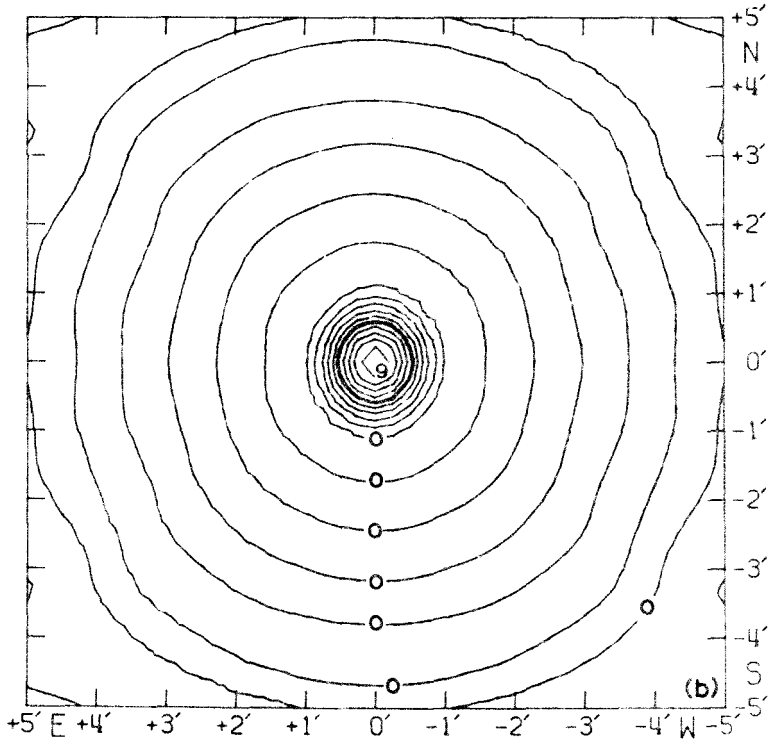
+5′ E +4′ +3′ +2′ +1′ 0′ -1′ -2′ -3′ -4′ W -5′
+5′ N +4′ +3′ +2′ +1′ 0′ -1′ -2′ -3′ -4′ S -5′
(b)

Figure 5

Response of the synthesized array at 1420 MHz to a point source at the declination of 3C58.

(a) 20' by 20' area; contour interval of 1; peak value of 10.

(b) 10' by 10' area; Half Power Beam Width contour darkened; contour interval of 1; peak value of 10.

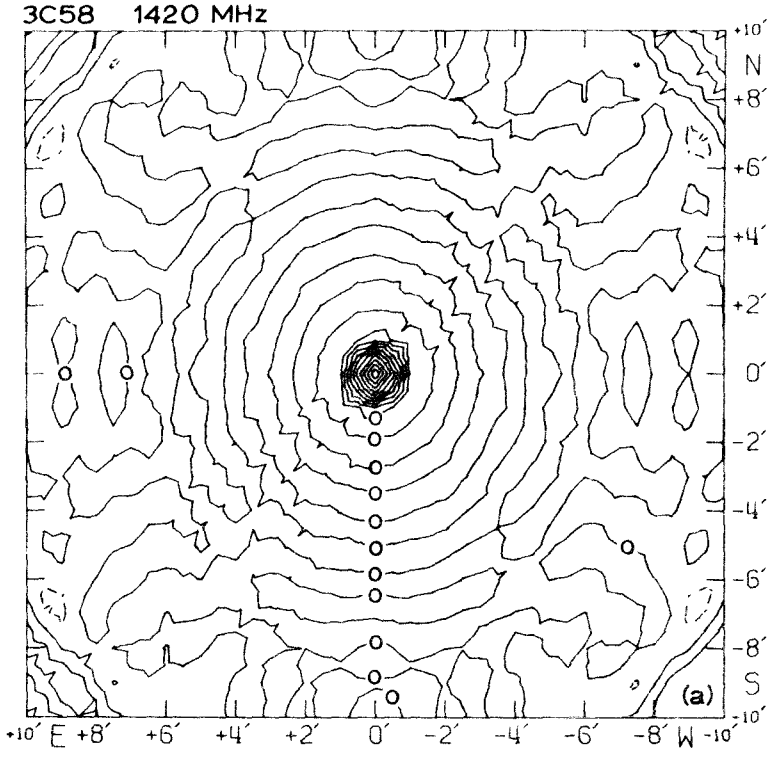
3C58 1420 MHz
+10′ N +8′ +6′ +4′ +2′ 0′ -2′ -4′ -6′ -8′ S -10′
+10′ E +8′ +6′ +4′ +2′ 0′ -2′ -4′ -6′ -8′ W -10′
(a)

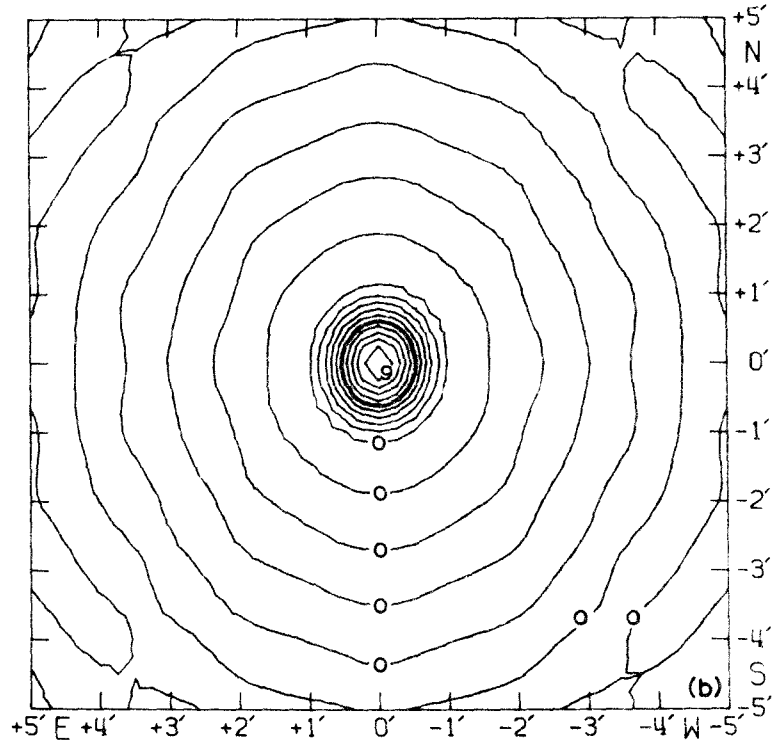
+5′ N +4′ +3′ +2′ +1′ 0′ -1′ -2′ -3′ -4′ S -5′
+5′ E +4′ +3′ +2′ +1′ 0′ -1′ -2′ -3′ -4′ W -5′
(b)

Figure 6

Response of the synthesized array at 2880 MHz to a point source at the declination of 3C58.

(a) 20' by 20' area; contour interval of 1; peak value of 10.

(b) 10' by 10' area; Half Power Beam Width contour darkened; contour interval of 1; peak value of 10.

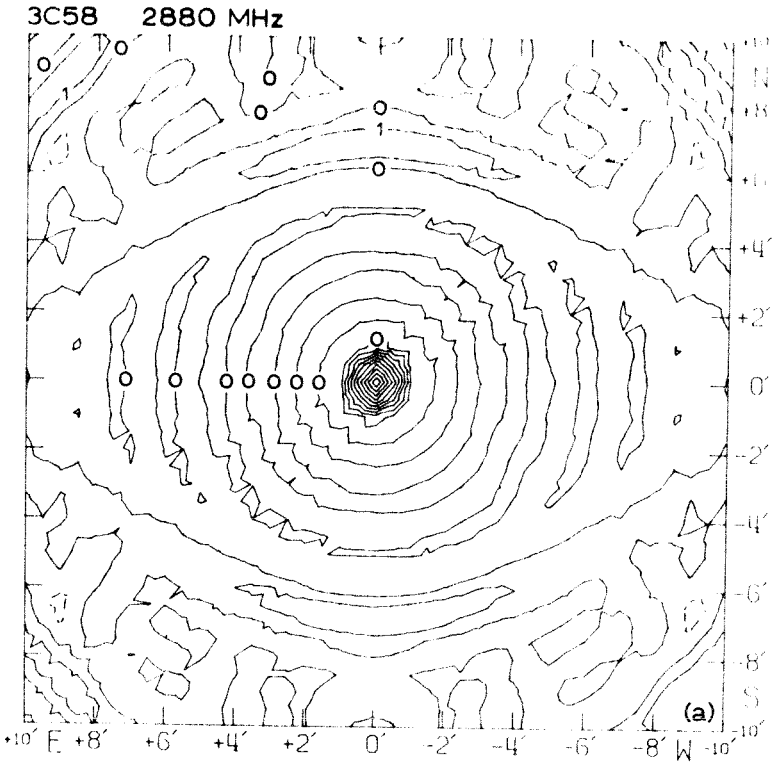
3C58 2880 MHz
(a)
+10′ E +8′ +6′ +4′ +2′ 0′ -2′ -4′ -6′ -8′ W -10′
+4′ +2′ 0′ -2′ -4′ -6′ -8′ S -10′

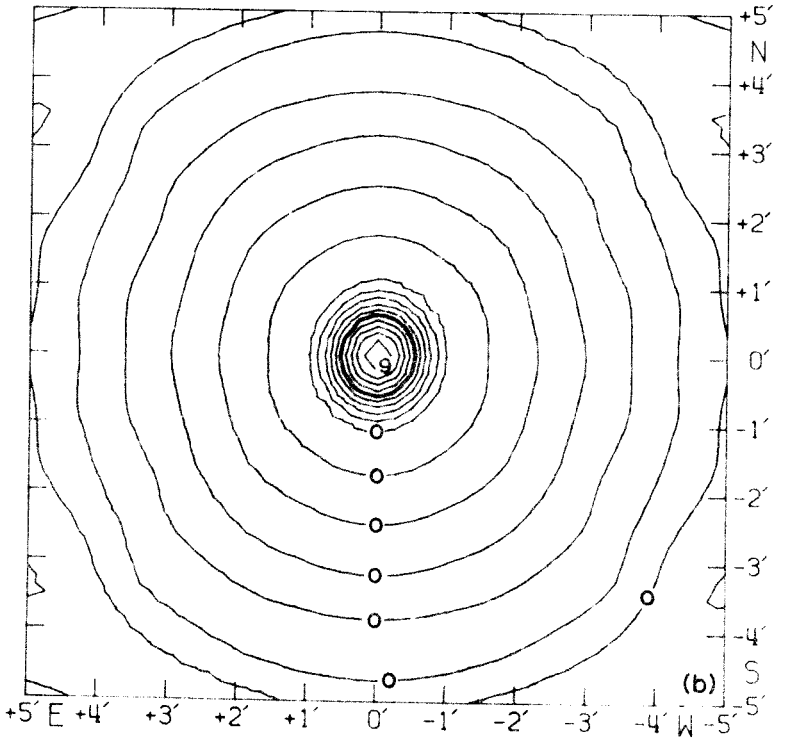
(b)
+5′ E +4′ +3′ +2′ +1′ 0′ -1′ -2′ -3′ -4′ W -5′
+5′ N +4′ +3′ +2′ +1′ 0′ -1′ -2′ -3′ -4′ S -5′

CHAPTER V

OBSERVATIONAL RESULTS

3C10

The resulting synthesized maps of 3C10 are displayed in squares 10' on a side. All details of position and scale are identical among the several diagrams with a center position in each case of $\alpha(1950.0) = 00^h22^m37^s.30$, $\delta(1950.0) = +63^\circ51'42''.0$.

Figure 7 shows the results at $\lambda = 21.1$ cm. The top diagram (a) displays the brightness distribution of the total radiation (I) normalized to the maximum value of 10 = 1.54 f.u. arcmin^{-2}.* Lines of Galactic longitude and latitude have been added to the plot for reference. Also, the Half Power Beam Width of slightly greater than one minute of arc is illustrated in the upper right hand corner. The middle diagram (b) displays the polarized flux density distribution ($\sqrt{U^2+ Q^2}$) normalized to a maximum value of 10 = 0.061 f.u. arcmin^{-2}. Due to the errors present in the data and the digital inversion method, only those areas having a polarized flux density greater than 20% of the maximum have been considered significant. This delimiting contour has been darkened. The bottom diagram (c) displays the observed position angle ($\frac{1}{2}\tan^{-1}(U/Q)$) distribution within the delimited area. The position angle is measured north through east and the percentage polarization is indicated by the line length. The length appropriate for 5% polarization is indicated in the lower left hand corner.

---

*1 f.u. arcmin^{-2} = 1.18 * 10^7 f.u. ster^{-1}

1 f.u. arcmin^{-2} = 190.79°K @ 1.42 GHz

1 f.u. arcmin^{-2} = 46.38°K @ 2.88 GHz

Figure 7

Distribution of the total intensity and polarization over 3C10 ($\alpha(1950.0) = 00^h22^m37^s.30$, $\delta(1950.0) = +63^\circ51'42''.0$) at 1420 MHz.

(a) Intensity of the total radiation; lines of Galactic longitude and latitude superposed; Half Power Beam Width shown in upper right hand corner; $10 = 1.54 * 10^{-26}$ W m^{-2} Hz^{-1} arcmin^{-2}.

(b) Intensity of the polarized radiation; 20% contour darkened; $10 = 0.061 * 10^{-26}$ W m^{-2} Hz^{-1} arcmin^{-2}.

(c) Position angle of the polarization; orientation of the line gives position of the electric vector; degree of linear polarization indicated by line length; line length appropriate for 5% polarization shown in lower left hand corner.

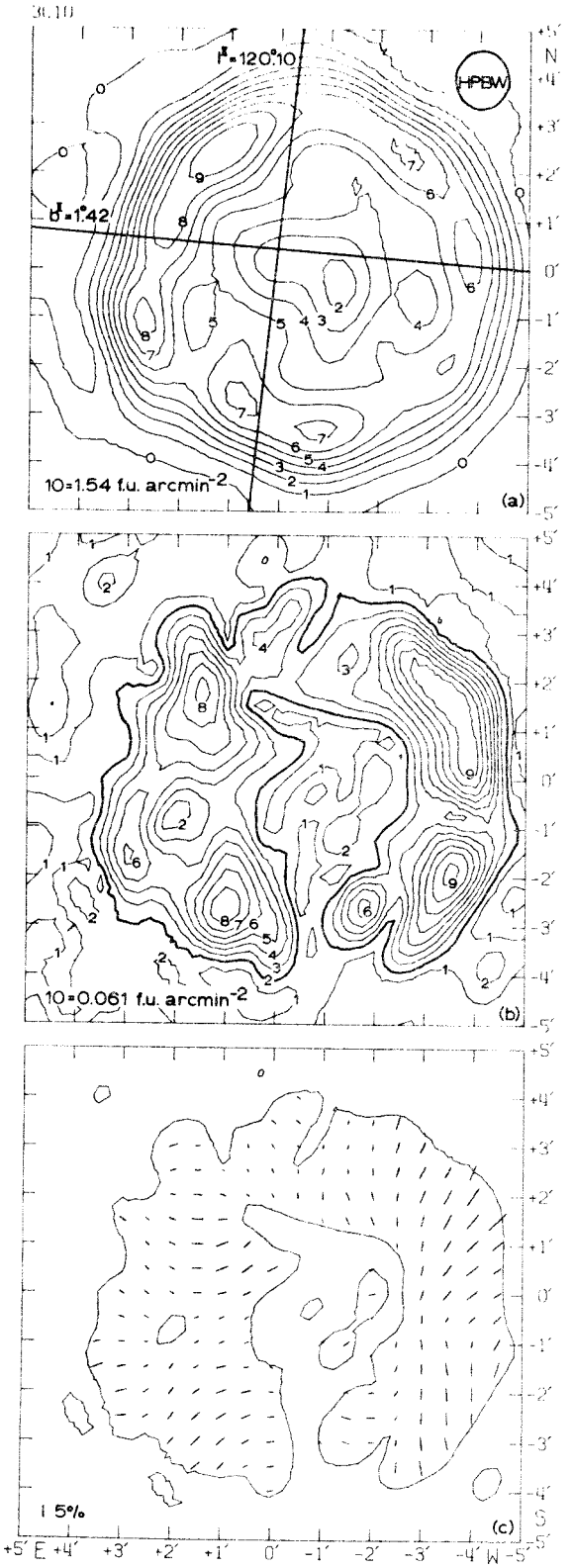
38.10
l = 120°10
b = 1°42
HPBW
10=1.54 f.u. arcmin^{-2}
(a)
10=0.061 f.u. arcmin^{-2}
(b)
1 5%
(c)
N
S
E
W
+5′ +4′ +3′ +2′ +1′ 0′ -1′ -2′ -3′ -4′ -5′

Figure 8 shows the results at λ = 10.4 cm in the same manner. The (a) map has a maximum value of I_0 = 0.91 f.u. arcmin^{-2}, while on the (b) map I_0 = 0.095 f.u. arcmin^{-2}. Only those areas with a polarized flux density greater than 30% of the maximum have been considered significant and this delimiting contour has been darkened. In the (c) map, the length appropriate for 10% polarization is illustrated in the lower left hand corner.

The brightness distribution of the total radiation for 3C10 is slowly varying with position, exhibiting no unresolved regions. It is seen to have a ring-like shape with a sharp outer edge. The brightest area lies in the north-east while the weaker sections of the ring are in the south-east and south-west. Near the center, the emission falls essentially to zero, a result which is incompatible with most uniformly emitting spherical shell models. These same features have been observed in more detail by Baldwin [44] at 1407 MHz with the Cambridge one-mile telescope.

On comparing the total intensity maps at the two observing frequencies, rather strong changes in detail are apparent. One must consider here the effect of the grating responses in the synthesized 10.4 cm beam shown in Figure 4. These result from the missing N/S antenna spacings. They unfortunately are approximately the same distance from the primary beam as the diameter of 3C10, resulting in a distortion. Although this nowhere exceeds 20%, it contributes to the apparent brightening and extension of the ring in the north-south direction. However, the distortion is not sufficient to explain all of the differences between the maps at the two frequencies, and it is

Figure 8

Distribution of the total intensity and polarization over 3C10 ($\alpha(1950.0) = 00^h22^m37^s.30$, $\delta(1950.0) = +63^\circ51'42''.0$) at 2880 MHz.

(a) Intensity of the total radiation; lines of Galactic longitude and latitude superposed; Half Power Beam Width shown in upper right hand corner; $10 = 0.91 * 10^{-26}$ W m^{-2} Hz^{-1} arcmin^{-2}.

(b) Intensity of the polarized radiation; 30% contour darkened; $10 = 0.095 * 10^{-26}$ W m^{-2} Hz^{-1} arcmin^{-2}.

(c) Position angle of the polarization; orientation of the line gives position of the electric vector; degree of linear polarization indicated by line length; line length appropriate for 10% polarization shown in lower left hand corner.

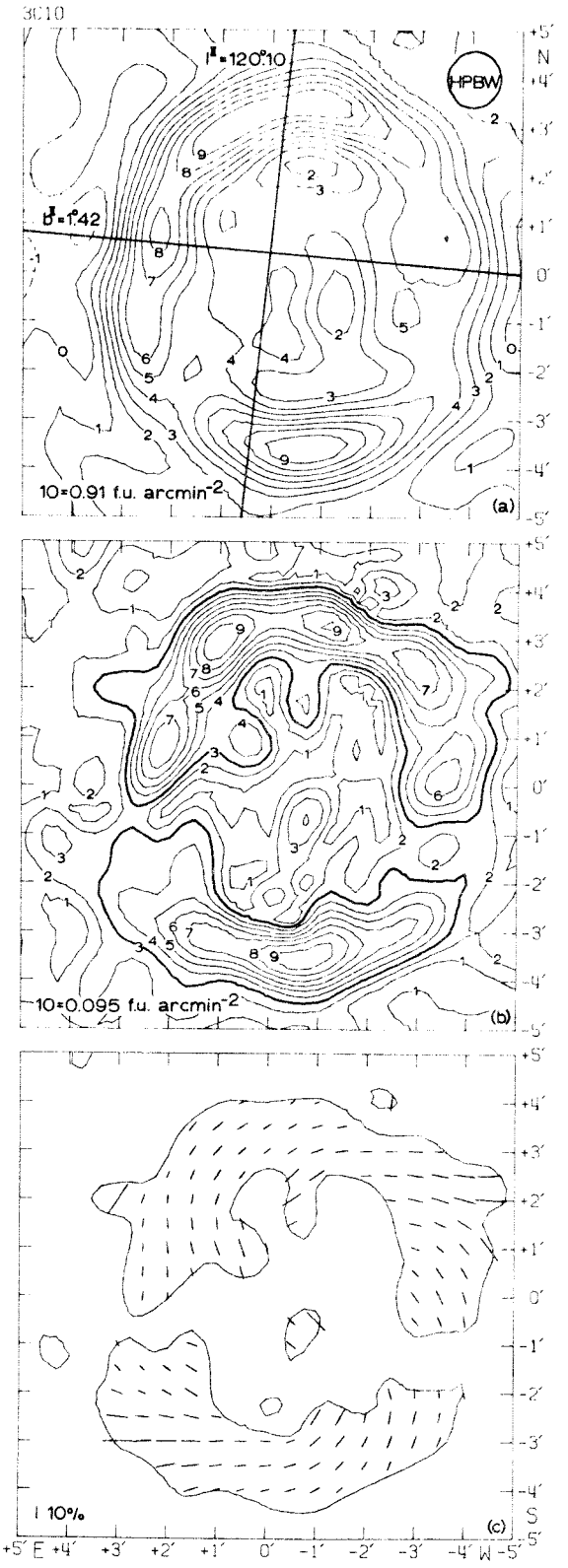
3C10
I = 120°10
b = 1°.42
HPBW
10=0.91 f.u. arcmin⁻²
(a)
10=0.095 f.u. arcmin⁻²
(b)
1 10%
(c)
N
S
E
W
+5′ +4′ +3′ +2′ +1′ 0′ -1′ -2′ -3′ -4′ -5′

believed that the spectral index varies across the source.

The polarized flux density distribution maps (b) exhibit a less pronounced ring-like structure. The shell is less complete and the correspondence of bright areas with those on the total intensity maps is weak. The agreement between the 21.1 cm and the 10.4 cm maps is rather poor due to distortion by the synthesized beam, changes in the spectral index, Faraday rotation, and depolarization. The small spots of polarized emission in the center of the ring are not considered significant and are believed to be the result of errors in the observational data.

The position angle and percentage polarization maps (c) display a smooth variation around the source. It is interesting to note that even though 3C10 exhibits an integrated polarization of only $0.7 \pm 0.4\%$ at 21.2 cm [36], when resolved the source contains areas exceeding 5% polarization at 21.1 cm and 10% polarization at 10.4 cm.

Although contour maps are qualitatively useful, they are tedious when quantitative data are desired. Therefore, parts of the contour map arrays have been included in tables along with the expected errors. Each table displays a value every half minute of arc on the 10' by 10' square. Since much of the area contains mostly noise, the data are shown only for a bounded region considered relevant.

Table VIII contains the 3C10 total intensity distribution in f.u. arcmin^{-2} at 21.1 cm for all values greater than the 10% contour. Each point has an error of approximately 0.06 f.u. arcmin^{-2}. In Table IX is found the 21.1 cm percentage polarization with errors for an area bounded by the 20% contour of the polarized flux density map. Table X

TABLE VIII. 3C10 TOTAL INTENSITY DISTRIBUTION IN F.U. ARCMIN^{-2} AT 1420 MHZ ($I_{21.1}$)

δ	+5.0 E	+4.5	+4.0	+3.5	+3.0	+2.5	+2.0	+1.5	+1.0	+0.5	0.0	-0.5	-1.0	-1.5	-2.0	-2.5	-3.0	-3.5	-4.0	-4.5	-5.0 W
+5.0 N																					
+4.5											0.21 ± 0.06	0.26 ± 0.06	0.20 ± 0.06								
+4.0									0.27 ± 0.06	0.47 ± 0.06	0.60 ± 0.06	0.65 ± 0.06	0.61 ± 0.06	0.44 ± 0.06	0.18 ± 0.06						
+3.5							0.16 ± 0.06	0.41 ± 0.06	0.78 ± 0.06	1.03 ± 0.06	1.06 ± 0.06	1.02 ± 0.06	1.02 ± 0.06	0.93 ± 0.06	0.65 ± 0.06	0.31 ± 0.06					
+3.0						0.25 ± 0.06	0.58 ± 0.06	1.01 ± 0.06	1.35 ± 0.06	1.39 ± 0.06	1.18 ± 0.06	1.00 ± 0.06	0.99 ± 0.06	1.06 ± 0.06	1.04 ± 0.06	0.84 ± 0.06	0.53 ± 0.06	0.24 ± 0.06			
+2.5						0.52 ± 0.06	1.07 ± 0.06	1.46 ± 0.06	1.54 ± 0.06	1.32 ± 0.06	0.97 ± 0.06	0.76 ± 0.06	0.71 ± 0.06	0.81 ± 0.06	1.02 ± 0.06	1.12 ± 0.06	0.95 ± 0.06	0.58 ± 0.06	0.20 ± 0.06		
+2.0					0.19 ± 0.06	0.81 ± 0.06	1.32 ± 0.06	1.44 ± 0.06	1.31 ± 0.06	1.07 ± 0.06	0.83 ± 0.06	0.71 ± 0.06	0.65 ± 0.06	0.62 ± 0.06	0.79 ± 0.06	1.02 ± 0.06	1.05 ± 0.06	0.83 ± 0.06	0.42 ± 0.06		
+1.5					0.42 ± 0.06	1.09 ± 0.06	1.34 ± 0.06	1.13 ± 0.06	0.95 ± 0.06	0.86 ± 0.06	0.78 ± 0.06	0.76 ± 0.06	0.71 ± 0.06	0.62 ± 0.06	0.64 ± 0.06	0.77 ± 0.06	0.89 ± 0.06	0.92 ± 0.06	0.65 ± 0.06	0.18 ± 0.06	
+1.0					0.64 ± 0.06	1.26 ± 0.06	1.28 ± 0.06	0.90 ± 0.06	0.71 ± 0.06	0.66 ± 0.06	0.61 ± 0.06	0.60 ± 0.06	0.60 ± 0.06	0.59 ± 0.06	0.62 ± 0.06	0.65 ± 0.06	0.74 ± 0.06	0.93 ± 0.06	0.84 ± 0.06	0.35 ± 0.06	
+0.5		0.17 ± 0.06	0.75 ± 0.06	1.24 ± 0.06	1.17 ± 0.06	0.84 ± 0.06	0.63 ± 0.06	0.49 ± 0.06	0.40 ± 0.06	0.40 ± 0.06	0.39 ± 0.06	0.45 ± 0.06	0.61 ± 0.06	0.65 ± 0.06	0.69 ± 0.06	0.93 ± 0.06	0.99 ± 0.06	0.48 ± 0.06			
0.0		0.33 ± 0.06	0.88 ± 0.06	1.13 ± 0.06	0.98 ± 0.06	0.81 ± 0.06	0.68 ± 0.06	0.47 ± 0.06	0.38 ± 0.06	0.38 ± 0.06	0.28 ± 0.06	0.33 ± 0.06	0.58 ± 0.06	0.64 ± 0.06	0.64 ± 0.06	0.88 ± 0.06	0.95 ± 0.06	0.92 ± 0.06			
-0.5		0.50 ± 0.06	1.09 ± 0.06	1.14 ± 0.06	0.82 ± 0.06	0.75 ± 0.06	0.77 ± 0.06	0.63 ± 0.06	0.56 ± 0.06	0.49 ± 0.06	0.28 ± 0.06	0.31 ± 0.06	0.58 ± 0.06	0.59 ± 0.06	0.56 ± 0.06	0.80 ± 0.06	0.88 ± 0.06	0.48 ± 0.06			
-1.0		0.50 ± 0.06	1.20 ± 0.06	1.23 ± 0.06	0.80 ± 0.06	0.71 ± 0.06	0.85 ± 0.06	0.81 ± 0.06	0.75 ± 0.06	0.61 ± 0.06	0.38 ± 0.06	0.44 ± 0.06	0.68 ± 0.06	0.63 ± 0.06	0.59 ± 0.06	0.80 ± 0.06	0.80 ± 0.06	0.38 ± 0.06			
-1.5		0.30 ± 0.06	1.03 ± 0.06	1.20 ± 0.06	0.84 ± 0.06	0.75 ± 0.06	0.91 ± 0.06	0.90 ± 0.06	0.80 ± 0.06	0.68 ± 0.06	0.53 ± 0.06	0.61 ± 0.06	0.77 ± 0.06	0.74 ± 0.06	0.76 ± 0.06	0.89 ± 0.06	0.73 ± 0.06	0.29 ± 0.06			
-2.0			0.86 ± 0.06	1.12 ± 0.06	0.86 ± 0.06	0.80 ± 0.06	0.95 ± 0.06	0.91 ± 0.06	0.79 ± 0.06	0.68 ± 0.06	0.59 ± 0.06	0.66 ± 0.06	0.78 ± 0.06	0.77 ± 0.06	0.84 ± 0.06	0.93 ± 0.06	0.88 ± 0.06	0.23 ± 0.06			
-2.5			0.41 ± 0.06	0.70 ± 0.06	0.73 ± 0.06	0.99 ± 0.06	1.11 ± 0.06	1.04 ± 0.06	0.85 ± 0.06	0.78 ± 0.06	0.78 ± 0.06	0.79 ± 0.06	0.79 ± 0.06	0.81 ± 0.06	0.86 ± 0.06	0.75 ± 0.06	0.41 ± 0.06				
-3.0			0.21 ± 0.06	0.38 ± 0.06	0.47 ± 0.06	0.71 ± 0.06	1.02 ± 0.06	1.09 ± 0.06	1.03 ± 0.06	1.03 ± 0.06	1.04 ± 0.06	0.97 ± 0.06	0.85 ± 0.06	0.76 ± 0.06	0.65 ± 0.06	0.44 ± 0.06	0.17 ± 0.06				
-3.5					0.19 ± 0.06	0.36 ± 0.06	0.62 ± 0.06	0.82 ± 0.06	0.96 ± 0.06	1.07 ± 0.06	1.07 ± 0.06	0.92 ± 0.06	0.71 ± 0.06	0.53 ± 0.06	0.36 ± 0.06	0.16 ± 0.06					
-4.0							0.18 ± 0.06	0.34 ± 0.06	0.54 ± 0.06	0.69 ± 0.06	0.68 ± 0.06	0.52 ± 0.06	0.33 ± 0.06	0.20 ± 0.06							
-4.5									0.16 ± 0.06	0.23 ± 0.06	0.22 ± 0.06	0.15 ± 0.06									
-5.0 S																					

TABLE IX. 3C10 POLARIZATION DISTRIBUTION IN PERCENT AT 1420 MHZ ($P_{21.1}$)

δ	+5.0 E	+4.5	+4.0	+3.5	+3.0	+2.5	+2.0	+1.5	+1.0	+0.5	0.0	-0.5	-1.0	-1.5	-2.0	-2.5	-3.0	-3.5	-4.0	-4.5	-5.0 W
+5.0 N																					
+4.5																					
+4.0												2.5 ± 1.1									
+3.5											2.1 ± 0.7	2.4 ± 0.7		1.7 ± 0.8	2.4 ± 1.2	5.7 ± 2.6					
+3.0							4.1 ± 1.3	2.6 ± 0.7		1.8 ± 0.5	2.1 ± 0.6	1.3 ± 0.7	1.6 ± 0.7	1.9 ± 0.7	2.7 ± 0.7	4.7 ± 0.9	4.7 ± 1.5				
+2.5							2.6 ± 0.7	2.7 ± 0.5	1.1 ± 0.5	1.7 ± 0.6	2.2 ± 0.8	1.8 ± 1.0	3.0 ± 1.1	2.0 ± 0.9	2.8 ± 0.7	4.6 ± 0.7	5.4 ± 0.8	5.0 ± 1.4	6.6 ± 4.1		
+2.0							2.3 ± 0.6	3.5 ± 0.5	2.6 ± 0.6	1.6 ± 0.7	2.1 ± 0.9	2.7 ± 1.1	3.4 ± 1.2	3.8 ± 1.2	3.7 ± 1.0	4.3 ± 0.8	5.7 ± 0.8	6.7 ± 1.0	8.5 ± 2.1		
+1.5				3.5 ± 1.8	2.3 ± 0.7	2.9 ± 0.6	4.4 ± 0.7	3.6 ± 0.8				1.6 ± 1.0	2.2 ± 1.0	3.2 ± 1.2	3.6 ± 1.2	4.0 ± 1.0	5.4 ± 0.9	6.7 ± 0.9	7.8 ± 1.3	9.9 ± 5.2	
+1.0					2.3 ± 0.6	3.0 ± 0.6	4.7 ± 0.9	5.4 ± 1.1	3.9 ± 1.2							2.7 ± 1.2	4.7 ± 1.1	5.7 ± 0.9	6.5 ± 1.0	5.4 ± 2.3	
+0.5					2.3 ± 0.6	2.8 ± 0.6	4.3 ± 0.9	5.4 ± 1.3	5.3 ± 1.6	4.6 ± 2.0					2.1 ± 1.2		4.2 ± 1.1	5.4 ± 0.9	6.1 ± 0.9	4.0 ± 1.6	
0.0				2.4 ± 0.8	2.6 ± 0.7	2.5 ± 0.8	3.3 ± 0.9	3.6 ± 1.1	3.6 ± 1.6						3.1 ± 1.3		4.3 ± 1.2	5.0 ± 0.9	5.6 ± 0.8	3.9 ± 1.5	
-0.5				2.8 ± 0.7	2.5 ± 0.7		2.2 ± 1.0	2.6 ± 1.0	2.3 ± 1.2								3.7 ± 1.4	2.6 ± 0.9	3.9 ± 0.9	4.2 ± 1.6	
-1.0		3.3 ± 1.5	2.8 ± 0.6	1.7 ± 0.6		2.4 ± 1.0	2.9 ± 0.9	2.0 ± 0.9					3.3 ± 2.0	3.4 ± 1.7		2.8 ± 1.2	4.2 ± 1.3	3.4 ± 0.9	7.8 ± 0.9	5.3 ± 2.0	
-1.5		6.1 ± 2.7	3.7 ± 0.7	2.3 ± 0.6	2.8 ± 0.9	2.9 ± 1.0	4.0 ± 0.8	2.9 ± 0.8	1.6 ± 0.9							3.3 ± 1.0	4.3 ± 1.0	5.6 ± 0.9	5.5 ± 1.1	6.6 ± 2.6	
-2.0			4.7 ± 1.1	2.9 ± 0.8	3.3 ± 0.9	3.5 ± 0.9	4.5 ± 0.8	3.9 ± 0.8	2.3 ± 1.0					1.9 ± 1.1	2.4 ± 1.0	3.0 ± 0.9	4.7 ± 0.9	6.3 ± 0.9	6.2 ± 1.3		
-2.5			4.6 ± 1.9	2.6 ± 1.1	3.8 ± 1.0	4.6 ± 0.9	4.8 ± 0.7	4.1 ± 0.7	3.1 ± 0.9					3.9 ± 1.0	4.5 ± 1.0	2.0 ± 0.9	5.0 ± 0.9	5.9 ± 1.1	4.4 ± 1.9		
-3.0					3.6 ± 1.6	5.2 ± 1.1	4.8 ± 0.8	3.4 ± 0.7	3.2 ± 0.7			1.3 ± 0.7	2.9 ± 0.8	2.7 ± 0.9	2.6 ± 1.0	6.0 ± 1.2	5.4 ± 1.8				
-3.5						4.6 ± 2.2	3.9 ± 1.2	2.4 ± 0.9	2.9 ± 0.8						4.6 ± 1.5	6.5 ± 2.3					
-4.0									2.9 ± 1.4												
-4.5																					
-5.0 S																					

TABLE X. 3C10 POSITION ANGLE DISTRIBUTION IN DEGREES AT 1420 MHZ ($PA_{21.1}$)

	+5.0 E	+4.5	+4.0	+3.5	+3.0	+2.5	+2.0	+1.5	+1.0	+0.5	0.0	-0.5	-1.0	-1.5	-2.0	-2.5	-3.0	-3.5	-4.0	-4.5	-5.0 W
+5.0 N																					
+4.5																					
+4.0												52. ± 10.									
+3.5											48. ± 7.	49. ± 6.		166. ± 9.	167. ± 9.	161. ± 8.					
+3.0							111. ± 6.	97. ± 9.		12. ± 6.	34. ± 6.	37. ± 12.	158. ± 9.	162. ± 7.	168. ± 5.	160. ± 4.	155. ± 6.				
+2.5							105. ± 5.	91. ± 4.	68. ± 8.	27. ± 7.	28. ± 7.	2. ± 10.	163. ± 7.	179. ± 9.	179. ± 9.	162. ± 3.	153. ± 3.	153. ± 5.	157. ± 11.		
+2.0							85. ± 5.	84. ± 3.	77. ± 4.	51. ± 9.	32. ± 9.	7. ± 7.	2. ± 6.	24. ± 6.	16. ± 5.	169. ± 3.	158. ± 2.	152. ± 3.	144. ± 4.		
+1.5				56. ± 10.	55. ± 6.	70. ± 4.	85. ± 3.	95. ± 4.				19. ± 12.	16. ± 9.	26. ± 8.	22. ± 6.	3. ± 5.	167. ± 3.	153. ± 2.	141. ± 3.	134. ± 9.	
+1.0					48. ± 5.	63. ± 4.	90. ± 3.	113. ± 4.	132. ± 6.							11. ± 8.	173. ± 4.	150. ± 3.	135. ± 3.	130. ± 6.	
+0.5					45. ± 5.	61. ± 5.	91. ± 4.	113. ± 4.	127. ± 6.	117. ± 6.					114. ± 12.		167. ± 5.	144. ± 3.	129. ± 3.	123. ± 8.	
0.0				60. ± 7.	53. ± 5.	65. ± 6.	92. ± 5.	106. ± 6.	116. ± 9.						103. ± 8.		163. ± 5.	142. ± 4.	127. ± 3.	123. ± 7.	
-0.5				71. ± 5.	66. ± 5.		107. ± 9.	111. ± 7.	119. ± 12.								177. ± 7.	152. ± 7.	133. ± 5.	131. ± 8.	
-1.0		102. ± 9.	89. ± 4.	90. ± 7.			120. ± 9.	109. ± 6.	112. ± 9.				128. ± 12.	123. ± 10.		170. ± 8.	10. ± 6.	13. ± 5.	166. ± 6.	150. ± 7.	
-1.5		111. ± 8.	103. ± 4.	115. ± 5.	140. ± 7.	118. ± 7.	103. ± 4.	98. ± 6.	65. ± 12.							157. ± 8.	1. ± 4.	11. ± 3.	1. ± 4.	162. ± 8.	
-2.0			105. ± 4.	122. ± 5.	143. ± 5.	125. ± 5.	110. ± 3.	102. ± 4.	82. ± 8.					77. ± 11.	98. ± 8.	142. ± 7.	174. ± 3.	5. ± 2.	1. ± 4.		
-2.5			96. ± 7.	121. ± 8.	144. ± 6.	134. ± 4.	124. ± 3.	113. ± 3.	96. ± 5.					79. ± 5.	90. ± 4.	142. ± 10.	178. ± 3.	4. ± 3.	178. ± 8.		
-3.0					138. ± 9.	136. ± 4.	132. ± 3.	118. ± 4.	98. ± 4.				40. ± 11.	71. ± 5.	92. ± 6.	170. ± 7.	6. ± 4.	12. ± 6.			
-3.5						130. ± 9.	138. ± 6.	115. ± 8.	97. ± 5.							174. ± 6.	10. ± 6.				
-4.0										97. ± 9.											
-4.5																					
-5.0 S																					

contains the 21.1 cm position angle and error in degrees.

Shown in Table XI are the values for the total intensity distribution in f.u. arcmin^{-2} of 3C10 at 10.4 cm wavelength. With an individual point error of approximately 0.11 f.u. arcmin^{-2}, the delimiting contour has been chosen at 20%. Table XII presents the 10.4 cm percentage polarization and errors for a region bounded by the polarized flux density 30% contour, and Table XIII displays the 10.4 cm position angle and error in degrees.

3C58

The contour maps for 3C58 are presented in the same manner as those for 3C10. The central position in each case is $\alpha(1950.0) = 02^h01^m52^s.80$, $\delta(1950.0) = +64^\circ35'14''.0$.

Figure 9 displays the results at $\lambda = 21.1$ cm. The total intensity map (a) has been normalized to a maximum value of $10 = 2.47$ f.u. arcmin^{-2}. Lines of Galactic longitude and latitude have been added along with a Half Power Beam Width contour. The polarized flux density distribution (b) has been normalized to a maximum value of $10 = 0.155$ f.u. arcmin^{-2}. Only those values exceeding 20% of the maximum are considered significant and that contour has been darkened. The bottom diagram (c) displays the observed position angle and percentage polarization distribution within the darkened contour. The length appropriate for 10% polarization is indicated in the lower left hand corner.

The results for $\lambda = 10.4$ cm are displayed similarly in Figure 10. The (a) map has a maximum value of $10 = 2.26$ f.u. arcmin^{-2}, while the (b) map is normalized to $10 = 0.24$ f.u. arcmin^{-2}. Again the 20%

TABLE XI. 3C10 TOTAL INTENSITY DISTRIBUTION IN F.U. ARCMIN^{-2} AT 2080 MHZ ($I_{10.4}$)

	+5.0 E	+4.5	+4.0	+3.5	+3.0	+2.5	+2.0	+1.5	+1.0	+0.5	0.0	-0.5	-1.0	-1.5	-2.0	-2.5	-3.0	-3.5	-4.0	-4.5	M -5.0
+5.0							0.21 ± 0.11	0.26 ± 0.11	0.31 ± 0.11	0.33 ± 0.11	0.34 ± 0.11	0.34 ± 0.11	0.31 ± 0.11	0.26 ± 0.11	0.26 ± 0.11	0.27 ± 0.11	0.26 ± 0.11	0.20 ± 0.11			
N																					
+4.5								0.21 ± 0.11	0.26 ± 0.11	0.30 ± 0.11	0.39 ± 0.11	0.41 ± 0.11	0.41 ± 0.11	0.34 ± 0.11	0.26 ± 0.11	0.26 ± 0.11	0.26 ± 0.11	0.20 ± 0.11			
+4.0								0.20 ± 0.11	0.32 ± 0.11	0.46 ± 0.11	0.57 ± 0.11	0.66 ± 0.11	0.68 ± 0.11	0.57 ± 0.11	0.37 ± 0.11	0.29 ± 0.11	0.22 ± 0.11	0.18 ± 0.11			
+3.5							0.20 ± 0.11	0.41 ± 0.11	0.64 ± 0.11	0.81 ± 0.11	0.87 ± 0.11	0.88 ± 0.11	0.90 ± 0.11	0.84 ± 0.11	0.63 ± 0.11	0.41 ± 0.11	0.29 ± 0.11	0.20 ± 0.11			
+3.0						0.18 ± 0.11	0.46 ± 0.11	0.74 ± 0.11	0.89 ± 0.11	0.88 ± 0.11	0.74 ± 0.11	0.63 ± 0.11	0.65 ± 0.11	0.71 ± 0.11	0.70 ± 0.11	0.60 ± 0.11	0.47 ± 0.11	0.31 ± 0.11	0.20 ± 0.11	0.19 ± 0.11	
+2.5						0.32 ± 0.11	0.66 ± 0.11	0.84 ± 0.11	0.78 ± 0.11	0.57 ± 0.11	0.34 ± 0.11	0.21 ± 0.11	0.22 ± 0.11	0.34 ± 0.11	0.49 ± 0.11	0.59 ± 0.11	0.56 ± 0.11	0.39 ± 0.11	0.22 ± 0.11	0.19 ± 0.11	0.19 ± 0.11
+2.0						0.49 ± 0.11	0.70 ± 0.11	0.67 ± 0.11	0.49 ± 0.11	0.32 ± 0.11	0.22 ± 0.11	0.19 ± 0.11	0.18 ± 0.11	0.21 ± 0.11	0.33 ± 0.11	0.47 ± 0.11	0.52 ± 0.11	0.42 ± 0.11	0.24 ± 0.11		
+1.5					0.19 ± 0.11	0.59 ± 0.11	0.69 ± 0.11	0.47 ± 0.11	0.30 ± 0.11	0.29 ± 0.11	0.33 ± 0.11	0.35 ± 0.11	0.33 ± 0.11	0.30 ± 0.11	0.35 ± 0.11	0.43 ± 0.11	0.48 ± 0.11	0.46 ± 0.11	0.30 ± 0.11		
+1.0					0.26 ± 0.11	0.70 ± 0.11	0.71 ± 0.11	0.41 ± 0.11	0.26 ± 0.11	0.30 ± 0.11	0.33 ± 0.11	0.33 ± 0.11	0.30 ± 0.11	0.32 ± 0.11	0.40 ± 0.11	0.46 ± 0.11	0.50 ± 0.11	0.53 ± 0.11	0.40 ± 0.11		
+0.5					0.32 ± 0.11	0.71 ± 0.11	0.70 ± 0.11	0.44 ± 0.11	0.30 ± 0.11	0.30 ± 0.11	0.32 ± 0.11	0.29 ± 0.11	0.22 ± 0.11	0.25 ± 0.11	0.38 ± 0.11	0.47 ± 0.11	0.50 ± 0.11	0.54 ± 0.11	0.45 ± 0.11	0.19 ± 0.11	
0.0					0.42 ± 0.11	0.65 ± 0.11	0.60 ± 0.11	0.44 ± 0.11	0.33 ± 0.11	0.31 ± 0.11	0.37 ± 0.11	0.35 ± 0.11	0.21 ± 0.11	0.19 ± 0.11	0.35 ± 0.11	0.49 ± 0.11	0.46 ± 0.11	0.48 ± 0.11	0.42 ± 0.11	0.20 ± 0.11	
-0.5					0.50 ± 0.11	0.62 ± 0.11	0.49 ± 0.11	0.39 ± 0.11	0.33 ± 0.11	0.30 ± 0.11	0.37 ± 0.11	0.34 ± 0.11			0.33 ± 0.11	0.46 ± 0.11	0.45 ± 0.11	0.43 ± 0.11	0.35 ± 0.11		
-1.0					0.51 ± 0.11	0.63 ± 0.11	0.45 ± 0.11	0.37 ± 0.11	0.36 ± 0.11	0.33 ± 0.11	0.38 ± 0.11	0.34 ± 0.11			0.35 ± 0.11	0.46 ± 0.11	0.45 ± 0.11	0.41 ± 0.11	0.28 ± 0.11		
-1.5					0.43 ± 0.11	0.60 ± 0.11	0.44 ± 0.11	0.37 ± 0.11	0.38 ± 0.11	0.36 ± 0.11	0.39 ± 0.11	0.40 ± 0.11	0.27 ± 0.11	0.22 ± 0.11	0.32 ± 0.11	0.39 ± 0.11	0.41 ± 0.11	0.40 ± 0.11	0.25 ± 0.11		
-2.0					0.32 ± 0.11	0.51 ± 0.11	0.41 ± 0.11	0.36 ± 0.11	0.37 ± 0.11	0.30 ± 0.11	0.27 ± 0.11	0.29 ± 0.11	0.25 ± 0.11	0.20 ± 0.11	0.23 ± 0.11	0.30 ± 0.11	0.39 ± 0.11	0.41 ± 0.11	0.28 ± 0.11		
-2.5					0.22 ± 0.11	0.38 ± 0.11	0.37 ± 0.11	0.40 ± 0.11	0.45 ± 0.11	0.35 ± 0.11	0.23 ± 0.11	0.22 ± 0.11	0.25 ± 0.11	0.27 ± 0.11	0.32 ± 0.11	0.38 ± 0.11	0.45 ± 0.11	0.43 ± 0.11	0.30 ± 0.11		
-3.0						0.25 ± 0.11	0.33 ± 0.11	0.47 ± 0.11	0.61 ± 0.11	0.61 ± 0.11	0.54 ± 0.11	0.54 ± 0.11	0.58 ± 0.11	0.61 ± 0.11	0.60 ± 0.11	0.56 ± 0.11	0.48 ± 0.11	0.35 ± 0.11	0.21 ± 0.11		
-3.5							0.24 ± 0.11	0.39 ± 0.11	0.58 ± 0.11	0.74 ± 0.11	0.84 ± 0.11	0.90 ± 0.11	0.90 ± 0.11	0.82 ± 0.11	0.69 ± 0.11	0.53 ± 0.11	0.35 ± 0.11	0.18 ± 0.11			
-4.0			0.22 ± 0.11	0.19 ± 0.11			0.18 ± 0.11	0.25 ± 0.11	0.37 ± 0.11	0.53 ± 0.11	0.69 ± 0.11	0.76 ± 0.11	0.72 ± 0.11	0.60 ± 0.11	0.46 ± 0.11	0.32 ± 0.11	0.19 ± 0.11				
-4.5			0.22 ± 0.11	0.26 ± 0.11	0.24 ± 0.11	0.23 ± 0.11	0.24 ± 0.11	0.26 ± 0.11	0.32 ± 0.11	0.38 ± 0.11	0.39 ± 0.11	0.35 ± 0.11	0.30 ± 0.11	0.25 ± 0.11	0.20 ± 0.11					0.20 ± 0.11	0.18 ± 0.11
S -5.0				0.22 ± 0.11	0.24 ± 0.11	0.26 ± 0.11	0.26 ± 0.11	0.25 ± 0.11	0.26 ± 0.11	0.27 ± 0.11	0.24 ± 0.11	0.22 ± 0.11	0.22 ± 0.11	0.21 ± 0.11	0.22 ± 0.11	0.22 ± 0.11	0.20 ± 0.11	0.19 ± 0.11	0.20 ± 0.11	0.18 ± 0.11	

TABLE XII. 3C10 POLARIZATION DISTRIBUTION IN PERCENT AT 2680 MHZ ($P_{10.4}$)

	+5.0 E	+4.5	+4.0	+3.5	+3.0	+2.5	+2.0	+1.5	+1.0	+0.5	0.0	-0.5	-1.0	-1.5	-2.0	-2.5	-3.0	-3.5	-4.0	-4.5 W	-5.0
+5.0 N																					
+4.5																					
+4.0										7. ± 4.		5. ± 3.	5. ± 3.			13. ± 9.					
+3.5								9. ± 5.	11. ± 3.	9. ± 2.	8. ± 2.	8. ± 2.	9. ± 2.	8. ± 2.							
+3.0								9. ± 3.	11. ± 2.	9. ± 2.	7. ± 2.	9. ± 3.	11. ± 3.	11. ± 3.	9. ± 3.	10. ± 3.	12. ± 4.	11. ± 6.			
+2.5							6. ± 3.	9. ± 2.	10. ± 3.	8. ± 3.		15. ± 11.	15. ± 10.	8. ± 6.	8. ± 4.	11. ± 3.	14. ± 4.	15. ± 6.	18. ± 11.	19. ± 14.	
+2.0			92. ± 311.	28. ± 28.	8. ± 4.	7. ± 3.	9. ± 3.	10. ± 4.				18. ± 13.	16. ± 13.			8. ± 4.	13. ± 4.	15. ± 5.	19. ± 11.	20. ± 24.	
+1.5					7. ± 3.	9. ± 3.	11. ± 4.	11. ± 7.	11. ± 7.			10. ± 6.	8. ± 6.				11. ± 4.	11. ± 4.	14. ± 7.		
+1.0					8. ± 3.	10. ± 3.	12. ± 5.	13. ± 8.	15. ± 8.	9. ± 6.							8. ± 4.	9. ± 4.	12. ± 5.	24. ± 22.	
+0.5					9. ± 3.	9. ± 3.	7. ± 4.		12. ± 7.								8. ± 4.	11. ± 4.	12. ± 5.		
0.0					8. ± 3.	8. ± 3.											11. ± 4.	13. ± 5.	11. ± 5.		
-0.5												9. ± 6.	21. ± 18.				9. ± 4.	10. ± 4.	10. ± 8.		
-1.0				6. ± 3.				9. ± 5.				10. ± 6.									
-1.5				8. ± 4.	6. ± 3.	8. ± 4.	11. ± 4.														
-2.0				11. ± 6.	7. ± 4.	9. ± 5.	12. ± 6.									11. ± 7.	8. ± 5.	7. ± 4.	10. ± 7.		
-2.5				18. ± 12.	11. ± 5.	12. ± 6.	13. ± 5.	6. ± 4.					16. ± 10.	15. ± 8.	10. ± 6.	11. ± 5.	12. ± 5.	9. ± 4.			
-3.0				24. ± 23.	16. ± 10.	17. ± 7.	15. ± 5.	12. ± 3.	9. ± 3.	9. ± 4.	8. ± 3.	12. ± 4.	12. ± 3.	10. ± 3.	11. ± 3.	12. ± 4.	10. ± 6.				
-3.5						14. ± 10.	15. ± 6.	11. ± 3.	10. ± 3.	10. ± 2.	10. ± 2.	10. ± 2.	9. ± 2.	8. ± 3.	8. ± 4.						
-4.0							12. ± 6.	8. ± 5.	7. ± 3.	6. ± 3.	9. ± 3.	9. ± 3.	7. ± 3.								
-4.5																					
-5.0 S																					

TABLE XIII. 3C10 POSITION ANGLE DISTRIBUTION IN DEGREES AT 2880 MHZ ($PA_{10.4}$)

	E +5'.0	+4'.5	+4'.0	+3'.5	+3'.0	+2'.5	+2'.0	+1'.5	+1'.0	+0'.5	0'.0	-0'.5	-1'.0	-1'.5	-2'.0	-2'.5	-3'.0	-3'.5	-4'.0	-4'.5	W -5'.0
+5'.0 N																					
+4'.5																					
+4'.0										116. ± 10.		123. ± 9.	107. ± 9.			172. ± 11.					
+3'.5								143. ± 8.	131. ± 4.	124. ± 4.	124. ± 5.	120. ± 4.	107. ± 4.	99. ± 5.							
+3'.0								147. ± 4.	139. ± 3.	132. ± 4.	129. ± 6.	125. ± 5.	110. ± 5.	98. ± 5.	93. ± 6.	91. ± 6.	88. ± 7.	90. ± 11.			
+2'.5							157. ± 8.	155. ± 4.	149. ± 4.	144. ± 7.		136. ± 9.	126. ± 9.	100. ± 13.	90. ± 9.	86. ± 6.	81. ± 5.	79. ± 6.	83. ± 9.	92. ± 10.	
+2'.0			151. ± 11.	147. ± 9.	160. ± 9.	174. ± 7.	169. ± 6.	162. ± 7.				124. ± 9.	132. ± 11.			83. ± 9.	77. ± 5.	72. ± 5.	74. ± 8.	86. ± 10.	
+1'.5					173. ± 9.	6. ± 6.	7. ± 7.	6. ± 11.	16. ± 11.			118. ± 9.	119. ± 12.				77. ± 7.	66. ± 6.	57. ± 8.		
+1'.0					180. ± 7.	8. ± 5.	15. ± 7.	20. ± 10.	18. ± 7.	12. ± 12.							69. ± 9.	51. ± 7.	40. ± 6.	37. ± 10.	
+0'.5					177. ± 6.	4. ± 5.	16. ± 11.		17. ± 10.								44. ± 7.	34. ± 5.	29. ± 6.		
0'.0					173. ± 7.	175. ± 11.											36. ± 6.	24. ± 5.	18. ± 7.		
-0'.5												45. ± 10.	44. ± 9.				39. ± 8.	25. ± 8.	9. ± 10.		
-1'.0				25. ± 11.				71. ± 10.				50. ± 9.									
-1'.5				44. ± 9.	49. ± 9.	55. ± 8.	58. ± 8.														
-2'.0				69. ± 9.	68. ± 10.	60. ± 8.	57. ± 7.									16. ± 11.	2. ± 11.	2. ± 12.	13. ± 12.		
-2'.5				83. ± 4.	85. ± 8.	79. ± 8.	76. ± 7.	80. ± 9.					149. ± 8.	151. ± 8.	168. ± 11.	170. ± 8.	166. ± 7.	167. ± 9.			
-3'.0				41. ± 12.	93. ± 9.	91. ± 7.	89. ± 5.	92. ± 5.	90. ± 6.	87. ± 8.	110. ± 9.	133. ± 4.	143. ± 4.	153. ± 5.	160. ± 6.	161. ± 6.	158. ± 10.				
-3'.5						101. ± 9.	96. ± 6.	97. ± 6.	96. ± 5.	96. ± 4.	106. ± 4.	122. ± 3.	136. ± 4.	149. ± 5.	159. ± 8.						
-4'.0							108. ± 11.	108. ± 12.	108. ± 10.	104. ± 6.	109. ± 5.	119. ± 5.	131. ± 7.								
-4'.5																					
S -5'.0																					

Figure 9

Distribution of the total intensity and polarization over 3C58 ($\alpha(1950.0) = 02^h01^m52^s.80$, $\delta(1950.0) = +64^o35'14''.0$) at 1420 MHz.

(a) Intensity of the total radiation; lines of Galactic longitude and latitude superposed; Half Power Beam Width shown in upper right hand corner; $10 = 2.47 * 10^{-26}$ W m^{-2} Hz^{-1} arcmin^{-2}.

(b) Intensity of the polarized radiation; 20% contour darkened; $10 = 0.155 * 10^{-26}$ W m^{-2} Hz^{-1} arcmin^{-2}.

(c) Position angle of the polarization; orientation of the line gives position of the electric vector; degree of linear polarization indicated by line length; line length appropriate for 10% polarization shown in lower left hand corner.

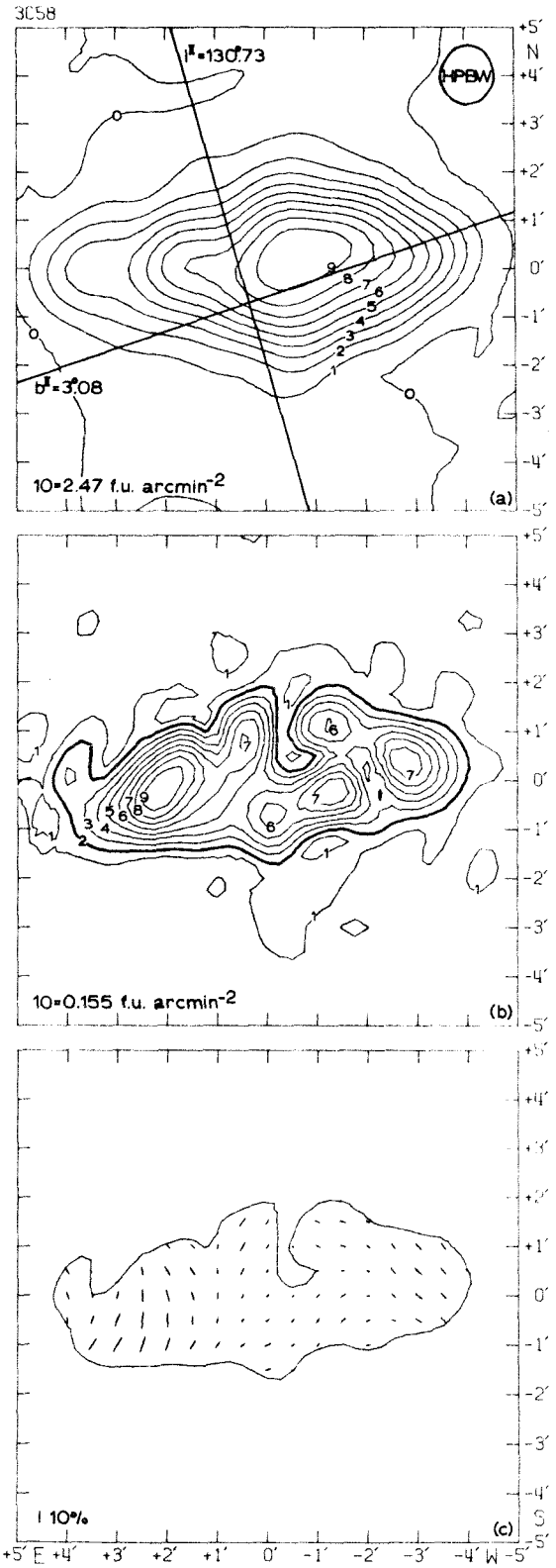
3C58
l^{II}=130°.73
b^{II}=3°.08
HPBW
10=2.47 f.u. arcmin^{-2}
(a)
10=0.155 f.u. arcmin^{-2}
(b)
1 10%
(c)
N
S
E
W
+5′ +4′ +3′ +2′ +1′ 0′ -1′ -2′ -3′ -4′ -5′

Figure 10

Distribution of the total intensity and polarization over 3C58 ($\alpha(1950.0) = 02^h01^m52^s.80$, $\delta(1950.0) = +64^\circ35'14''.0$) at 2880 MHz.

(a) Intensity of the total radiation; lines of Galactic longitude and latitude superposed; Half Power Beam Width shown in upper right hand corner; $10 = 2.26 * 10^{-26}$ W m^{-2} Hz^{-1} arcmin^{-2}.

(b) Intensity of the polarized radiation; 20% contour darkened; $10 = 0.24 * 10^{-26}$ W m^{-2} Hz^{-1} arcmin^{-2}.

(c) Position angle of the polarization; orientation of the line gives position of the electric vector; degree of linear polarization indicated by line length; line length appropriate for 10% polarization shown in lower left hand corner.

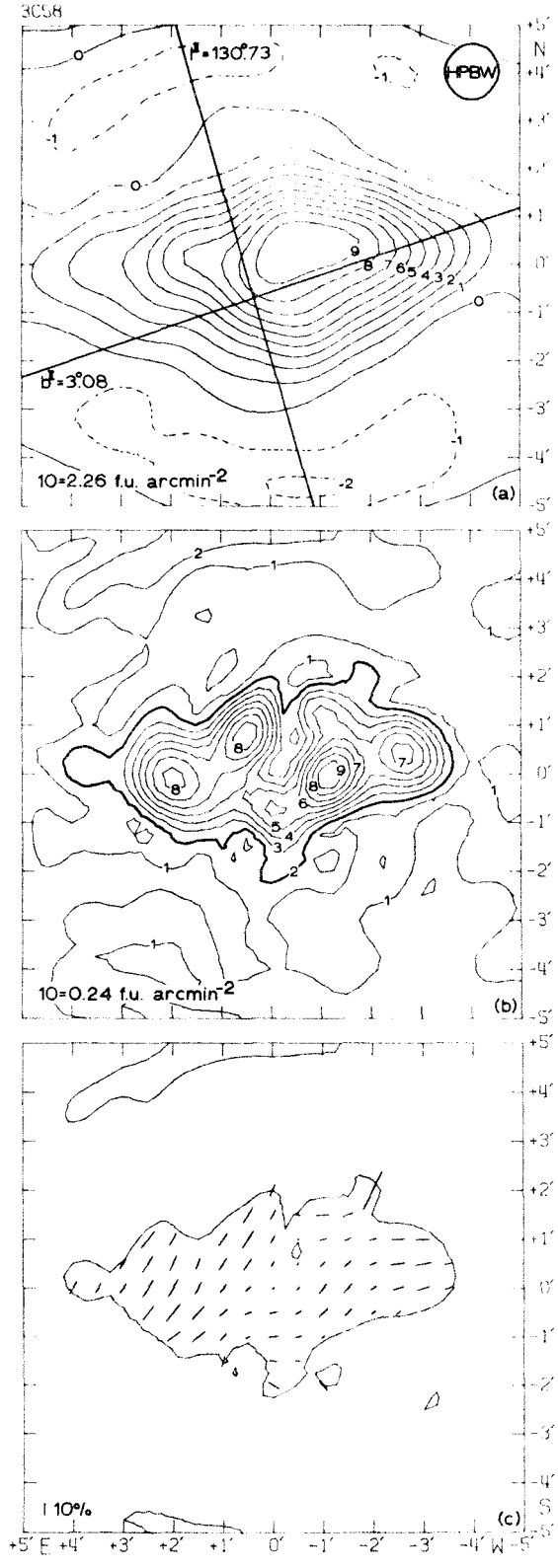
3C98
HPBW
10=2.26 f.u. arcmin^{-2}
(a)
10=0.24 f.u. arcmin^{-2}
(b)
1 10%
(c)
N
S
E
W

contour is chosen to delimit the polarized flux density distribution and is darkened. In the (c) diagram the line length appropriate to 10% polarization is displayed in the lower left hand corner.

Unlike 3C10, 3C58 is narrow enough in the N/S direction to be free from grating response distortion. The total flux density distribution varies smoothly with position, and shows little frequency dependence. The source exhibits a simple shape, brightest in the center and falling off slowly to zero on the edges. An elongation is evident in the E/W direction.

The situation is strikingly different in the polarized flux density distribution, however. The source exhibits considerable structure with the maps at both frequencies appearing remarkably similar. Several bright regions approach the limit of resolution of the synthesized beam, indicating that a higher resolution study may yield even more detail. The "bay" in the north-central area may result from the near orthogonality of the bordering position angles and the consequent cancelling of the polarized flux.

In its integrated properties, 3C58 is only weakly polarized ($0.8 \pm 0.6\%$ at 21.2 cm [36]) although when resolved it has polarizations exceeding 10% at 21.1 cm and 15% at 10.4 cm.

Again, a tabular display of the data is useful. Table XIV represents the 3C58 total intensity distribution in f.u. arcmin^{-2} at 21.1 cm for all values greater than the 10% contour. Each point has an error of approximately 0.07 f.u. arcmin^{-2}. Table XV contains the 21.1 cm percentage polarization and errors within an area bounded by the 20% contour of the polarized flux density distribution, while Table XVI

TABLE XIV. 1955 TOTAL INTENSITY DISTRIBUTION IN F.U. ARCMIN^{-2} AT 1420 MHZ ($I_{21.1}$)

δ	E +5°0	+4°5	+4°0	+3°5	+3°0	+2°5	+2°0	+1°5	+1°0	+0°5	0°0	−0°5	−1°0	−1°5	−2°0	−2°5	−3°0	−3°5	−4°0	−4°5	W −5°0
+5°0 N																					
+4°5																					
+4°0																					
+3°5																					
+3°0																					
+2°5											0.30 ± 0.07	0.37 ± 0.07	0.34 ± 0.07	0.25 ± 0.07							
+2°0								0.29 ± 0.07	0.32 ± 0.07	0.42 ± 0.07	0.63 ± 0.07	0.71 ± 0.07	0.63 ± 0.07	0.52 ± 0.07	0.43 ± 0.07	0.29 ± 0.07					
+1°5							0.35 ± 0.07	0.50 ± 0.07	0.57 ± 0.07	0.60 ± 0.07	1.17 ± 0.07	1.33 ± 0.07	1.24 ± 0.07	1.14 ± 0.07	1.01 ± 0.07	0.73 ± 0.07	0.41 ± 0.07				
+1°0			0.43 ± 0.07	0.48 ± 0.07	0.54 ± 0.07	0.81 ± 0.07	1.00 ± 0.07	1.05 ± 0.07	1.33 ± 0.07	1.79 ± 0.07	2.02 ± 0.07	2.00 ± 0.07	1.91 ± 0.07	1.70 ± 0.07	1.34 ± 0.07	0.93 ± 0.07	0.60 ± 0.07	0.31 ± 0.07		
+0°5	0.28 ± 0.07	0.46 ± 0.07	0.77 ± 0.07	0.79 ± 0.07	0.95 ± 0.07	1.34 ± 0.07	1.55 ± 0.07	1.57 ± 0.07	1.80 ± 0.07	2.20 ± 0.07	2.42 ± 0.07	2.43 ± 0.07	2.32 ± 0.07	2.08 ± 0.07	1.75 ± 0.07	1.39 ± 0.07	0.98 ± 0.07	0.52 ± 0.07			
0°0	0.40 ± 0.07	0.75 ± 0.07	0.92 ± 0.07	0.92 ± 0.07	1.13 ± 0.07	1.54 ± 0.07	1.76 ± 0.07	1.81 ± 0.07	2.02 ± 0.07	2.31 ± 0.07	2.42 ± 0.07	2.36 ± 0.07	2.19 ± 0.07	1.96 ± 0.07	1.72 ± 0.07	1.41 ± 0.07	0.97 ± 0.07	0.47 ± 0.07			
−0°5	0.32 ± 0.07	0.62 ± 0.07	0.77 ± 0.07	0.81 ± 0.07	0.96 ± 0.07	1.29 ± 0.07	1.47 ± 0.07	1.63 ± 0.07	1.91 ± 0.07	2.15 ± 0.07	2.19 ± 0.07	2.04 ± 0.07	1.80 ± 0.07	1.57 ± 0.07	1.34 ± 0.07	0.99 ± 0.07	0.57 ± 0.07				
−1°0		0.35 ± 0.07	0.46 ± 0.07	0.55 ± 0.07	0.67 ± 0.07	0.81 ± 0.07	0.93 ± 0.07	1.14 ± 0.07	1.42 ± 0.07	1.67 ± 0.07	1.75 ± 0.07	1.59 ± 0.07	1.29 ± 0.07	1.05 ± 0.07	0.81 ± 0.07	0.46 ± 0.07					
−1°5				0.30 ± 0.07	0.37 ± 0.07	0.41 ± 0.07	0.48 ± 0.07	0.61 ± 0.07	0.78 ± 0.07	0.99 ± 0.07	1.14 ± 0.07	1.01 ± 0.07	0.70 ± 0.07	0.47 ± 0.07	0.30 ± 0.07						
−2°0								0.30 ± 0.07	0.35 ± 0.07	0.47 ± 0.07	0.60 ± 0.07	0.50 ± 0.07	0.24 ± 0.07								
−2°5										0.26 ± 0.07	0.30 ± 0.07										
−3°0																					
−3°5																					
−4°0																					
−4°5 S −5°0																					

TABLE XV. 3C58 POLARIZATION DISTRIBUTION IN PERCENT AT 1420 MHZ ($P_{21.1}$)

	+5.0 E	+4.5	+4.0	+3.5	+3.0	+2.5	+2.0	+1.5	+1.0	+0.5	0.0	-0.5	-1.0	-1.5	-2.0	-2.5	-3.0	-3.5	-4.0	-4.5	-5.0 W
+5.0 N																					
+4.5																					
+4.0																					
+3.5																					
+3.0																					
+2.5																					
+2.0																					
+1.5										8.0 ± 1.6	4.6 ± 1.0		5.5 ± 1.0	5.7 ± 1.1	3.4 ± 1.2						
+1.0							4.7 ± 1.5	4.8 ± 1.2	4.0 ± 1.1	8.1 ± 1.0	3.9 ± 0.7	1.8 ± 0.6	4.5 ± 0.6	4.6 ± 0.6	3.9 ± 0.7	5.7 ± 0.9	6.6 ± 1.3	6.4 ± 2.1			
+0.5		0.6 ± 2.2				6.5 ± 1.3	8.3 ± 1.0	7.3 ± 0.8	5.0 ± 0.8	5.9 ± 0.7	2.9 ± 0.5		1.4 ± 0.5	2.8 ± 0.5	2.6 ± 0.6	6.5 ± 0.7	8.0 ± 0.9	7.1 ± 1.3	6.1 ± 2.4		
0.0		6.6 ± 1.7	3.4 ± 1.3	6.2 ± 1.3	10.6 ± 1.2	9.8 ± 0.9	7.2 ± 0.7	5.4 ± 0.7	4.0 ± 0.6	2.8 ± 0.5	2.2 ± 0.5	3.9 ± 0.5	5.1 ± 0.6	2.3 ± 0.6	5.0 ± 0.7	7.3 ± 0.9	6.9 ± 1.3				
-0.5		5.6 ± 2.0	6.8 ± 1.6	11.2 ± 1.8	14.0 ± 1.6	11.3 ± 1.1	6.9 ± 0.9	5.3 ± 0.8	3.7 ± 0.6	4.4 ± 0.6	4.1 ± 0.5	5.2 ± 0.6	5.8 ± 0.7	4.2 ± 0.8	3.5 ± 0.9	5.5 ± 1.2	6.3 ± 2.2				
-1.0			10.9 ± 3.1	12.9 ± 2.7	13.5 ± 2.3	10.7 ± 1.7	8.0 ± 1.4	5.7 ± 1.1	4.4 ± 0.8	5.5 ± 0.7	4.1 ± 0.7	2.7 ± 0.7	2.3 ± 0.9	3.6 ± 1.1							
-1.5										4.8 ± 1.2	2.9 ± 1.3										
-2.0																					
-2.5																					
-3.0																					
-3.5																					
-4.0																					
-4.5																					
-5.0 S																					

TABLE XVI. VLSR POSITION ANGLE DISTRIBUTION IN DEGREES AT 1420 MHZ ($PA_{21.1}$)

	+5.0 E	+4.5	+4.0	+3.5	+3.0	+2.5	+2.0	+1.5	+1.0	+0.5	0.0	-0.5	-1.0	-1.5	-2.0	-2.5	-3.0	-3.5	-4.0	-4.5 W	-5.0
+5.0 N																					
+4.5																					
+4.0																					
+3.5																					
+3.0																					
+2.5																					
+2.0																					
+1.5										145. ± 3.	146. ± 4.		66. ± 3.	73. ± 4.	67. ± 7.						
+1.0							43. ± 6.	46. ± 5.	168. ± 6.	150. ± 2.	148. ± 3.	49. ± 6.	64. ± 3.	73. ± 3.	57. ± 3.	43. ± 3.	43. ± 4.	38. ± 6.			
+0.5	27. ± 6.				14. ± 4.	32. ± 2.	35. ± 2.	4. ± 3.	156. ± 2.	146. ± 4.			89. ± 7.	97. ± 4.	61. ± 4.	44. ± 2.	45. ± 2.	46. ± 3.	90. ± 7.		
0.0	19. ± 5.	3. ± 8.	165. ± 4.	4. ± 2.	17. ± 2.	19. ± 2.	179. ± 3.	153. ± 3.	129. ± 3.	134. ± 4.	134. ± 2.	123. ± 2.	99. ± 5.	52. ± 3.	50. ± 2.	47. ± 3.					
-0.5	3. ± 7.	158. ± 4.	157. ± 3.	173. ± 2.	179. ± 2.	173. ± 2.	161. ± 3.	136. ± 3.	118. ± 2.	130. ± 2.	137. ± 2.	126. ± 2.	109. ± 4.	73. ± 5.	57. ± 4.	44. ± 6.					
-1.0		147. ± 5.	149. ± 3.	163. ± 3.	162. ± 3.	149. ± 3.	143. ± 3.	125. ± 4.	115. ± 3.	125. ± 3.	139. ± 5.	118. ± 8.	101. ± 6.								
-1.5									110. ± 5.												
-2.0																					
-2.5																					
-3.0																					
-3.5																					
-4.0																					
-4.5 S																					
-5.0																					

presents the position angle and error in degrees.

Similar information is shown for 3C58 at 10.4 cm in Tables XVII, XVIII, and XIX. Table XVII is bounded by the 10% contour of the total intensity distribution and has an individual point error of 0.18 f.u. arcmin^{-2}. Tables XVIII and XIX are bounded by the 20% contour of the 10.4 cm polarized flux density distribution and are presented in percentages and degrees, respectively.

Errors

Propagating the experimental and instrumental errors through the digital inversion was not only difficult but also unsatisfactory, and the actual error estimates were obtained by an indirect method. Before considering this, however, let us examine some of the origins and magnitudes of the data errors.

The phase and flux calibration, system noise errors, and confusion problems have been ably discussed by Fomalont [42] and will not be treated further here. Considering the calibrations for polarization measurements, Table XX lists the percentage polarization which would be measured in an unpolarized radio source if the settings or corrections were in error by one standard deviation. Horn Setting, Hour Angle and Circular Polarization, Hour Angle refer to the scatter of points at different hour angles about the average. The two rows given for each are the results determined for the two calibrators 3C295 and Cassiopeia A. Since 3C295 is by far the weaker, it has a much greater point scatter, causing the standard deviation in every case to be larger. Horn Setting, Declination and Circular Polarization, Declination refer to the scatter of the calibration sources about the straight line fit

TABLE XVII. 408 MHz TOTAL INTENSITY DISTRIBUTION IN F.U. ARCMIN^{-2} AT 2000 (1950.0)

	+5:0	+4:5	+4:0	+3:5	+3:0	+2:5	+2:0	+1:5	+1:0	+0:5	0:0	-0:5	-1:0	-1:5	-2:0	-2:5	-3:0	-3:5	-4:0	-4:5	-5:0
+5:0																					
+4:5																					
+4:0																					
+3:5																					
+3:0																					
+2:5																					
+2:0										0.28 ± 0.18	0.45 ± 0.18	0.51 ± 0.18	0.42 ± 0.18	0.28 ± 0.18							
+1:5								0.37 ± 0.18	0.47 ± 0.18	0.72 ± 0.18	1.07 ± 0.18	1.19 ± 0.18	1.07 ± 0.18	0.91 ± 0.18	0.74 ± 0.18	0.47 ± 0.18					
+1:0			0.22 ± 0.18	0.28 ± 0.18	0.37 ± 0.18	0.65 ± 0.18	0.85 ± 0.18	0.95 ± 0.18	1.28 ± 0.18	1.74 ± 0.18	1.93 ± 0.18	1.86 ± 0.18	1.72 ± 0.18	1.50 ± 0.18	1.12 ± 0.18	0.71 ± 0.18	0.44 ± 0.18	0.27 ± 0.18		
+0:5		0.31 ± 0.18	0.49 ± 0.18	0.54 ± 0.18	0.75 ± 0.18	1.11 ± 0.18	1.31 ± 0.18	1.39 ± 0.18	1.71 ± 0.18	2.11 ± 0.18	2.26 ± 0.18	2.23 ± 0.18	2.14 ± 0.18	1.92 ± 0.18	1.56 ± 0.18	1.15 ± 0.18	0.78 ± 0.18	0.45 ± 0.18		
0:0	0.30 ± 0.18	0.47 ± 0.18	0.60 ± 0.18	0.67 ± 0.18	0.89 ± 0.18	1.23 ± 0.18	1.42 ± 0.18	1.57 ± 0.18	1.90 ± 0.18	2.16 ± 0.18	2.17 ± 0.18	2.09 ± 0.18	1.99 ± 0.18	1.80 ± 0.18	1.52 ± 0.18	1.16 ± 0.18	0.77 ± 0.18	0.39 ± 0.18		
-0:5	0.26 ± 0.18	0.39 ± 0.18	0.49 ± 0.18	0.57 ± 0.18	0.76 ± 0.18	0.98 ± 0.18	1.13 ± 0.18	1.39 ± 0.18	1.78 ± 0.18	1.99 ± 0.18	1.94 ± 0.18	1.79 ± 0.18	1.61 ± 0.18	1.38 ± 0.18	1.10 ± 0.18	0.74 ± 0.18	0.40 ± 0.18			
-1:0			0.28 ± 0.18	0.40 ± 0.18	0.54 ± 0.18	0.63 ± 0.18	0.72 ± 0.18	0.99 ± 0.18	1.37 ± 0.18	1.60 ± 0.18	1.63 ± 0.18	1.47 ± 0.18	1.18 ± 0.18	0.89 ± 0.18	0.58 ± 0.18	0.26 ± 0.18				
-1:5					0.28 ± 0.18	0.32 ± 0.18	0.40 ± 0.18	0.60 ± 0.18	0.83 ± 0.18	1.03 ± 0.18	1.15 ± 0.18	1.02 ± 0.18	0.69 ± 0.18	0.40 ± 0.18						
-2:0								0.31 ± 0.18	0.41 ± 0.18	0.52 ± 0.18	0.61 ± 0.18	0.49 ± 0.18	0.23 ± 0.18							
-2:5																					
-3:0																					
-3:5																					
-4:0																					
-4:5																					
-5:0																					

TABLE XVIII. 3C58 POLARIZATION DISTRIBUTION IN PERCENT AT 2980 MHZ ($P_{10.4}$)

	+5.0 E	+4.5	+4.0	+3.5	+3.0	+2.5	+2.0	+1.5	+1.0	+0.5	0.0	-0.5	-1.0	-1.5	-2.0	-2.5	-3.0	-3.5	-4.0	-4.5	-5.0 W
+5.0 N																					
+4.5																					
+4.0																					
+3.5																					
+3.0																					
+2.5																					
+2.0											11. ± 8.				36. ± 45.						
+1.5										15. ± 6.	9. ± 3.	5. ± 3.	11. ± 3.	9. ± 4.							
+1.0						18. ± 12.	11. ± 5.	4. ± 4.	17. ± 4.	16. ± 3.	8. ± 2.	3. ± 2.	7. ± 2.	7. ± 2.	6. ± 2.	11. ± 3.	12. ± 5.				
+0.5		15. ± 15.		9. ± 6.	14. ± 5.	13. ± 3.	10. ± 3.	12. ± 3.	11. ± 2.	5. ± 1.	3. ± 1.	7. ± 1.	8. ± 2.	7. ± 2.	12. ± 2.	13. ± 3.	8. ± 4.				
0.0		12. ± 8.	10. ± 6.	10. ± 5.	17. ± 5.	17. ± 3.	12. ± 3.	9. ± 2.	7. ± 2.	3. ± 1.	5. ± 1.	11. ± 2.	11. ± 2.	7. ± 2.	9. ± 2.	11. ± 3.	8. ± 4.				
-0.5						15. ± 5.	18. ± 4.	15. ± 3.	9. ± 2.	7. ± 2.	7. ± 2.	7. ± 2.	10. ± 2.	8. ± 2.	5. ± 2.	5. ± 3.					
-1.0							13. ± 6.	14. ± 5.	9. ± 3.	5. ± 2.	9. ± 2.	7. ± 2.	4. ± 2.								
-1.5									8. ± 5.		7. ± 3.	6. ± 3.									
-2.0											11. ± 7.										
-2.5																					
-3.0																					
-3.5																					
-4.0																					
-4.5																					
-5.0 S																					

TABLE XIX. 3C58 POSITION ANGLE DISTRIBUTION IN DEGREES AT 2880 MHZ ($PA_{10.4}$)

DEC \ RA	+6:0 E	+4:5	+4:0	+3:5	+3:0	+2:5	+2:0	+1:5	+1:0	+0:5	0:0	-0:5	-1:0	-1:5	-2:0	-2:5	-3:0	-3:5	-4:0	-4:5	-5:0 W
+5:0 N																					
+4:5																					
+4:0																					
+3:5																					
+3:0																					
+2:5																					
+2:0											197. ± 12.				154. ± 10.						
+1:5										148. ± 5.	151. ± 6.	93. ± 12.	92. ± 5.	111. ± 7.							
+1:0						143. ± 8.	152. ± 7.	157. ± 12.	146. ± 5.	148. ± 3.	151. ± 4.	101. ± 12.	103. ± 5.	114. ± 5.	104. ± 6.	93. ± 5.	93. ± 7.				
+0:5		153. ± 11.		147. ± 10.	149. ± 5.	156. ± 4.	159. ± 4.	148. ± 3.	146. ± 3.	152. ± 5.	144. ± 9.	134. ± 3.	131. ± 3.	110. ± 5.	98. ± 3.	100. ± 4.	103. ± 10.				
0:0	149. ± 9.	149. ± 9.	144. ± 8.	148. ± 3.	150. ± 3.	150. ± 3.	141. ± 3.	129. ± 4.	119. ± 8.	139. ± 5.	141. ± 2.	137. ± 2.	121. ± 4.	108. ± 4.	108. ± 5.	109. ± 10.					
-0:5					144. ± 5.	142. ± 3.	139. ± 3.	131. ± 4.	110. ± 5.	101. ± 4.	122. ± 4.	136. ± 3.	135. ± 4.	127. ± 8.	125. ± 9.						
-1:0						127. ± 6.	129. ± 5.	137. ± 6.	111. ± 8.	98. ± 5.	107. ± 5.	122. ± 8.									
-1:5								164. ± 12.		83. ± 9.	83. ± 10.										
-2:0										97. ± 10.											
-2:5																					
-3:0																					
-3:5																					
-4:0																					
-4:5																					
-5:0 S																					

in declination.

TABLE XX. Polarization Error Estimates

Source of Error	21.1 cm		10.4 cm	
	0/90 Std.Dev.	45/135 Std.Dev.	0/90 Std.Dev.	45/135 Std.Dev.
Horn Setting, Hour Angle	0.17% 0.01%	0.14%(3C295) 0.02%(Cass A)	0.39% 0.13%	0.39%(3C295) 0.04%(Cass A)
Circular Polarization, Hour Angle	0.39% 0.01%	0.25%(3C295) 0.02%(Cass A)	0.38% 0.14%	0.39%(3C295) 0.08%(Cass A)
Horn Setting, Declination	0.12%	0.10%	0.39%	0.39%
Circular Polarization, Declination	0.13%	0.26%	0.32%	0.26%

Although a complete discussion of Faraday rotation will be deferred to the next chapter, it must be noted here that the position angle (PA_ν) of a linearly polarized cosmic radio wave has a wavelength dependence of the form

$$PA_\nu = PA0 + R_m \lambda^2 \tag{26}$$

where $PA0$ and R_m are constants. Since radio receivers with a finite bandwidth were used to collect the data, the possible effects must be considered.

The observed position angle ($\overline{PA}$) can be written as

$$\overline{PA} = \frac{\int PA_\nu \, R_\nu \, d\nu}{\int R_\nu \, d\nu} \tag{27}$$

where R_ν is the receiver bandpass function. It can easily be shown

from Equation (27) that if the receiver bandpass function R_ν is symmetric about some frequency ν_o, then $\overline{PA} = PA_{\nu_o}$. Thus, the use of a finite receiving bandwidth, if symmetric, introduces no error into the position angle measurements.

However, this rotation across the receiver bandwidth reduces the observed polarization (P) below the true value (p). For the small range of frequencies involved, p is frequency independent and the relation can be expressed as

$$P\, e^{2iPA_{\nu_o}} = \frac{\int p\, e^{2iPA_\nu} R_\nu d\nu}{\int R_\nu d\nu} \qquad (28)$$

where R_ν is the receiver bandpass function, PA_ν is defined in Equation (26), and PA_{ν_o} is the observed position angle.

Let us represent the actual receiver bandpass function R_ν by two equal Gaussians symmetrically placed about the observing frequency ν_o and separated from it by a frequency interval ν_1 with each Gaussian having a full width at half maximum of ν_2. Using this model in Equation (28), one arrives at the result

$$P = p \cos\{(4R_m c^2 \nu_1)/\nu_o^3\} \exp\{-(4R_m^2\, c^4 \nu_2^2)/(2.77\, \nu_o^6)\} \qquad (29)$$

where R_m is defined in Equation (26) and c is the velocity of light in vacuum. Employing the receiver parameters ($\nu_o = 1.42 * 10^9$ or $2.88 * 10^9$Hz; $\nu_1 = 10^7$Hz; $\nu_2 = 5 * 10^6$Hz) and a range of values for R_m sufficient to cover those encountered in the observations, the bandwidth depolarization factor was calculated and the results are shown in Table XXI.

TABLE XXI. Bandwidth Depolarization Factor

R_m (rad m^{-2})	Freq. (GHz)	Factor
±150	1.42	0.9815
±150	2.88	0.9997
±125	1.42	0.9872
±125	2.88	0.9998
±100	1.42	0.9918
±100	2.88	0.9999
± 75	1.42	0.9954
± 75	2.88	0.9999
± 50	1.42	0.9979
± 50	2.88	1.0000
± 25	1.42	0.9995
± 25	2.88	1.0000

As can be easily seen, the effect is completely negligible.

Another possible source of error is the Faraday rotation occurring in the ionosphere of the earth. This effect is difficult to determine since it varies with the time of day, the zenith angle, the time of year, and the solar cycle.

With the generous assistance of Mr. Brendan D. Mulhall of the Jet Propulsion Laboratory [45], who employed satellite data in conjunction with a model ionosphere program, it was determined that for an observing frequency of 1.42 GHz and an hour angle range of -4^h to $+4^h$ at a declination of $+64^\circ$, the ionospheric Faraday rotation varied from a minimum of $+0^\circ.5$ to a maximum of $+6^\circ.5$. The maximum occurs at large zenith angles in the early afternoon.

Because the inversion maps are the integrated result of many observations at numerous zenith angles and all times of the day, it is impossible to determine accurately the overall ionospheric effect. However, a rough calculation was made by estimating the rotation for each interpolated data point used in the inversion and taking the arithmetic mean of the values. This yields the result that all position angles at 21.1 cm are high by approximately $+2^{\circ}.5$. The effect at 10.4 cm is correspondingly less by a factor of λ^2 and is on the order of $+0^{\circ}.5$. These are systematic effects. However, due to their uncertainty and small magnitude, no corrections have been included in the present work.

All of the above mentioned data errors will manifest themselves as departures from zero in the inversion range where there is thought to be no emission. Following the methods of Fomalont [23], the errors for an inversion point on the four fundamental maps (I, U, Q, $\sqrt{U^2+ Q^2}$) were determined as the root mean square (RMS) average brightness external to the area of the source considered significant. These most basic errors, used as the origin for all other error estimates, are collected in Table XXII.

TABLE XXII. Basic Error Estimates

Source	21.1 cm (f.u. arcmin^{-2})	10.4 cm (f.u. arcmin^{-2})
3C10 I	$5.83 * 10^{-2}$	$1.07 * 10^{-1}$
3C10 U	$4.91 * 10^{-3}$	$1.24 * 10^{-2}$
3C10 Q	$5.44 * 10^{-3}$	$1.06 * 10^{-2}$
3C10 $\sqrt{U^2+Q^2}$	$7.33 * 10^{-3}$	$1.63 * 10^{-2}$
3C58 I	$7.48 * 10^{-2}$	$1.81 * 10^{-1}$
3C58 U	$8.60 * 10^{-3}$	$2.19 * 10^{-2}$
3C58 Q	$7.69 * 10^{-3}$	$1.75 * 10^{-2}$
3C58 $\sqrt{U^2+Q^2}$	$1.15 * 10^{-2}$	$2.80 * 10^{-2}$

Although $\sqrt{U^2+Q^2}$ is not truly an independent quantity, it was treated as such and its error derived from the inversion maps.

These basic values were propagated as statistically independent errors through any calculations to obtain all other error estimates.

CHAPTER VI

SECONDARY RESULTS

Because we have available observations with the same resolution at two frequencies, there is much additional information to be obtained.

Spectral Index

Through comparison of the total intensity maps, the spectral index (α) distribution can be computed. Using the sign convention of Kellermann et al. [46] ($I_\nu \propto \nu^{+\alpha}$), the values are displayed with errors in Tables XXIII and XXIV for 3C10 and 3C58, respectively. The 3C10 tables represent the area common to greater than the 10% contour on the 21.1 cm map and greater than the 20% contour on the 10.4 cm map. For 3C58, the boundaries are the 10% contours at both frequencies.

Inspecting the 3C10 distribution, a strong dependence of spectral index on position in the source is lacking. A striking feature is the rather steep spectrum exhibited for most areas as compared with the integrated result of -0.55 ± 0.02 found by Kellermann et al. [46]. The strongly positive spectral index values in the northern and southern regions are a physically unreal result of the grating response distortion at 10.4 cm mentioned earlier. From synchrotron theory, it is not possible to have a spectral index exceeding +1/3. Thus, any such values were neglected in all following calculations.

The 3C58 spectral index distribution also shows no strong dependence on position. There is, however, a tendency for the spectral index to be somewhat flatter in the central and south-central regions of the source with a steepening toward the outer edges. From Kellermann et al.

TABLE XXIII. 3C10 SPECTRAL INDEX DISTRIBUTION (α)

δ \ α	+5.0	+4.5	+4.0	+3.5	+3.0	+2.5	+2.0	+1.5	+1.0	+0.5	0.0	-0.5	-1.0	-1.5	-2.0	-2.5	-3.0	-3.5	-4.0	-4.5	-5.0
+5.0																					
+4.5											0.7 ± 0.6	0.6 ± 0.5	1.0 ± 0.5								
+4.0									0.3 ± 0.6	-0.0 ± 0.4	-0.1 ± 0.3	0.0 ± 0.3	0.1 ± 0.3	0.4 ± 0.3	1.1 ± 0.6						
+3.5							0.3 ± 0.9	0.0 ± 0.4	-0.3 ± 0.3	-0.3 ± 0.2	-0.3 ± 0.2	-0.2 ± 0.2	-0.2 ± 0.2	-0.1 ± 0.2	-0.0 ± 0.3	0.4 ± 0.4					
+3.0					-0.4 ± 0.9	-0.3 ± 0.4	-0.4 ± 0.2	-0.6 ± 0.2	-0.6 ± 0.2	-0.6 ± 0.2	-0.6 ± 0.3	-0.6 ± 0.3	-0.6 ± 0.2	-0.6 ± 0.2	-0.5 ± 0.2	-0.5 ± 0.3	-0.2 ± 0.4	0.3 ± 0.6			
+2.5					-0.7 ± 0.5	-0.7 ± 0.2	-0.8 ± 0.2	-1.0 ± 0.2	-1.2 ± 0.3	-1.5 ± 0.4	-1.8 ± 0.7	-1.6 ± 0.7	-1.3 ± 0.5	-1.0 ± 0.3	-0.9 ± 0.3	-0.8 ± 0.3	-0.5 ± 0.4	0.1 ± 0.8			
+2.0					-0.8 ± 0.3	-0.9 ± 0.2	-1.1 ± 0.2	-1.4 ± 0.3	-1.7 ± 0.5	-1.9 ± 0.7	-1.9 ± 0.8	-1.8 ± 0.8	-1.6 ± 0.7	-1.3 ± 0.5	-1.1 ± 0.3	-1.0 ± 0.3	-1.0 ± 0.4	-0.8 ± 0.7			
+1.5				-1.1 ± 0.8	-0.9 ± 0.3	-0.9 ± 0.2	-1.2 ± 0.3	-1.6 ± 0.5	-1.5 ± 0.5	-1.2 ± 0.5	-1.1 ± 0.4	-1.1 ± 0.5	-1.0 ± 0.5	-0.9 ± 0.4	-0.8 ± 0.4	-0.9 ± 0.3	-1.0 ± 0.3	-1.1 ± 0.5			
+1.0				-1.3 ± 0.6	-0.8 ± 0.2	-0.8 ± 0.2	-1.1 ± 0.4	-1.4 ± 0.6	-1.1 ± 0.5	-0.8 ± 0.5	-0.9 ± 0.5	-1.0 ± 0.5	-0.9 ± 0.5	-0.6 ± 0.4	-0.5 ± 0.3	-0.5 ± 0.3	-0.8 ± 0.3	-1.0 ± 0.4			
+0.5				-1.2 ± 0.5	-0.8 ± 0.2	-0.7 ± 0.2	-0.9 ± 0.3	-1.0 ± 0.5	-0.7 ± 0.5	-0.3 ± 0.5	-0.4 ± 0.6	-0.8 ± 0.7	-0.8 ± 0.6	-0.7 ± 0.4	-0.5 ± 0.3	-0.5 ± 0.3	-0.8 ± 0.3	-1.0 ± 0.3	-1.3 ± 0.8		
0.0				-1.1 ± 0.4	-0.8 ± 0.2	-0.7 ± 0.3	-0.9 ± 0.4	-1.0 ± 0.5	-0.6 ± 0.5	-0.1 ± 0.5	-0.1 ± 0.5	-0.3 ± 0.8	-0.8 ± 0.8	-0.7 ± 0.5	-0.5 ± 0.4	-0.5 ± 0.3	-0.9 ± 0.3	-1.2 ± 0.4	-1.4 ± 0.8		
-0.5			-1.6 ± 0.9	-1.1 ± 0.3	-0.9 ± 0.5	-0.7 ± 0.3	-0.9 ± 0.4	-1.2 ± 0.5	-1.0 ± 0.9	-0.6 ± 0.4	-0.5 ± 0.5			-0.8 ± 0.5	-0.4 ± 0.4	-0.3 ± 0.4	-0.9 ± 0.4	-1.3 ± 0.4			
-1.0				-1.2 ± 0.3	-0.6 ± 0.3	-0.8 ± 0.3	-0.9 ± 0.4	-1.2 ± 0.4	-1.3 ± 0.5	-1.0 ± 0.4	-0.8 ± 0.5			-0.9 ± 0.4	-0.4 ± 0.3	-0.4 ± 0.4	-0.9 ± 0.4	-1.5 ± 0.5			
-1.5				-1.2 ± 0.4	-1.0 ± 0.3	-0.5 ± 0.3	-1.0 ± 0.4	-1.2 ± 0.4	-1.3 ± 0.4	-1.0 ± 0.4	-0.8 ± 0.4	-1.0 ± 0.6	-1.4 ± 0.7	-1.3 ± 0.5	-0.9 ± 0.4	-0.9 ± 0.4	-1.1 ± 0.4	-1.5 ± 0.6			
-2.0				-1.1 ± 0.5	-1.0 ± 0.3	-1.0 ± 0.4	-1.2 ± 0.4	-1.4 ± 0.4	-1.6 ± 0.5	-1.5 ± 0.6	-1.2 ± 0.5	-1.3 ± 0.6	-1.7 ± 0.8	-1.7 ± 0.7	-1.4 ± 0.5	-1.2 ± 0.4	-1.1 ± 0.4	-1.1 ± 0.5			
-2.5				-0.9 ± 0.7	-0.9 ± 0.4	-0.9 ± 0.4	-1.1 ± 0.4	-1.3 ± 0.3	-1.5 ± 0.4	-1.9 ± 0.7	-1.8 ± 0.7	-1.6 ± 0.6	-1.5 ± 0.6	-1.3 ± 0.5	-1.0 ± 0.4	-0.9 ± 0.3	-0.8 ± 0.4	-0.4 ± 0.5			
-3.0					-0.6 ± 0.6	-0.5 ± 0.5	-0.6 ± 0.3	-0.7 ± 0.3	-0.8 ± 0.3	-0.9 ± 0.3	-0.9 ± 0.3	-0.8 ± 0.3	-0.6 ± 0.3	-0.5 ± 0.3	-0.4 ± 0.3	-0.4 ± 0.3	-0.3 ± 0.5	0.3 ± 0.9			
-3.5						0.3 ± 0.9	0.1 ± 0.4	-0.1 ± 0.3	-0.1 ± 0.2	-0.2 ± 0.2	-0.3 ± 0.2	-0.3 ± 0.2	-0.1 ± 0.2	-0.0 ± 0.3	-0.0 ± 0.3	-0.1 ± 0.5	0.2 ± 1.0			
-4.0								1.0 ± 0.6	0.6 ± 0.4	0.3 ± 0.3	0.1 ± 0.2	0.1 ± 0.2	0.2 ± 0.3	0.4 ± 0.4	0.6 ± 0.6						
-4.5										1.2 ± 0.6	0.7 ± 0.5	0.6 ± 0.6	1.0 ± 0.8								
-5.0																					

TABLE XXIV. 3C58 SPECTRAL INDEX DISTRIBUTION (@)

	E +5:0	+4:5	+4:0	+3:5	+3:0	+2:5	+2:0	+1:5	+1:0	+0:5	0:0	-0:5	-1:0	-1:5	-2:0	-2:5	-3:0	-3:5	-4:0	-4:5	W -5:0
+5:0																					
N +4:5																					
+4:0																					
+3:5																					
+3:0																					
+2:5																					
+2:0												-0.6 ± 0.9	-0.5 ± 0.6	-0.5 ± 0.5	-0.6 ± 0.6	-0.9 ± 0.9					
+1:5							-0.7 ± 1.2	-0.4 ± 0.7	-0.3 ± 0.6	-0.1 ± 0.4	-0.1 ± 0.3	-0.2 ± 0.2	-0.2 ± 0.3	-0.3 ± 0.3	-0.4 ± 0.4	-0.6 ± 0.6					
+1:0				-0.9 ± 1.2	-0.7 ± 0.9	-0.5 ± 0.7	-0.3 ± 0.4	-0.2 ± 0.3	-0.1 ± 0.3	-0.0 ± 0.2	-0.0 ± 0.2	-0.1 ± 0.1	-0.1 ± 0.1	-0.1 ± 0.2	-0.2 ± 0.2	-0.3 ± 0.2	-0.4 ± 0.4	-0.4 ± 0.6	-0.2 ± 1.0		
+0:5			-0.8 ± 0.8	-0.6 ± 0.5	-0.5 ± 0.5	-0.3 ± 0.4	-0.3 ± 0.2	-0.2 ± 0.2	-0.2 ± 0.2	-0.1 ± 0.2	-0.1 ± 0.1	-0.1 ± 0.1	-0.1 ± 0.1	-0.1 ± 0.1	-0.1 ± 0.1	-0.2 ± 0.2	-0.3 ± 0.2	-0.3 ± 0.3	-0.2 ± 0.6		
0:0		-0.4 ± 0.9	-0.7 ± 0.6	-0.6 ± 0.4	-0.5 ± 0.4	-0.3 ± 0.3	-0.3 ± 0.2	-0.3 ± 0.2	-0.2 ± 0.2	-0.1 ± 0.1	-0.1 ± 0.1	-0.2 ± 0.1	-0.2 ± 0.1	-0.1 ± 0.1	-0.1 ± 0.1	-0.2 ± 0.2	-0.3 ± 0.2	-0.3 ± 0.3	-0.3 ± 0.7		
-0:5		-0.3 ± 1.0	-0.7 ± 0.7	-0.6 ± 0.5	-0.5 ± 0.4	-0.4 ± 0.3	-0.4 ± 0.3	-0.4 ± 0.2	-0.2 ± 0.2	-0.1 ± 0.1	-0.1 ± 0.1	-0.2 ± 0.1	-0.2 ± 0.1	-0.2 ± 0.2	-0.2 ± 0.2	-0.3 ± 0.3	-0.4 ± 0.4	-0.5 ± 0.7			
-1:0				-0.7 ± 0.9	-0.6 ± 0.7	-0.3 ± 0.5	-0.4 ± 0.4	-0.4 ± 0.4	-0.2 ± 0.3	-0.0 ± 0.2	-0.1 ± 0.2	-0.1 ± 0.2	-0.1 ± 0.2	-0.1 ± 0.2	-0.2 ± 0.3	-0.4 ± 0.5					
-1:5						-0.4 ± 1.0	-0.3 ± 0.8	-0.2 ± 0.7	-0.0 ± 0.5	0.1 ± 0.3	0.1 ± 0.3	0.0 ± 0.2	0.0 ± 0.3	-0.0 ± 0.4	-0.2 ± 0.7						
-2:0									0.1 ± 0.9	0.3 ± 0.7	0.1 ± 0.5	0.0 ± 0.4	-0.0 ± 0.6								
-2:5																					
-3:0																					
-3:5																					
-4:0																					
-4:5																					
S -5:0																					

[46] the integrated spectral index is -0.10 ±0.03.

Rotation Measure

Reconsidering Equation (26) illustrating the frequency dependence the position angle, PA_ν is the observed position angle at frequency ν or wavelength λ, PAO is the position angle at $\lambda = 0$, the intrinsic position angle, and R_m is the rotation measure.

With the position angles available at two frequencies, it is possible to calculate the rotation measure distribution. Unfortunately, there is an ambiguity of $n\pi$ radians in any position angle. Using observations at 1.42 and 2.88 GHz, there is a consequent uncertainty of $\pm 93n$ rad m^{-2} in the rotation measure. To resolve this ambiguity, the integrated polarization results of other observers shown in Table XXV were used.

TABLE XXV. Integrated Position Angles

Source	ν (MHz)	λ (m)	PA_ν (°)	PA_ν (rad)	$PA_\nu+\pi$ (rad)	$PA_\nu-\pi$ (rad)	Ref.
3C10	4995	0.0600	122	2.129	5.271	-1.013	[39]
3C10	8350	0.0359	109	1.902	5.044	-1.240	[49]
3C10	1414	0.2120	139	2.426	5.568	-0.716	[36]
3C10	--	0.0375	116	2.025	5.167	-1.117	[47]
3C58	4995	0.0600	166	2.897	6.039	-0.245	[39]
3C58	--	0.0207	2	0.035	3.177	-3.107	[48]
3C58	8350	0.0359	178	3.107	6.249	-0.035	[49]
3C58	1414	0.2120	167	2.915	6.057	-0.227	[36]
3C58	--	0.0375	175	3.054	6.196	-0.088	[47]

The integrated position angle values have been plotted against the wavelength squared in Figure 11 for both 3C10 and 3C58. In each case the "best" series of points has been fitted with a straight line, the slope of which yields the integrated rotation measure and the zero

Figure 11

Determination of the approximate integrated rotation measure for 3C10 and 3C58.

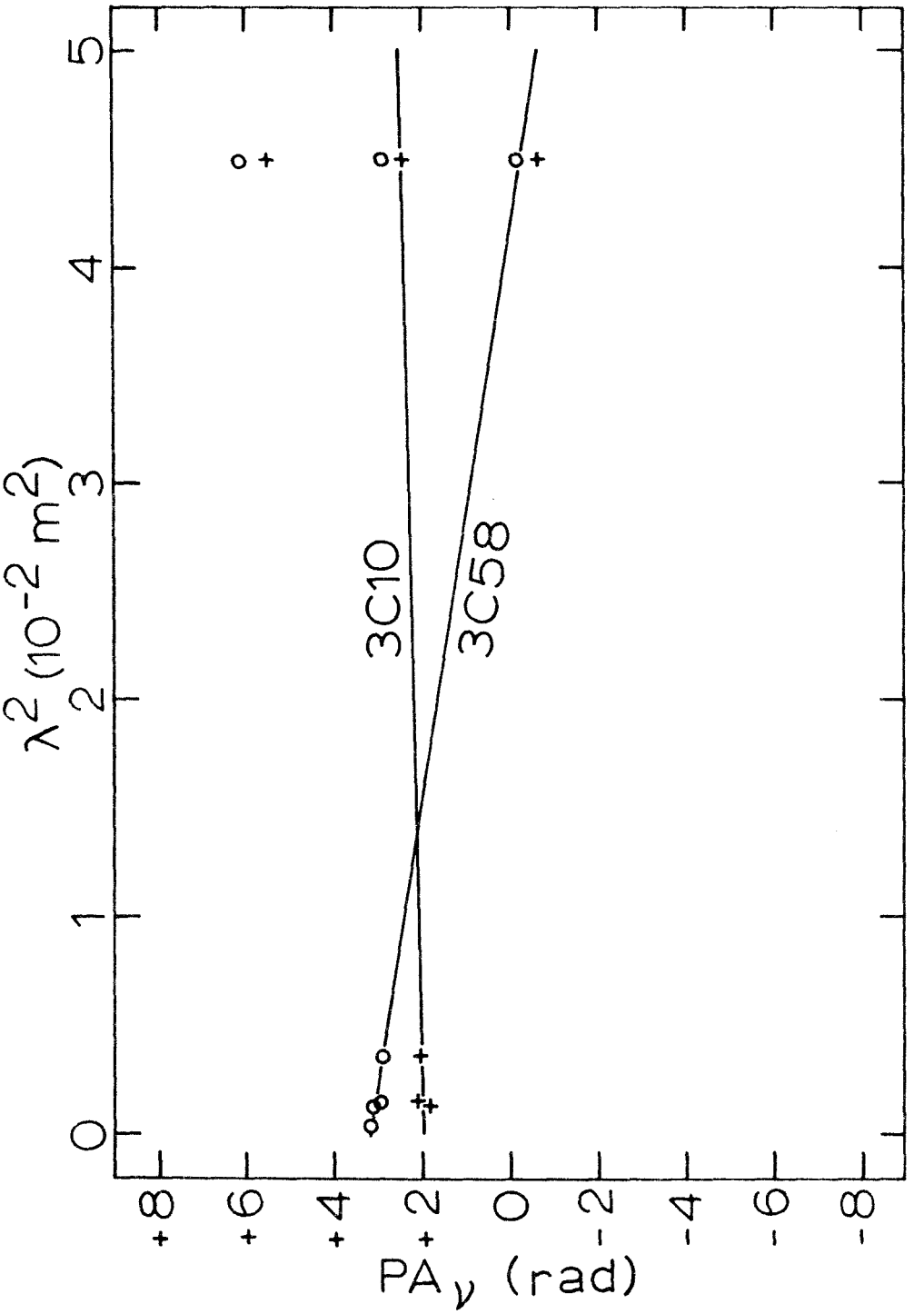
3C10
3C58
λ^2 (10^{-2} m^2)
PA$_\nu$ (rad)
0
1
2
3
4
5
+8
+6
+4
+2
0
-2
-4
-6
-8

intersect of which gives the integrated intrinsic position angle. These values were determined to be, for 3C10, R_m = 0 rad m^{-2}, PA0 = 113° and, for 3C58, R_m = -76 rad m^{-2}, PA0 = 2°. The rotation measure distributions were then calculated for each source by requiring the individual values to lie near the integrated results. Since the integrated rotation measures are quite uncertain, and since there is considerable leeway in adjusting the individual values lying near the extremes of the distribution, further constraints required that the intrinsic position angles vary slowly across the source and the rotation measure distribution contains no sharp discontinuities. These were expected due to beam-smoothing effects.

The rotation measure distributions for 3C10 and 3C58 are displayed in Tables XXVI and XXVII, respectively. Each entry is the rotation measure and error in rad m^{-2} .

The rotation measure distribution across 3C10 possibly increases up the eastern half and down the western half of the source, although this trend is not well defined. 3C58, on the other hand, displays a smooth increase of the rotation measure from east to west with little deviation. The significance of these variations will be discussed in more detail later.

Intrinsic Position Angle

Having determined the rotation measures, it is a simple matter to solve Equation (26) for the intrinsic position angles (PA0). For 3C10, Figure 12 presents a graphical display, while Table XXVIII presents the numerical values and errors in degrees. The same is given

TABLE XXVI. 3C10 ROTATION MEASURE DISTRIBUTION IN RAD M^{-2} (R_M)

K \ M	+5.0	+4.5	+4.0	+3.5	+3.0	+2.5	+2.0	+1.5	+1.0	+0.5	0.0	-0.5	-1.0	-1.5	-2.0	-2.5	-3.0	-3.5	-4.0	-4.5	-5.0
+5.0																					
+4.5																					
+4.0												57. ± 7.									
+3.5											54. ± 4.	57. ± 4.		35. ± 5.							
+3.0								59. ± 4.		31. ± 4.	44. ± 4.	48. ± 7.	25. ± 5.	33. ± 4.	39. ± 4.	36. ± 4.	34. ± 5.				
+2.5							66. ± 5.	60. ± 3.	51. ± 5.	32. ± 5.		24. ± 7.	19. ± 6.		46. ± 5.	39. ± 3.	37. ± 3.	38. ± 4.	38. ± 7.		
+2.0							47. ± 4.	49. ± 3.	49. ± 4.			33. ± 6.				45. ± 5.	42. ± 3.	41. ± 3.	37. ± 4.		
+1.5						32. ± 6.	33. ± 3.	40. ± 4.	46. ± 6.								47. ± 4.	45. ± 3.	44. ± 4.		
+1.0						25. ± 4.	28. ± 3.	38. ± 4.	48. ± 6.	59. ± 5.							54. ± 5.	51. ± 4.	49. ± 4.	48. ± 7.	
+0.5						25. ± 4.	30. ± 4.	39. ± 6.		57. ± 6.							63. ± 5.	57. ± 3.	52. ± 5.		
0.0						31. ± 5.	36. ± 6.										66. ± 4.	60. ± 3.	57. ± 4.		
-0.5																	71. ± 5.	66. ± 6.	64. ± 6.		
-1.0				33. ± 6.				25. ± 7.													
-1.5				31. ± 5.	35. ± 5.	44. ± 6.	31. ± 5.														
-2.0				19. ± 5.	28. ± 6.	43. ± 5.	35. ± 5.									65. ± 7.	-5. ± 6.	1. ± 6.	-6. ± 7.		
-2.5				6. ± 6.	19. ± 6.	34. ± 5.	30. ± 4.	23. ± 5.						52. ± 5.	53. ± 6.	78. ± 7.	6. ± 4.	9. ± 5.			
-3.0						25. ± 7.	24. ± 3.	21. ± 3.	14. ± 4.	6. ± 4.			45. ± 6.	56. ± 3.	62. ± 4.	5. ± 5.	13. ± 4.	18. ± 6.			
-3.5							18. ± 6.	21. ± 4.	10. ± 5.	1. ± 5.						8. ± 5.					
-4.0										-4. ± 6.											
-4.5																					
S -5.0																					

TABLE XXVII. SCAR RELATION MEASURE DISTRIBUTION IN RAD M^{-2} (R_M)

	+5.0 E	+4.5	+4.0	+3.5	+3.0	+2.5	+2.0	+1.5	+1.0	+0.5	0.0	-0.5	-1.0	-1.5	-2.0	-2.5	-3.0	-3.5	-4.0	-4.5 W	-5.0
+5.0 N																					
+4.5																					
+4.0																					
+3.5																					
+3.0																					
+2.5																					
+2.0																					
+1.5										-95. ± 3.	-96. ± 4.		-107. ± 3.	-113. ± 4.							
+1.0							-56. ± 5.		-81. ± 4.	-92. ± 2.	-95. ± 3.	-120. ± 7.	-113. ± 3.	-115. ± 3.	-118. ± 4.	-119. ± 3.	-119. ± 4.				
+0.5						-70. ± 3.	-64. ± 2.	-64. ± 3.	-74. ± 2.	-88. ± 2.	-96. ± 3.		-116. ± 4.	-110. ± 2.	-118. ± 3.	-121. ± 2.	-122. ± 2.	-124. ± 6.			
0.0			-67. ± 5.	-76. ± 6.	-82. ± 5.	-75. ± 2.	-69. ± 2.	-68. ± 2.	-73. ± 2.	-81. ± 3.	-88. ± 5.	-96. ± 3.	-97. ± 2.	-101. ± 2.	-105. ± 4.	-122. ± 3.	-123. ± 3.	-125. ± 9.			
-0.5						-78. ± 3.	-74. ± 2.	-75. ± 2.	-78. ± 2.	-80. ± 3.	-84. ± 3.	-89. ± 2.	-93. ± 2.	-98. ± 2.	-103. ± 4.	-120. ± 5.					
-1.0							-75. ± 3.	-93. ± 3.	-90. ± 4.	-86. ± 5.	-84. ± 3.	-84. ± 3.	-84. ± 5.								
-1.5											-79. ± 5.	-80. ± 6.									
-2.0																					
-2.5																					
-3.0																					
-3.5																					
-4.0																					
-4.5 S																					
-5.0																					

Figure 12

Intrinsic position angle of the electric vector for 3C10; delimiting 21.1 cm contour shown solid; delimiting 10.4 cm contour shown dashed; line length has no significance.

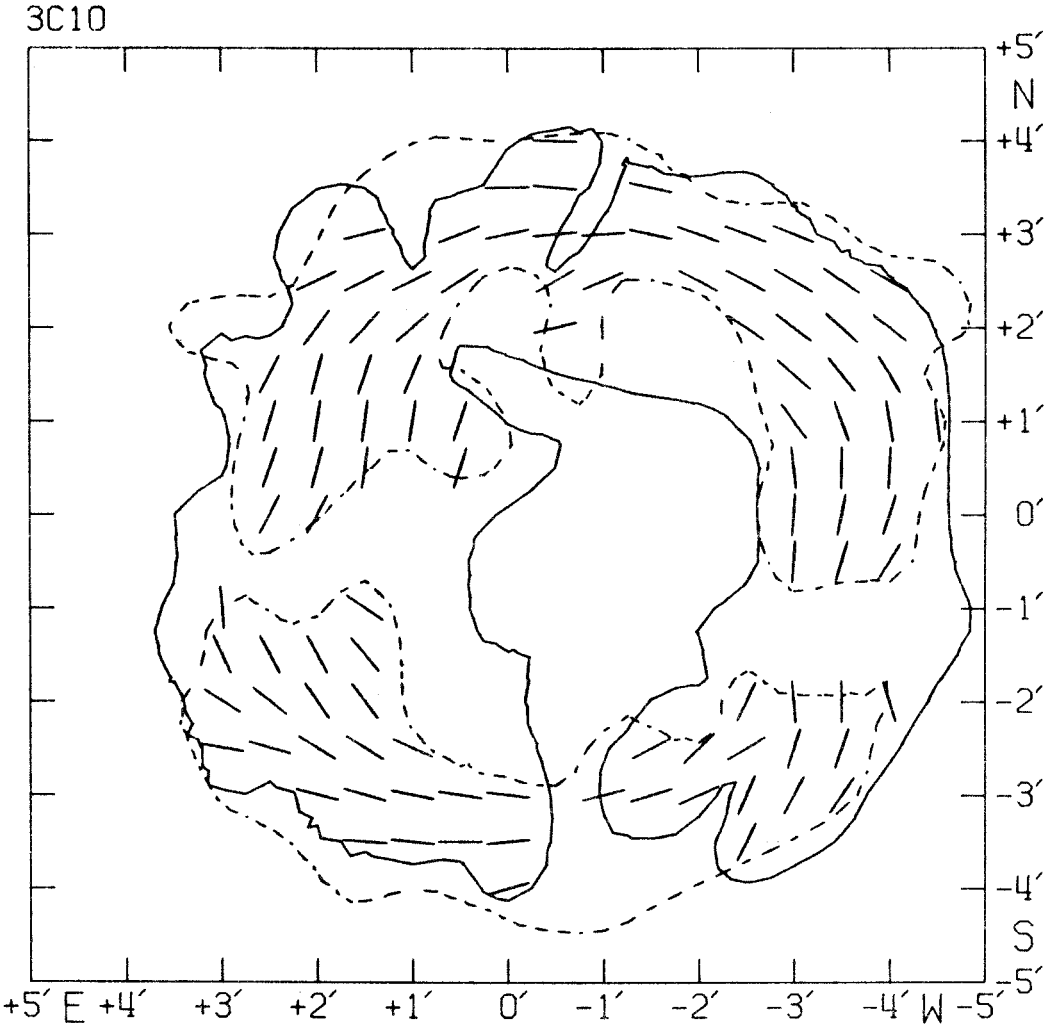
3C10
+5′
N
+4′
+3′
+2′
+1′
0′
-1′
-2′
-3′
-4′
S
-5′
+5′ E +4′ +3′ +2′ +1′ 0′ -1′ -2′ -3′ -4′ W -5′

TABLE XXVIII. SCIO INTRINSIC POSITION ANGLE DISTRIBUTION IN DEGREES (PA0)

	+5.0 E	+4.5	+4.0	+3.5	+3.0	+2.5	+2.0	+1.5	+1.0	+0.5	0.0	-0.5	-1.0	-1.5	-2.0	-2.5	-3.0	-3.5	-4.0	-4.5	-5.0 W
+5.0 N																					
+4.5																					
+4.0												88. ± 20.									
+3.5											91. ± 13.	85. ± 12.		77. ± 17.							
+3.0							105. ± 11.			112. ± 11.	102. ± 13.	96. ± 21.	94. ± 16.	77. ± 14.	69. ± 11.	68. ± 10.	67. ± 13.				
+2.5						116. ± 14.	116. ± 9.	117. ± 15.	124. ± 15.			121. ± 21.	114. ± 17.		61. ± 14.	62. ± 9.	58. ± 8.	55. ± 12.	59. ± 22.		
+2.0						144. ± 12.	138. ± 9.	132. ± 12.				104. ± 17.				55. ± 14.	52. ± 8.	47. ± 8.	51. ± 12.		
+1.5					153. ± 15.	165. ± 10.	162. ± 11.	157. ± 16.									48. ± 10.	38. ± 9.	30. ± 11.		
+1.0					164. ± 12.	171. ± 9.	172. ± 11.	171. ± 15.	162. ± 14.								35. ± 13.	20. ± 10.	10. ± 10.	7. ± 19.	
+0.5					161. ± 12.	165. ± 10.	172. ± 16.		162. ± 17.								7. ± 13.	179. ± 9.	177. ± 9.		
0.0					154. ± 13.	152. ± 17.											176. ± 12.	169. ± 9.	163. ± 11.		
-0.5																	175. ± 15.	164. ± 10.	149. ± 15.		
-1.0				5. ± 17.			55. ± 19.														
-1.5				25. ± 14.	27. ± 14.	28. ± 16.	39. ± 15.														
-2.0				57. ± 14.	51. ± 15.	34. ± 14.	36. ± 13.									155. ± 18.	5. ± 16.	1. ± 16.	17. ± 17.		
-2.5				79. ± 17.	74. ± 18.	58. ± 14.	57. ± 11.	66. ± 13.						119. ± 13.	135. ± 16.	122. ± 19.	162. ± 10.	161. ± 12.			
-3.0						75. ± 17.	74. ± 10.	79. ± 8.	81. ± 11.	83. ± 12.		105. ± 20.	108. ± 10.	115. ± 13.	157. ± 14.	152. ± 10.	147. ± 16.				
-3.5							85. ± 18.	84. ± 13.	90. ± 14.	96. ± 10.					154. ± 14.						
-4.0										107. ± 17.											
-4.5																					
-5.0 S																					

for 3C58 in Figure 13 and Table XXIX. Due to the ambiguity in the rotation measure, the intrinsic position angle is uncertain by $\mp 58n^{\circ}$. Thus the distributions shown here are not unique, but are the most reasonable for the data.

According to the theory of synchrotron radiation, a component of the magnetic field is orthogonal to the intrinsic position angle. Thus the 3C10 map (Figure 12) indicates the existence of an organized component of the magnetic field which is radial. Similar results have been found in the likewise ring-shaped supernova remnant Cassiopeia A by Mayer and Hollinger [21] at a frequency (λ = 1.55 cm) sufficiently high that the Faraday rotation is likely to be negligible. Since synchrotron radiation is not emitted along the magnetic field, a radial component will cause the central emission to be weak. This is observed in 3C10.

3C58 also displays a degree of uniformity in its magnetic field structure. Examination of Figure 13 reveals that, with little deviation, a component of the magnetic field runs parallel to the major east-west axis over the full extent of the source.

Assuming for the moment that both 3C10 and 3C58 are supernova remnants, the intrinsic position angle maps imply that the magnetic field structure in the sources has a partially organized component which is carried out with the matter in the explosion. Since the objects are probably of the same type (Type I supernovae) and are relatively close together in the galaxy, but do not resemble each other and do not expand preferentially along the galactic coordinates, it would seem that the interstellar matter and magnetic field, although certainly exerting some

Figure 13

Intrinsic position angle of the electric vector for 3C58; delimiting 21.1 cm contour shown solid; delimiting 10.4 cm contour shown dashed; line length has no significance.

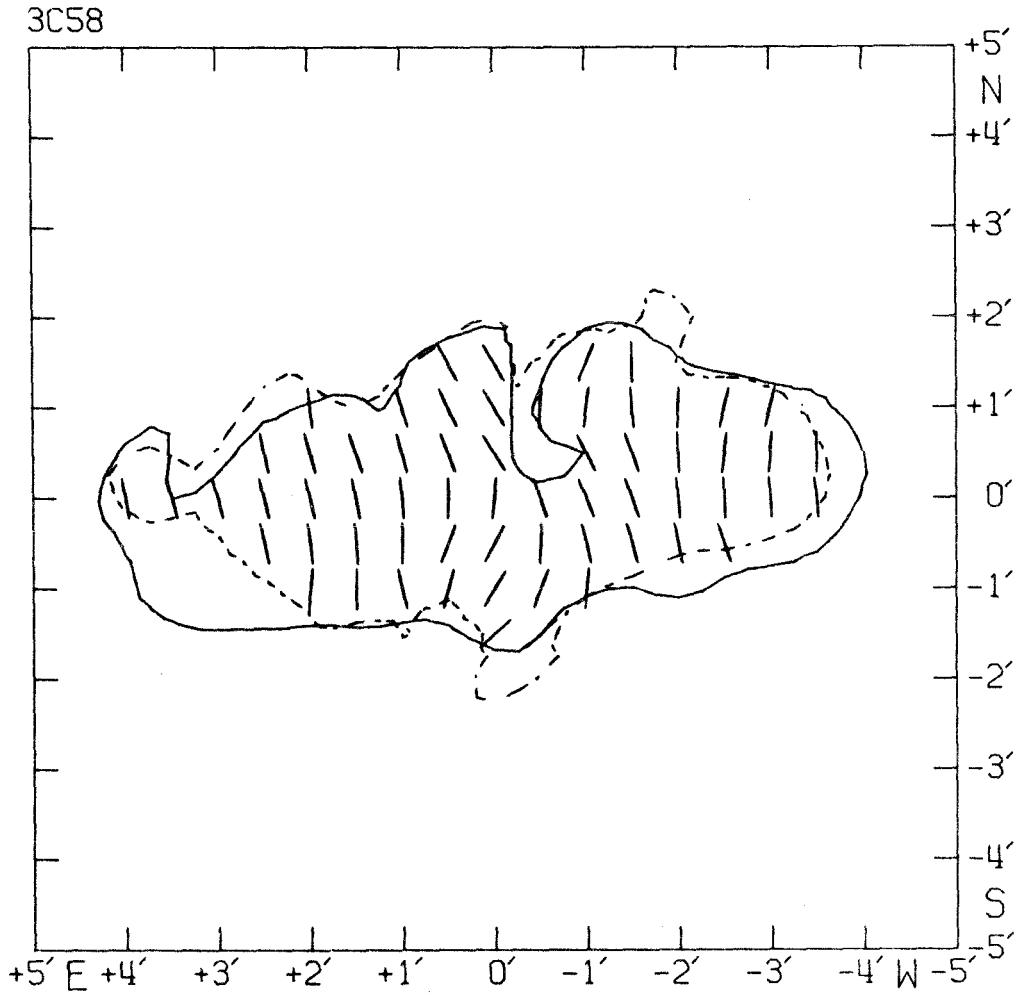
3C58
+5′
N
+4′
+3′
+2′
+1′
0′
-1′
-2′
-3′
-4′
S
-5′
+5′ E +4′ +3′ +2′ +1′ 0′ -1′ -2′ -3′ -4′ W -5′

TABLE XXIX. 2GEV INTRINSIC POSITION ANGLE DISTRIBUTION IN DEGREES (PA01

	+5.0 E	+4.5	+4.0	+3.5	+3.0	+2.5	+2.0	+1.5	+1.0	+0.5	0.0	-0.5	-1.0	-1.5	-2.0	-2.5	-3.0	-3.5	-4.0	-4.5	-5.0 W
+5.0 N																					
+4.5																					
+4.0																					
+3.5																					
+3.0																					
+2.5																					
+2.0																					
+1.5											27. ± 9.	30. ± 10.		158. ± 9.	1. ± 11.						
+1.0							7. ± 14.		16. ± 11.	25. ± 9.	30. ± 8.	175. ± 19.	173. ± 8.	5. ± 8.	177. ± 10.	167. ± 8.	166. ± 11.				
+0.5						12. ± 9.	16. ± 6.	13. ± 7.	15. ± 7.	20. ± 5.	31. ± 9.		26. ± 13.	19. ± 7.	3. ± 9.	173. ± 6.	176. ± 6.	179. ± 15.			
0.0			10. ± 15.	16. ± 18.	15. ± 12.	14. ± 6.	13. ± 4.	12. ± 5.	6. ± 6.	179. ± 7.	174. ± 12.	19. ± 9.	22. ± 5.	20. ± 5.	6. ± 11.	3. ± 7.	4. ± 7.	7. ± 14.			
-0.5						13. ± 7.	8. ± 5.	5. ± 4.	179. ± 7.	160. ± 8.	154. ± 7.	177. ± 7.	14. ± 5.	16. ± 6.	11. ± 12.	19. ± 15.					
-1.0							174. ± 9.	1. ± 8.	13. ± 10.	165. ± 12.	150. ± 7.	159. ± 8.	174. ± 14.								
-1.5											132. ± 15.	133. ± 17.									
-2.0																					
-2.5																					
-3.0																					
-3.5																					
-4.0																					
-4.5																					
-5.0 S																					

influence, are not dominant factors in determining the source properties. A similar conclusion was reached for Cassiopeia A by Mayer and Hollinger [21].

It should be noted, however, that this interpretation is not unique. The same magnetic field structures can be obtained in a model by Gardner and Whiteoak [50] from a compression of the interstellar magnetic field. A field directed primarily along the line of sight for 3C10 and primarily perpendicular to the line of sight for 3C58 would be required.

Depolarization

Employing the convention of Maltby [51], a measure of the depolarization was obtained by taking the ratio of the 21.1 cm polarization to the 10.4 cm polarization, $P_{21.1}/P_{10.4}$. The values calculated for 3C10 and 3C58 are shown in Tables XXX and XXXI, respectively.

Examination of the distributions for the two sources yields no obvious spatial dependences. Large and small values of the depolarization ratio seem to be scattered at random.

Correlations

In an attempt to find correlations, the measured source properties were plotted against one another. These results are shown in Table XXXII.

As can be seen, any correlations are very weak. There is a tendency for areas of higher brightness to exhibit a lower degree of polarization and, very tentatively, an implication that areas with a steep spectral index have a higher degree of polarization. However, there is in general no strong relation between the source parameters.

TABLE AAA. 3C10 DEPOLARIZATION DISTRIBUTION (ξ = ($P_{21.1}$/$P_{10.4}$))

	E +5.0	+4.5	+4.0	+3.5	+3.0	+2.5	+2.0	+1.5	+1.0	+0.5	0.0	-0.5	-1.0	-1.5	-2.0	-2.5	-3.0	-3.5	-4.0	-4.5 W -5.0
+5.0																				
N +4.5																				
+4.0												0.47 ± 0.32								
+3.5											0.27 ± 0.11	0.29 ± 0.11		0.20 ± 0.11						
+3.0								0.28 ± 0.11		0.20 ± 0.08	0.29 ± 0.13	0.14 ± 0.10	0.15 ± 0.08	0.17 ± 0.08	0.29 ± 0.12	0.49 ± 0.19	0.60 ± 0.20			
+2.5							0.43 ± 0.23	0.31 ± 0.10	0.11 ± 0.09	0.22 ± 0.12		0.12 ± 0.10	0.21 ± 0.16		0.34 ± 0.18	0.43 ± 0.15	0.40 ± 0.13	0.34 ± 0.16	0.37 ± 0.11		
+2.0							0.32 ± 0.14	0.41 ± 0.15	0.26 ± 0.12			0.15 ± 0.13				0.54 ± 0.28	0.44 ± 0.15	0.45 ± 0.17	0.45 ± 0.28		
+1.5						0.34 ± 0.18	0.32 ± 0.11	0.42 ± 0.18	0.34 ± 0.22								0.51 ± 0.21	0.50 ± 0.24	0.57 ± 0.32		
+1.0						0.31 ± 0.13	0.29 ± 0.07	0.41 ± 0.19	0.43 ± 0.29	0.26 ± 0.15							0.60 ± 0.32	0.67 ± 0.29	0.54 ± 0.24	0.23 ± 0.24	
+0.5						0.26 ± 0.10	0.30 ± 0.11	0.62 ± 0.38		0.46 ± 0.31							0.51 ± 0.27	0.52 ± 0.20	0.52 ± 0.21		
0.0						0.34 ± 0.15	0.45 ± 0.27										0.38 ± 0.18	0.38 ± 0.15	0.50 ± 0.23		
-0.5																	0.42 ± 0.25	0.27 ± 0.16	0.39 ± 0.24		
-1.0				0.50 ± 0.32				0.26 ± 0.18													
-1.5				0.49 ± 0.29	0.39 ± 0.22	0.34 ± 0.20	0.26 ± 0.15														
-2.0				0.43 ± 0.26	0.42 ± 0.24	0.36 ± 0.21	0.28 ± 0.15									0.28 ± 0.20	0.58 ± 0.36	0.85 ± 0.53	0.62 ± 0.44		
-2.5				0.25 ± 0.20	0.23 ± 0.14	0.29 ± 0.15	0.35 ± 0.16	0.47 ± 0.29						0.26 ± 0.16	0.47 ± 0.32	0.18 ± 0.12	0.43 ± 0.19	0.63 ± 0.32			
-3.0						0.22 ± 0.14	0.34 ± 0.13	0.41 ± 0.14	0.36 ± 0.14	0.37 ± 0.17		0.11 ± 0.07	0.25 ± 0.10	0.27 ± 0.13	0.24 ± 0.12	0.52 ± 0.22	0.54 ± 0.36			
-3.5							0.32 ± 0.10	0.36 ± 0.16	0.25 ± 0.12	0.29 ± 0.10						0.56 ± 0.30					
-4.0										0.38 ± 0.22											
-4.5 S -5.0																					

TABLE XXXI. 3C54 DEPOLARIZATION DISTRIBUTION ($\xi = (P_{21.1}/P_{10.4})^{1}$)

	+5.0	+4.5	+4.0	+3.5	+3.0	+2.5	+2.0	+1.5	+1.0	+0.5	0.0	-0.5	-1.0	-1.5	-2.0	-2.5	-3.0	-3.5	-4.0	-4.5	W -5.0
+5.0 N																					
+4.5																					
+4.0																					
+3.5																					
+3.0																					
+2.5																					
+2.0																					
+1.5										0.54 ± 0.23	0.54 ± 0.22		0.51 ± 0.19	0.66 ± 0.29							
+1.0							0.42 ± 0.24		0.33 ± 0.14	0.51 ± 0.12	0.52 ± 0.15	0.67 ± 0.43	0.66 ± 0.18	0.66 ± 0.19	0.63 ± 0.23	0.54 ± 0.18	0.56 ± 0.26				
+0.5					0.41 ± 0.16	0.62 ± 0.17	0.76 ± 0.22	0.44 ± 0.12	0.52 ± 0.11	0.56 ± 0.19			0.20 ± 0.06	0.35 ± 0.09	0.39 ± 0.13	0.57 ± 0.13	0.61 ± 0.16	0.94 ± 0.92			
0.0	0.54 ± 0.36	0.35 ± 0.24	0.62 ± 0.34	0.62 ± 0.18	0.59 ± 0.13	0.60 ± 0.14	0.58 ± 0.15	0.61 ± 0.18	0.90 ± 0.42	0.46 ± 0.16	0.36 ± 0.07	0.48 ± 0.09	0.34 ± 0.12	0.54 ± 0.15	0.65 ± 0.19	0.90 ± 0.91				
-0.5					0.93 ± 0.34	0.61 ± 0.16	0.47 ± 0.13	0.58 ± 0.17	0.54 ± 0.16	0.61 ± 0.15	0.59 ± 0.16	0.51 ± 0.11	0.69 ± 0.18	0.86 ± 0.40	0.68 ± 0.40						
-1.0						0.81 ± 0.38	0.57 ± 0.24	0.70 ± 0.31	0.87 ± 0.40	0.65 ± 0.18	0.57 ± 0.18	0.61 ± 0.33									
-1.5										0.73 ± 0.37	0.49 ± 0.32										
-2.0																					
-2.5																					
-3.0																					
-3.5																					
-4.0																					
-4.5 S																					
-5.0																					

TABLE XXXII. Search for Correlations

Source	X vs Y	Comments
3C10	21.1 cm % Polarization	Weak Correlation--High intensity implies low polarization.
	vs	
3C58	21.1 cm Total Intensity	Weak Correlation--High intensity implies low polarization.
3C10	10.4 cm % Polarization	Weak Correlation--High intensity implies low polarization.
	vs	
3C58	10.4 cm Total Intensity	Weak Correlation--High intensity implies low polarization.
3C10	Rotation Measure	No Correlation
	vs	
3C58	21.1 cm Total Intensity	No Correlation
3C10	Rotation Measure	No Correlation
	vs	
3C58	10.4 cm Total Intensity	No Correlation
3C10	Depolarization	No Correlation
	vs	
3C58	21.1 cm Total Intensity	No Correlation
3C10	Depolarization	No Correlation
	vs	
3C58	10.4 cm Total Intensity	No Correlation
3C10	21.1 cm % Polarization	No Correlation
	vs	
3C58	Rotation Measure	No Correlation
3C10	10.4 cm % Polarization	No Correlation
	vs	
3C58	Rotation Measure	No Correlation
3C10	21.1 cm % Polarization	No Correlation
	vs	
3C58	Spectral Index	Weak Correlation--Steep spectral index implies high polarization.
3C10	10.4 cm % Polarization	No Correlation
	vs	
3C58	Spectral Index	Weak Correlation--Steep spectral index implies high polarization.
3C10	Rotation Measure	No Correlation
	vs	
3C58	Spectral Index	No Correlation

TABLE XXXII, continued

3C10	Rotation Measure	No Correlation
	vs	
3C58	Depolarization	No Correlation
3C10	Depolarization	No Correlation
	vs	
3C58	Spectral Index	No Correlation

CHAPTER VII

SOURCE MODELS

3C10 Model

3C10 is the remnant of a Type I supernova first observed by Tycho Brahe in the year 1572. When modern observers searched for optical details, however, they were unsuccessful until it had been observed as a radio source in 1952 by Brown and Hazard [52]. Aided by this information, a few exceedingly faint details were found by Minkowski in 1959 [53]. Because of the dearth of this optical information, no estimate of the distance has been made from measurement of the proper motion and radial velocity of the filaments. The best present estimate is that obtained from the observations of 21 cm absorption lines by Menon and Williams (reported in [54])* which places the distance to 3C10 as 5000 pc†.

Calculating source properties on the basis of this value, 3C10 lies 124 pc above the Galactic plane, has a spectral power emitted of $1.3 * 10^{24}$ erg $sec^{-1}Hz^{-1}$, and a total power emitted in the radio region of $2.7 * 10^{34}$ erg sec^{-1}. The latter calculation assumes, as is normally true for supernova remnants, that the spectral index is constant for the entire radio range of 10^{7} to 10^{11} Hz.

With an E/W diameter of 8.'7 and a N/S diameter of 9.'4 to the 10% contour on the 21.1 cm total intensity map, a mean of 9.'1 was chosen to represent the source, yielding a diameter of 13.2 pc. From its two-

---

*A previous estimate by Menon and Williams [55] seems to have been superseded by the one found in Minkowski [54].

†1 pc = $3.0856 * 10^{18}$ cm

dimensional appearance, the model selected for 3C10 was a uniformly emitting spherical shell centered at 0.'5W, 0.'0N . Although thinner shells cannot be excluded, following the example of Minkowski [54] the shell thickness was chosen to be one-quarter of the radius giving an inner radius of 5.0 pc, an outer radius of 6.6 pc, and a volume of $2.1 * 10^{58} cm^3$. On the basis of this model, the line of sight path lengths through the source were calculated and are shown in Table XXXIII in cm.

Although some pulsars have been found in supernova remnants, a recent search in the vicinity of 3C10 by Reifenstein et al. [56] was unsuccessful.

3C58 Model

Little is known about 3C58 besides its integrated radio properties. No optical identification has been proposed, and a search of the Palomar Sky Survey prints for this present work proved fruitless. Most observers conclude that it is a Galactic source, but its nature is still in question. Higgs and Ramana [57] agree that there is no visible identification but are uncertain whether it is a thermal or a nonthermal source. Kellermann et al. [46] classify it as a supernova remnant, while Horton et al. [58] consider it to be a thermal source.

The object has a simple shape and it has been found by Fomalont [59] that simple shapes are relatively rare among extragalactic sources. Additionally, it is at a Galactic latitude of only $+3^{\circ}$ and has a relatively large angular size. Thus, it seems certain that 3C58 is a Galactic object. Because of its relatively high degree of

TABLE XXXIII. SCIO, LINE-OF-SIGHT PATH LENGTH THROUGH THE SOURCE IN UNITS OF 10^{19} CM (L)

	+5.0 F	+4.5	+4.0	+3.5	+3.0	+2.5	+2.0	+1.5	+1.0	+0.5	0.0	-0.5	-1.0	-1.5	-2.0	-2.5	-3.0	-3.5	-4.0	-4.5	-5.0 M
+5.0 N																					
+4.5																					
+4.0									1.4	1.7	1.9	1.9	1.9								
+3.5							1.3	1.9	2.2	2.4	2.6	2.6	2.6	2.4	2.2						
+3.0						1.5	2.1	2.5	2.2	1.8	1.6	1.6	1.6	1.8	2.2	2.5	2.1				
+2.5						2.1	2.6	1.8	1.5	1.4	1.3	1.3	1.3	1.4	1.5	1.8	2.6	2.1	1.3		
+2.0						2.5	1.8	1.5	1.3	1.2	1.2	1.2	1.2	1.2	1.3	1.5	1.8	2.5	1.9		
+1.5					2.2	2.2	1.5	1.3	1.2	1.1	1.1	1.1	1.1	1.1	1.2	1.3	1.5	2.2	2.2		
+1.0					2.4	1.8	1.4	1.2	1.1	1.1	1.1	1.0	1.1	1.1	1.1	1.2	1.4	1.8	2.4		
+0.5					2.6	1.6	1.3	1.2	1.1	1.1	1.0	1.0	1.0	1.1	1.1	1.2	1.3	1.6	2.6	1.9	
0.0					2.6	1.6	1.3	1.2	1.1	1.0	1.0	1.0	1.0	1.0	1.1	1.2	1.3	1.6	2.6	1.9	
-0.5				1.9	2.6	1.6	1.3	1.2	1.1	1.1	1.0	1.0			1.1	1.2	1.3	1.6	2.6		
-1.0					2.4	1.8	1.4	1.2	1.1	1.1	1.1	1.0			1.1	1.2	1.4	1.8	2.4		
-1.5					2.2	2.2	1.5	1.3	1.2	1.1	1.1	1.1	1.1	1.1	1.2	1.3	1.5	2.2	2.2		
-2.0					1.9	2.5	1.8	1.5	1.3	1.2	1.2	1.2	1.2	1.2	1.3	1.5	1.8	2.5	1.9		
-2.5					1.3	2.1	2.6	1.8	1.5	1.4	1.3	1.3	1.3	1.4	1.5	1.8	2.6	2.1	1.3		
-3.0						1.5	2.1	2.5	2.2	1.8	1.6	1.6	1.6	1.8	2.2	2.5	2.1	1.5			
-3.5								1.9	2.2	2.4	2.6	2.6	2.6	2.4	2.2	1.9	1.3				
-4.0												1.9	1.9	1.7							
-4.5																					
-5.0 S																					

polarization, one also concludes that 3C58 is a nonthermal (synchrotron) source.

According to Kesteven [60], Galactic sources with nonthermal spectral indices are generally considered to be supernova remnants. He finds that few of these exhibit a complete ring of emission but that the majority are consistent with a fraction of a shell. Minkowski [54] concludes that all Galactic nonthermal sources are probably supernova remnants and that a characteristic of a supernova remnant is a relatively flat spectrum. Poveda and Woltjer [61] require a supernova remnant to be both nonthermal and to exhibit either a clearly shell-like radio structure or an associated optical filamentary nebulosity. Even more restrictive, Milne and Hill [62] establish five conditions for a supernova remnant: (a) nonthermal radio spectrum, (b) large angular size, (c) within 250 pc of the Galactic plane, (d) filamentary structure if optically identified, and (3) radio shell structure.

3C58 satisfies the first three of these conditions for a supernova remnant. Optical identification obviously is a weak requirement. The lack of ring-like radio structure is more serious, but few suspected supernova remnants exhibit more than a hint of shell structure. Since the most famous remnant, the Crab Nebula (3C144, Taurus A), has no shell structure, it would indicate that such structure is sufficient but not necessary. Therefore, we conclude that 3C58 is probably a Galactic supernova remnant.

In order to determine a distance for 3C58, we utilize, with a correction by Minkowski [63], a purely radio astronomical method developed for supernova remnants by Shklovsky [64]. Assuming the radio

emission is synchrotron radiation, the distance d is related to the radio surface brightness I_ν and the apparent diameter ϕ by

$$d \propto W^{\frac{\beta+3}{3(\beta+2)}} H_{o\perp}^{-\frac{18+5\beta}{12(\beta+2)}} I_\nu^{-\frac{1}{\beta+2}} \phi^{-1} \tag{30}$$

where W is proportional to the energy released in the outburst, $H_{o\perp}$ is the magnetic field normal to the velocity vector of the relativistic electrons at some initial time, and β is related to the spectral index α by $\beta = 2(1-2\alpha)$. This relation is further simplified to

$$d \propto I^{-\frac{1}{\beta+2}} \phi^{-1}$$

or

$$d \propto I_\nu^{-\frac{0.25}{1-\alpha}} \phi^{-1} \tag{31}$$

by the assumption of approximately equal initial conditions in all supernovae. Unfortunately, this assumption is rather poor and Equation (30) is not very insensitive to the values of W and $H_{o\perp}$. Thus, the method cannot claim high accuracy. Nevertheless, Equation (31) has been used with the information on several supernova remnants at 21 cm shown in Table XXXIV to obtain a distance estimate for 3C58 of 4.6 ± 1.2 Kpc.

TABLE XXXIV. Supernova Remnants

Source	21 cm Flux Density	Area (arcmin^2)	I_{21} (f.u./arcmin^2)	α	ϕ (arcmin)	d (Kpc)
3C10	43.5[a]	65.4[c]	.665	-.55[b]	9.13[c]	5.0[d]
3C58	34.2[a]	38.9[c]	.880	-.10[b]	7.25[c]	?
Tau A	880[a]	30.2[f]	29.15	-.26[b]	6.20[f]	1.8[d]
3C358	16.3[a]	18.9[a]	.864	-.64[d]	4.90[a]	6.7[d]
Cass A	1590[b]	32.2[e]	32.17	-1.09[b]	6.40[e]	3.4[d]

a Fomalont [23]
b Kellermann et al. [46]
c Present results
d Minkowski [54]
e Ryle et al. [65]
f Mayer et al. [21]

An empirical method of estimating the distance to a supernova remnant advanced by Poveda and Woltjer [61] is based on the assumption that the surface brightness at 400 MHz is linearly related to the true diameter. Their result can be shown to be of the form

$$d \propto I_{\nu}^{k} \phi^{-1} \qquad (32)$$

where k is a free parameter to be determined. Assuming Equation (32) is valid at 21 cm and employing the data of Table XXXIV in several combinations of two sources, we obtain an average distance to 3C58 of 5.5 ± 2.2 Kpc.

Because of the large errors involved in these two estimates, only a very approximate distance determination has been obtained. Thus, using a convenient median value, the distance to 3C58 has been chosen as 5000 pc.

Calculations on the basis of this value imply that 3C58 lies 269 pc above the Galactic plane, has a spectral power emitted of $1.0 * 10^{24}$ erg $sec^{-1} Hz^{-1}$, and a total power emitted in the radio region of $7.4 * 10^{34}$ erg sec^{-1}. Again, it has been assumed that the spectral index is constant for the entire radio range of 10^{7} to 10^{11} Hz.

Measurements to the 10% contour on the 21.1 cm total intensity map yield an E/W diameter of 9.'0 (13.1 pc) and a N/S diameter of 5.'5 (8.0 pc). Choosing a uniformly filled prolate spheroidal model of these dimensions centered at 0.'0 E, 0.'0 N, the volume of 3C58 is $1.3 * 10^{58}$ cm^3. The line of sight path lengths through the source have been calculated on the basis of this model and are shown in Table XXXV in cm.

As for 3C10, a search for pulsars in the vicinity of 3C58 by Reifenstein et al. [56] was unsuccessful.

Synchrotron Theory

A theoretical study of the polarized emission from synchrotron sources has been performed by Korchak and Syrovatskii [15]. Unfortunately, knowledge of the intrinsic polarization is required and ignorance of the depolarization mechanism makes this unavailable. However, since the observed polarization is weak, an estimate of source parameters can be obtained by considering the unpolarized case of the source volume uniformly filled with relativistic electrons and random magnetic fields.

Following the treatment by Ginzburg and Syrovatskii [16],[66], we assume that the relativistic electron distribution is homogeneous

TABLE XXXV. 3C58, LINE-OF-SIGHT PATH LENGTH THROUGH THE SOURCE IN UNITS OF 10^{19} CM (L)

	E +5.0	+4.5	+4.0	+3.5	+3.0	+2.5	+2.0	+1.5	+1.0	+0.5	0.0	-0.5	-1.0	-1.5	-2.0	-2.5	-3.0	-3.5	-4.0	-4.5	W -5.0
N +5.0																					
+4.5																					
+4.0																					
+3.5																					
+3.0																					
+2.5																					
+2.0										1.7	1.7	1.7	1.6	1.5							
+1.5							1.8	1.9	2.0	2.0	2.1	2.0	2.0	1.9	1.8	1.6					
+1.0				1.3	1.6	1.8	2.0	2.1	2.2	2.3	2.3	2.3	2.2	2.1	2.0	1.8	1.6	1.3	0.7		
+0.5			1.0	1.5	1.8	2.0	2.2	2.3	2.4	2.4	2.4	2.4	2.4	2.3	2.2	2.0	1.8	1.5	1.0		
0.0		0.1	1.1	1.5	1.8	2.0	2.2	2.3	2.4	2.4	2.5	2.4	2.4	2.3	2.2	2.0	1.8	1.5	1.1		
-0.5			1.0	1.5	1.8	2.0	2.2	2.3	2.4	2.4	2.4	2.4	2.4	2.3	2.2	2.0	1.8	1.5			
-1.0				1.3	1.6	1.8	2.0	2.1	2.2	2.3	2.3	2.3	2.2	2.1	2.0	1.8					
-1.5						1.5	1.8	1.9	2.0	2.0	2.1	2.0	2.0	1.9	1.8						
-2.0									1.6	1.7	1.7	1.7	1.6								
-2.5																					
-3.0																					
-3.5																					
-4.0																					
-4.5																					
S -5.0																					

and isotropic with an energy spectrum of

$$N(E) = KE^{-\gamma} dE \tag{33}$$

where $N(E)$ is the number of relativistic electrons per unit volume with arbitrary directions of motion and energies in the interval $(E,E+dE)$. The intensity of radiation from this ensemble has been shown by these authors to be

$$I_\nu = a(\gamma) \left\{\frac{e^3}{mc^2}\right\} \left\{\frac{3e}{4\pi\, m^3c^5}\right\}^{\frac{\gamma-1}{2}} H^{\frac{\gamma+1}{2}} KL\, \nu^{-(\frac{\gamma-1}{2})}$$

or (34)

$$I_\nu = 1.35 * 10^{-22}\, a(\gamma)\, LK\, H^{\frac{\gamma+1}{2}} \left(\frac{6.26 * 10^{18}}{\nu}\right)^{\frac{\gamma-1}{2}} \text{ erg cm}^{-2}\text{sec}^{-1}\text{ster}^{-1}\text{Hz}^{-1}\,\dagger$$

where e is the electronic charge ($4.80 * 10^{-10}$ e.s.u.), m is the electronic mass ($9.11 * 10^{-28}$ gm), c is the speed of light in vacuum, ν is the observing frequency in Hz, L is the dimension of the radiating region along the line of sight in cm, K is the coefficient of the energy spectrum (see Equation (33)), H is an average value of the magnetic field in the radiating region in gauss, γ is the exponent of the energy spectrum (see Equation (33)), and $a(\gamma)$ is a coefficient equal to

$$a(\gamma) = \frac{2^{\frac{\gamma-1}{2}}\, \sqrt{3}\, \Gamma(\frac{3\gamma-1}{12})\, \Gamma(\frac{3\gamma+19}{12})\, \Gamma(\frac{\gamma+5}{4})}{8\sqrt{\pi}\, (\gamma+1)\, \Gamma(\frac{\gamma+7}{4})} \,. \tag{35}$$

$\dagger$ 1 erg cm^{-2}sec^{-1}ster^{-1}Hz^{-1} = $8.46 * 10^{15}$ f.u. arcmin^{-2}

In practice, for $\gamma > 1.5$, $a(\gamma)$ is evaluated by linear interpolation from Table XXXVI and for $\gamma < 1.5$, $a(\gamma)$ is taken equal to

$$a(\gamma) = 0.31\ (0.24)^{\frac{\gamma-1}{2}} \quad . \tag{36}$$

TABLE XXXVI. Synchrotron Coefficients†

γ	<1.5	1.0	1.5	2.0	2.5	3.0	4.0	5.0
$a(\gamma)$	----	0.283	0.147	0.103	0.0852	0.0742	0.0725	0.0922
$y_1(\gamma)$	0.24	0.80	1.3	1.8	2.2	2.7	3.4	4.0
$y_2(\gamma)$	0.24	0.00045	0.011	0.032	0.10	0.18	0.38	0.65

†From Ginzburg and Syrovatskii [66]

Examination of Equation (34) reveals that the radiation has a power law spectrum of spectral index

$$\alpha = (1-\gamma)/2 \quad . \tag{37}$$

Rewriting Equation (34) with $\nu = 1420$ MHz (21.1 cm) yields

$$I_{21.1} = a(\gamma)\ LK\ H^{\frac{\gamma+1}{2}}\ (4.41 * 10^9)^{\frac{\gamma-1}{2}}\ (8.77 * 10^5)\ \text{f.u. arcmin}^{-2} \quad . \tag{38}$$

An estimate of the energy density of relativistic electrons in the source may be obtained by integrating Equation (33)

$$W_e = \int_{E_1}^{E_2} E\ N(E)\ dE = K \int_{E_1}^{E_2} E^{-\gamma+1}\ dE \quad . \tag{39}$$

Ginzburg and Syrovatskii [66] find that the energy limits E_1 and

E_2 are related to the radio region frequency limits of $\nu_1(10^7 \text{Hz})$ and $\nu_2(10^{11} \text{Hz})$ by

$$E_1 \simeq 4.01 * 10^{-10} \{\nu_1 / y_1(\gamma)\ H\}^{1/2} \text{ erg} \tag{40}$$

and

$$E_2 \simeq 4.01 * 10^{-10} \{\nu_2 / y_2(\gamma)\ H\}^{1/2} \text{ erg}$$

where for $\gamma > 1.5$, $y_1(\gamma)$ and $y_2(\gamma)$ are tabulated in Table XXXVI and for $\gamma < 1.5$, $y_1(\gamma) \simeq y_2(\gamma) \simeq 0.24$. It should be noted that Equation (39) is a special case when $\gamma = 2$. Thus, for simplicity, only the more general case of $1/3 < \gamma < 2$ or $\gamma > 2$ is considered, giving

$$w_e = \left\{\frac{K}{2-\gamma}\right\} \{(1.27 * 10^{-4} y_2(\gamma)^{-.5}\ H^{-.5})^{2-\gamma} - (1.27 * 10^{-6} y_1(\gamma)^{-.5}\ H^{-.5})^{2-\gamma}\} \text{erg cm}^{-3} \tag{41}$$

It is generally thought that in a supernova remnant the energy density of the magnetic field $w_H = H^2/8\pi$ must, to some order of approximation, be equal to the energy density of the relativistic particles w_p. Not only is this the condition for which the system of fields and particles has near minimum energy, but also if the magnetic field energy were greatly smaller than the energy of the relativistic particles, a leakage of particles would occur until a state of energetic quasi-equilibrium was established. Thus it is reasonable to assume that $w_H = w_p$. However, radio observations only detect the relativistic electrons and positrons. Thus, the energy density of all particles must be related to the energy density of the electronic component to be useful. Following the example of Burbidge

and Burbidge [67], we have chosen the ratio of 100 so that

$$w_p = 10^2 \, w_e = H^2/8\pi \quad . \tag{42}$$

Combining Equations (38), (41), and (42) and solving for the magnetic field yields

$$H = \left[\left\{ \frac{I_{21.1} A(\gamma)}{a(\gamma) \, L} \right\} \{4.41 * 10^9\}^{\alpha} \left\{ \frac{2.20 * 10^9}{1 + 2\alpha} \right\} \{1.27 * 10^{-4}\}^{1+2\alpha} \right]^{2/7} \text{ gauss} \tag{43}$$

where

$$A(\gamma) = y_2(\gamma)^{-\left(\frac{1+2\alpha}{2}\right)} - 10^{-2(1+2\alpha)} \, y_1(\gamma)^{-\left(\frac{1+2\alpha}{2}\right)} \tag{44}$$

and α is the spectral index (see Equation (37)).

Determining $y_1(\gamma)$, $y_2(\gamma)$ and $a(\gamma)$ by the methods described above, and obtaining $I_{21.1}$ for 3C10 and 3C58 from Tables VIII and XIV, α from Tables XXIII and XXIV, and L from Tables XXXIII and XXXV, the values for the averaged magnetic field in the sources were calculated for all points at which the necessary information was available. The results are shown in Table XXXVII and Table XXXVIII for 3C10 and 3C58, respectively.

Solving Equations (41) and (42) for the coefficient of the energy spectrum K, the average total relativistic electron density

$$N_{et} = \int_{E_1}^{E_2} N(E) \, dE = K \int_{E_1}^{E_2} E^{-\gamma} \, dE \tag{45}$$

becomes

TABLE XXXVII. 3C10 AVERAGE TRANSVERSE MAGNETIC FIELD STRENGTH IN UNITS OF 10^{-4} GAUSS (MI

	+5.0 E	+4.5	+4.0	+3.5	+3.0	+2.5	+2.0	+1.5	+1.0	+0.5	0.0	-0.5	-1.0	-1.5	-2.0	-2.5	-3.0	-3.5	-4.0	-4.5	-5.0 W
+5.0 N																					
+4.5																					
+4.0									1.8	1.6	1.6	1.7	1.8								
+3.5							1.6	1.5	2.0	2.0	2.1	1.5	1.6	1.6	1.6						
+3.0						1.5	1.8	1.9	2.1	2.3	2.2	2.2	2.1	2.1	1.9	1.8	1.4				
+2.5						1.7	2.0	2.6	3.4	4.5	6.5	9.5	7.6	4.3	3.3	2.7	2.0	1.7	1.5		
+2.0						2.1	2.8	3.9	6.2	9.5	11.4	11.0	10.0	6.6	4.3	3.6	3.0	2.5	1.8		
+1.5					2.7	2.5	3.1	4.7	8.1	7.0	4.3	3.6	3.5	3.0	2.5	2.5	2.5	2.6	2.8		
+1.0					2.5	2.6	2.8	3.8	5.6	3.7	2.5	2.5	3.0	2.5	2.0	2.0	2.0	2.3	2.7		
+0.5					3.2	2.5	2.5	2.8	3.2	2.0	2.0	1.8	2.1	2.3	2.1	2.0	2.0	2.3	2.9	3.9	
0.0					2.8	2.5	2.3	2.7	3.1	1.9	1.6	1.6	1.7	1.9	2.1	2.0	1.9	2.5	3.3	4.2	
-0.5				5.9	3.2	2.7	2.3	2.9	4.1	3.2	2.0	1.9			2.3	2.0	2.0	2.5	4.0		
-1.0					3.9	3.0	2.4	2.7	4.4	4.8	3.1	2.4			2.8	2.0	1.9	2.6	5.1		
-1.5					3.9	2.9	2.7	3.0	4.4	5.0	3.3	2.3	2.8	5.7	4.5	2.7	2.4	3.4	5.4		
-2.0					3.2	2.7	3.1	4.1	5.8	7.7	6.2	3.9	4.6	8.5	8.4	5.1	3.6	3.3	3.0		
-2.5					2.3	2.2	2.3	3.4	4.8	7.3	11.1	9.9	7.6	6.2	4.3	3.0	2.3	2.1	1.7		
-3.0						1.6	1.6	1.7	2.1	2.5	2.7	2.9	2.5	2.1	1.8	1.7	1.7	1.8			
-3.5								1.6	1.5	1.5	1.5	2.2	2.2	1.6	0.8	1.6	1.5				
-4.0												1.9	1.8	1.9							
-4.5																					
-5.0 S																					

TABLE XXXVIII. SIGN AVERAGE TRANSVERSE MAGNETIC FIELD STRENGTH IN UNITS OF 10^{-4} GAUSS (H)

	+5.0 E	+4.5	+4.0	+3.5	+3.0	+2.5	+2.0	+1.5	+1.0	+0.5	0.0	-0.5	-1.0	-1.5	-2.0	-2.5	-3.0	-3.5	-4.0	-4.5	-5.0 W
+5.0 N																					
+4.5																					
+4.0																					
+3.5																					
+3.0																					
+2.5																					
+2.0										1.6	1.8	1.9	1.8	2.2							
+1.5							1.6	1.6	1.9	1.6	1.8	1.8	1.8	2.3	2.1	2.0					
+1.0				2.4	1.9	1.7	2.0	1.6	1.7	1.9	2.1	2.1	2.1	2.0	2.0	2.6	2.1	1.9	1.6		
+0.5			2.4	2.0	1.9	2.1	2.4	1.8	1.8	2.0	2.1	2.2	2.1	2.1	2.1	2.0	2.6	2.3	1.7		
0.0		3.3	2.2	2.1	2.0	2.1	2.3	2.4	1.9	2.0	2.1	2.1	2.1	2.1	2.1	2.0	2.5	2.2	2.2		
-0.5			2.1	2.0	1.9	2.0	2.1	2.2	1.8	2.0	2.1	2.0	2.0	1.9	1.9	2.4	2.0	1.8			
-1.0				1.9	1.8	2.0	1.9	1.9	1.7	1.9	2.0	2.0	1.9	1.8	1.7	1.9					
-1.5						1.6	1.7	1.4	1.6	1.8	1.9	2.0	1.9	1.7	1.4						
-2.0									1.5	1.8	1.8	1.7	1.6								
-2.5																					
-3.0																					
-3.5																					
-4.0																					
-4.5																					
S -5.0																					

$$N_{et} = \{H^{5/2}\}\{\frac{1+2\alpha}{2\alpha}\}\{\frac{1}{0.319}\}\{y_2(\gamma)^{-\alpha} - 10^{-4\alpha} y_1(\gamma)^{-\alpha}\} \text{ / A}(\gamma)\text{cm}^{-3} \quad . \quad (46)$$

These values were likewise calculated for both sources and are displayed in Table XXXIX for 3C10 and Table XL for 3C58.

A study of the tables of the magnetic field and relativistic electron density for 3C10 reveals a tendency for both to assume large values in the body of the annulus which taper off to smaller values near the inner and outer edges. This variation indicates that the uniformly filled spherical shell model of thickness one-quarter of the radius is a crude approximation at best. The source seems to have strong inhomogeneities requiring either a shell of different dimensions or a more complicated model. However, such a treatment is beyond the scope of the present work.

Except in the eastern region of the source, the equivalent tables for 3C58 show no such strong deviations, indicating that the uniformly filled prolate spheroidal model is a reasonable fit to the data.

From the above results, the total relativistic particle energy densities can be estimated ($w_p = w_H = H^2/8\pi$) and integrated over the source. Additionally, assuming that, as with the energy densities, the number density of heavy relativistic particles is 100 times the relativistic electron density ($N_{pt} = 10^2 N_{et}$) and that the heavy particles are mostly protons, the relativistic particle mass densities can be estimated and integrated over the source. Noting that the necessary information is not available for all cells of the source,

TABLE XXXIX. 3C10 AVERAGE TOTAL RELATIVISTIC ELECTRON DENSITY IN UNITS OF 10^{-8} CM^{-3}

	E +5.0	+4.5	+4.0	+3.5	+3.0	+2.5	+2.0	+1.5	+1.0	+0.5	0.0	-0.5	-1.0	-1.5	-2.0	-2.5	-3.0	-3.5	-4.0	-4.5	W -5.0
+5.0 N																					
+4.5																					
+4.0									0.	0.	0.	0.	0.								
+3.5							0.	0.	1.	1.	1.	0.	0.	0.	0.						
+3.0						1.	1.	2.	6.	10.	9.	8.	6.	5.	4.	2.	0.				
+2.5						5.	7.	18.	54.	136.	411.	1230.	670.	125.	53.	27.	9.	3.	0.		
+2.0						12.	29.	86.	344.	1170.	1980.	1780.	1400.	443.	128.	74.	42.	24.	9.		
+1.5					35.	20.	40.	158.	752.	502.	126.	68.	64.	40.	20.	19.	22.	28.	38.		
+1.0					78.	23.	26.	80.	269.	76.	20.	21.	38.	22.	7.	3.	4.	14.	33.		
+0.5					57.	19.	16.	30.	52.	9.	1.	2.	11.	17.	8.	3.	3.	14.	38.	109.	
0.0					57.	17.	12.	26.	44.	5.	0.	0.	1.	9.	10.	3.	3.	21.	61.	130.	
-0.5				348.	52.	25.	13.	34.	110.	51.	6.	5.			13.	2.	1.	20.	108.		
-1.0					94.	38.	16.	29.	131.	171.	42.	18.			32.	2.	1.	26.	224.		
-1.5					94.	37.	26.	42.	132.	195.	52.	14.	32.	289.	147.	27.	19.	62.	268.		
-2.0					51.	29.	45.	109.	298.	661.	369.	92.	159.	901.	856.	217.	78.	59.	45.		
-2.5					19.	15.	20.	62.	167.	562.	1850.	1360.	660.	361.	131.	43.	20.	11.	2.		
-3.0						4.	3.	4.	10.	19.	28.	29.	19.	8.	3.	2.	2.	1.			
-3.5								0.	0.	0.	0.	1.	1.	0.	0.	0.	0.				
-4.0												0.	0.	0.							
-4.5																					
S -5.0																					

TABLE XL. 3C58 AVERAGE TOTAL RELATIVISTIC ELECTRON DENSITY IN UNITS OF 10^{-6} CM^{-3}

N \ E	+5.0	+4.5	+4.0	+3.5	+3.0	+2.5	+2.0	+1.5	+1.0	+0.5	0.0	-0.5	-1.0	-1.5	-2.0	-2.5	-3.0	-3.5	-4.0	-4.5	-5.0 W
+5.0 N																					
+4.5																					
+4.0																					
+3.5																					
+3.0																					
+2.5																					
+2.0											2.8	2.2	2.6	4.3	15.9						
+1.5							4.9	1.5	0.7	0.4	0.5	0.5	0.6	1.4	2.6	5.9					
+1.0				20.6	7.6	2.8	1.0	0.5	0.4	0.4	0.5	0.6	0.6	0.6	0.7	1.2	2.1	2.3	0.4		
+0.5			17.0	6.6	2.8	1.4	1.2	0.6	0.5	0.5	0.6	0.6	0.7	0.7	0.6	0.7	1.4	1.6	0.5		
0.0		8.5	9.5	6.3	2.7	1.5	1.6	1.6	0.6	0.6	0.6	0.7	0.7	0.7	0.6	0.7	1.4	1.6	0.8		
-0.5			8.5	6.6	2.8	1.7	2.0	2.1	0.6	0.5	0.6	0.7	0.7	0.6	0.6	1.3	2.2	3.1			
-1.0				7.2	1.9	1.0	1.4	1.5	0.5	0.4	0.5	0.5	0.5	0.5	0.5	2.4					
-1.5						1.1	0.8	0.3	0.3	0.3	0.3	0.4	0.3	0.3	0.3						
-2.0									0.2	0.2	0.2	0.3	0.3								
-2.5																					
-3.0																					
-3.5																					
-4.0																					
-4.5																					
-5.0 S																					

for a volume of $1.8 * 10^{58}$ cm^3, 3C10 has a total relativistic particle energy of $8.8 * 10^{49}$ ergs and a total relativistic particle mass of $3.0 * 10^{30}$ gm or $1.5 * 10^{-3}$ $M_\odot$. Similarly, for a volume of $1.1 * 10^{58}$ cm^3, 3C58 has a total relativistic particle energy of $1.7 * 10^{49}$ ergs and a total relativistic particle mass of $2.9 * 10^{28}$ gm or $1.5 * 10^{-5}$ $M_\odot$.

At present, supernovae are generally classified into two categories (see, e.g. Shklovsky [68]). A Type II supernova is the violent explosion of a massive, young Population I star and a Type I supernova is the less energetic eruption of an old, small mass Population II star. Since the energy and mass of relativistic particles involved are even smaller than for 3C10, the remnant of a Type I supernova, 3C58 is almost certainly also the remnant of a Type I supernova.

Correlations

An attempt was made to correlate the magnetic field distribution and the relativistic electron density distribution with other source properties. As is seen in Table XLI, the results were negative.

TABLE XLI. Search for Correlations

Source	X vs Y	Comments
3C10	21.1 cm % Polarization	No Correlation
	vs	
3C58	Magnetic Field	No Correlation
3C10	10.4 cm % Polarization	No Correlation
	vs	
3C58	Magnetic Field	No Correlation
3C10	Depolarization	No Correlation
	vs	
3C58	Magnetic Field	No Correlation
3C10	Rotation Measure	No Correlation
	vs	
3C58	Magnetic Field	No Correlation
3C10	Depolarization	No Correlation
	vs	
3C58	Rel. Electron Density	No Correlation
3C10	Rotation Measure	No Correlation
	vs	
3C58	Rel. Electron Density	No Correlation

Rotation Measure

For a linearly polarized electromagnetic wave traveling through a magneto-ionic medium, the transmission velocities of the two senses of circular polarization are unequal, causing a shift in the relative phase and an effective rotation of the plane of polarization. This effect is generally expressed as a frequency independent rotation measure (R_m)

$$R_m = \psi/\lambda^2 = 2.62 * 10^{-13} \int N_{th} B_L \, dL \text{ rad m}^{-2} \dagger \qquad (47)$$

†See, e.g. Gardner and Whiteoak [69].

where N_{th} is the thermal electron density in cm^{-3}, B_L is the longitudinal component of the magnetic field in gauss, L is the path length in cm, Ψ is the angle of rotation in radians ($\Psi = PA_\nu - PA0$), and λ is the wavelength in meters.

The origin of this Faraday rotation is not completely clear although most authors (Gardner and Davies [70], Seielstad *et al.* [71], Gardner and Whiteoak [72]) conclude that the greatest part occurs in the interstellar medium. Let us consider a source at a distance of 5000 pc with a rotation measure of 100 rad m^{-2}. Equation (47) yields an average along the line-of-sight of $\langle N_{th} B_L \rangle = 2.5 * 10^{-8}$ gauss cm^{-3}. If the interstellar density is 10^{-1} hydrogen atoms per cm^3 and 10% of these are ionized, $\langle N_{th} \rangle = 10^{-2}$ cm^{-3} and $\langle B_L \rangle = 2.5 * 10^{-6}$ gauss. From measurements on pulsars, line-of-sight averages for the magnetic field have been found to be of this order (Smith [73], Radhakrishnan *et al.* [74], Ekers *et al.* [75]). Thus, it is easily possible to have an interstellar origin for the observed rotation measures.

Another approach has been suggested by Milne [76] for Vela X. He assumes the source has sufficient symmetry that the average rotation measure represents the rotation in the interstellar medium and the deviations from this average arise within the source. Areas with a rotation measure greater than the average contain a magnetic field component directed towards the observer and areas with a rotation measure less than the average contain a magnetic field component directed away from the observer.

Considering the individual sources, 3C10, with a median value of approximately +35 rad m^{-2}, shows considerable change of rotation

measure with position. This is most easily explained as a small scale variation of the longitudinal component of the magnetic field within the source itself. On the other hand, the slow variation of the rotation measure across 3C58 seems to indicate a large scale gradient in the interstellar magnetic field and/or electron density. Thus, no general conclusions about the cause of Faraday rotation can be drawn from the present, seemingly conflicting, results.

Depolarization

The origin of the depolarization seen in most radio sources has been a subject of controversy. Some authors contend that it is mainly a Galactic effect [36], [72], [77], [78], [79], while others consider it to arise within the source [51], [69], [71], [80].

In general, there seem to be three possibilities:

a) Galactic Faraday depolarization. If this were the case, one might expect a correlation with rotation measure which has not been found, a correlation with Galactic latitude which is disputed, and a correlation with source size which has not been found.

b) Source spectral depolarization. This would occur if the regions with steep spectra were less strongly polarized than those with flat spectra. This has not been found. In fact, Table XXXII indicates a slight tendency for the opposite to be true.

c) Source Faraday depolarization. This possibility of emission and rotation occurring together throughout the source cannot be eliminated by the lack of correlation between polarization properties and other source parameters. The observed emission arises from the transverse magnetic fields and the relativistic electron density, while

Faraday rotation originates in the longitudinal magnetic fields and thermal electron density.

Considering case (c) in more detail, and following a treatment similar to the "rectangular slab" model by Gardner and Whiteoak [69], a "pin cushion" model made up of an array of uniformly emitting and rotating rods is proposed. The polarized emission from one rod arriving through a magneto-ionic medium can be written as

$$P_\lambda \exp[2i(PA_\nu - R_m\lambda^2)] = \frac{\int_0^L p_\lambda(r)\,\varepsilon_\lambda(r)\,\exp[2i(\chi_\lambda(r)+\psi_\lambda(r))]A\,dr}{\int_0^L \varepsilon_\lambda(r)\,A\,dr} \qquad (48)$$

where P_λ is the observed fractional polarization, PA_ν is the observed position angle, R_m is the interstellar rotation measure, r is the depth of a volume element from the surface of the source, $p_\lambda(r)$ is the intrinsic fractional polarization at depth r in the source, $\varepsilon_\lambda(r)$ is the emissivity at depth r, $\chi_\lambda(r)$ is the position angle of the emitted radiation at depth r, $\Psi_\lambda(r)$ is the rotation of the radiation emitted at depth r before reaching the surface of the source [$\Psi_\lambda(r) = (2.62 * 10^{-13})\lambda^2 N_{th} B_L r$], A is the end area of the rod ($0.'5^2 = 5.04 * 10^{36}$ cm^2 @ 5 Kpc), and L is the line-of-sight length through the source.

Since the rods are assumed to be uniform throughout and since the intrinsic fractional polarization and intrinsic position angle are frequency independent,

$$\begin{aligned} \varepsilon_\lambda(r) &= \varepsilon_\lambda \\ p_\lambda(r) &= p \\ \chi_\lambda(r) &= \chi \quad . \end{aligned} \qquad (49)$$

Performing the integration and rewriting gives

$$P_\lambda \exp(2i\ PA_\nu) = \{p\ \exp(2i\chi)\}\left\{\frac{\exp[2i(R_m\lambda^2 - \frac{\pi}{4})]}{2C\lambda^2}\right\}\{\exp(2iC\lambda^2) - 1\} \qquad (50)$$

where $C = (2.62 * 10^{-13})L\ N_{th}B_L$. Solving for the spectral polarization yields

$$P_\lambda = \left\{\frac{p}{C\lambda^2}\right\} \sin(C\lambda^2) \ . \qquad (51)$$

Thus, the depolarization ratio (ξ) can be expressed as the transcendental equation

$$\xi = \{P_{21.1}/P_{10.4}\} = \left\{\frac{\lambda^2_{10.4}}{\lambda^2_{21.1}}\right\}\left\{\frac{\sin(C\ \lambda^2_{21.1})}{\sin(C\ \lambda^2_{10.4})}\right\} \ . \qquad (52)$$

If it is assumed that the longitudinal component of the magnetic field is approximately equal to the transverse component ($B_L = H$), then all of the quantities in Equation (52) are known except N_{th} and an estimate of the thermal electron density in the objects under study may be obtained. Of the many solutions, only the minimum is of interest. Table XLII contains examples of the minimum solution for N_{th} for several points on both 3C10 and 3C58.

TABLE XLII. Minimum Values for N_{th}

Position (E/W,N/S)	Source	Depol. (ξ)	L (cm)	H (gauss)	N_{th}(min) (cm^{-3})
-0.5,+3.5	3C10	.3	$2.6 * 10^{19}$	$1.6 * 10^{-4}$	.05
+0.0,-3.5	3C10	.3	$2.6 * 10^{19}$	$1.6 * 10^{-4}$	.05
+2.0,+0.5	3C10	.3	$1.4 * 10^{19}$	$2.5 * 10^{-4}$	.05
-4.0,+0.0	3C10	.5	$2.6 * 10^{19}$	$3.3 * 10^{-4}$	.02
-2.5,-2.5	3C10	.2	$1.9 * 10^{19}$	$3.0 * 10^{-4}$	.04
+2.5,+0.0	3C58	.6	$2.1 * 10^{19}$	$2.1 * 10^{-4}$	.03
-1.0,+1.5	3C58	.5	$2.0 * 10^{19}$	$1.8 * 10^{-4}$	.05
-3.0,+0.5	3C58	.6	$1.8 * 10^{19}$	$2.6 * 10^{-4}$	.03
+0.0,-1.0	3C58	.7	$2.3 * 10^{19}$	$2.0 * 10^{-4}$	.03
-1.5,+0.5	3C58	.4	$2.3 * 10^{19}$	$2.1 * 10^{-4}$	.04

Additionally, it can be seen that Equation (51) is a multivalued function with a maximum solution. Taking the absolute upper limit case of $p = 1$, $\sin(C\lambda^2) = 1$ gives

$$P_\lambda = (1/C\lambda^2) \tag{53}$$

which can be solved for $N_{th}(max)$. Calculating these values from the 21.1 cm data for the same points yields the results shown in Table XLIII.

TABLE XLIII. Maximum Values for N_{th}

Position (E/W,N/S)	Source	$P_{21.1}$	$N_{th}(max)$ (cm^{-3})
-0!5,+3!5	3C10	.024	.9
+0!0,-3!5	3C10	.029	.7
+2!0,+0!5	3C10	.028	.9
-4!0,+0!0	3C10	.056	.2
-2!5,-2!5	3C10	.020	.8
+2!5,+0!0	3C58	.106	.2
-1!0,+1!5	3C58	.055	.4
-3!0,+0!5	3C58	.080	.2
+0!0,-1!0	3C58	.055	.3
-1!5,+0!5	3C58	.028	.6

Equation (50) can also be solved for the Faraday rotation imparted to the radiation by the source. The result ($\frac{1}{2}C = 1.31 * 10^{-13} L N_{th} B_L$) amounts to approximately 10 rad m^{-2} for $N_{th}(min)$ and 100 rad m^{-2} for $N_{th}(max)$. Thus, it is possible, with this model, to have at least part of the observed Faraday rotation arise within the source itself.

CHAPTER VIII

FINALE

Comparisons

An attempt was made to compare the present work with the theories of supernova remnants. There are four principle papers in this area.

Shklovsky [81] discusses supernova remnants in some detail, but only of Type II, and requires optical observations for quantitative calculations. Van der Laan [82] postulates emission from electrons trapped in the interstellar medium compressed by the explosion. However, this theory does not apply to young sources and the effect is probably negligible in Type I supernova remnants.

A predicted secular decrease of the integrated flux density of a remnant due to the adiabatic expansion of a filled spherical volume of relativistic particles and magnetic fields by Shklovsky [83] was strikingly substantiated for Cassiopeia A. Unfortunately, this is a temporal effect about which there is insufficient information for 3C10 and 3C58.

A partial comparison can be made to the theory by van der Laan [84] for young shell sources in which the radio radiation arises from a relativistic particle flux generated within the supernova remnant and trapped in the magnetic field formed by compression of the interstellar medium. The theory predicts

$$B \simeq \frac{(1 + 4\bar{\varepsilon})^{1/2}}{2\bar{\varepsilon}} B_o \text{ gauss}$$

$$V_p \simeq \left(\frac{1 + 5\bar{\varepsilon}}{6\bar{\varepsilon}^2}\right)^{1/2} \frac{B_o}{(4\pi\rho_o)^{1/2}} \text{ cm sec}^{-1}$$

$$T \simeq \frac{r}{4V_p} \text{ sec} \qquad (54)$$

where B is the magnetic field strength in the shell, B_o is the magnetic field strength in the interstellar medium, r is the inner radius of the envelope, Δr is the thickness of the shell, $\bar{\varepsilon}$ is the fractional thickness of the shell ($\bar{\varepsilon} = \Delta r/r$), ρ_o is the density of the interstellar medium, V_p is the shell expansion velocity, and T is the age of the source.

For our shell source 3C10, $B \simeq 2 * 10^{-4}$ gauss and $r \simeq 5.2$ pc. Assuming, as did van der Laan, that the interstellar density is approximately one proton per cm^3 ($\rho_o = 1.66 * 10^{-24}$ gm cm^{-3}) and using a shell thickness of $\bar{\varepsilon} = 1/4$ yields

$$\begin{aligned} B_o &= 71 * 10^{-6} \text{ gauss} \\ V_p &= 380 \text{ km sec}^{-1} \\ T &= 3300 \text{ years} \quad . \end{aligned} \qquad (55)$$

A lower value for the interstellar density used earlier of 10^{-1} protons per cm^3 with the same shell thickness lowers the estimated source age to $T = 1040$ years.

Since the age of 3C10 is known to be 400 years and the greatest Galactic magnetic field yet measured is approximately $20 * 10^{-6}$ gauss [85],[86], the agreement with the theory is poor. However, due to the roughness of the calculations, it cannot be discarded on this basis.

Conclusions

3C10 (Tycho's supernova; S. N. 1572) is the remnant of a Type I supernova 5000 pc distant and 124 pc above the Galactic plane. The total radiation has an annular structure with a sharp outer edge and little emission from the central regions. The polarized flux density has a similar, although less complete, ring-like shape and, although the integrated emission shows little polarization, many areas are polarized in excess of 5% at 21.1 cm and 10% at 10.4 cm. The spectral index distribution shows little positional dependence, but in most areas is quite steep. The rotation measure ranges from -6 to +60 rad m^{-2} with no obvious positional organization. The intrinsic position angle distribution implies the existence of a radial component to the magnetic field. The depolarization distribution is seemingly random.

Using a source model of a uniformly filled spherical shell 13.2 pc in diameter, the magnetic field averaged along the line-of-sight is estimated to be of the order of $5 * 10^{-4}$ gauss and the averaged total relativistic electron density to be in the range 10^{-5} to $10^{-8} cm^{-3}$. From these estimates, the total relativistic particle energy is calculated to be $8.8 * 10^{49}$ ergs and the total relativistic particle mass to be $1.5 * 10^{-3} M_{\odot}$. A search for relations among the various source parameters failed to reveal any strong correlations.

3C58, on the basis of the present work, is thought to be the remnant of a Type I supernova 5000 pc distant lying 269 pc above the Galactic plane. Its structure in the total radiation is a simple shape, brightest in the center and falling off slowly to zero on the edges

with an east-west elongation. The polarized emission distribution is quite complex with some possibly unresolved regions. Although the source has little integrated polarization, when resolved, many regions exhibit polarizations exceeding 10% at 21.1 cm and 15% at 10.4 cm. The spectral index distribution over the source shows a slight tendency for the spectral index to be flat in the central and south-central regions and steeper towards the edges. The rotation measure changes smoothly from -67 rad m^{-2} in the eastern region to -125 rad m^{-2} in the western region. The intrinsic position angle distribution implies an organized component of the magnetic field parallel to the major east-west axis over the full extent of the source. The depolarization distribution is seemingly random.

Using a uniformly filled prolate spheroidal model with major and minor diameters of 13.1 and 8.0 pc, respectively, the magnetic field averaged along the line-of-sight is estimated to be of the order of $2 * 10^{-4}$ gauss and the averaged relativistic electron density to be $10^{-8} cm^{-3}$. These estimates yield a total relativistic particle energy of $1.7 * 10^{49}$ ergs and a total relativistic particle mass of $1.5 * 10^{-5} M_{\odot}$. Again, no strong correlations could be found between the various source parameters.

For both 3C10 and 3C58, the possible origins of Faraday rotation and depolarization were discussed and a model was advanced for the depolarization mechanism. From this model, the thermal electron density in the sources is estimated to be of the order of 0.1 cm^{-3}.

An attempt to compare the results of the present study with the current theories of supernova remnants was largely unsuccessful.

REFERENCES

1. Mayer, C. H., McCullough, T. P. and Sloanaker, R. M., Astrophys. J. 126, 468 (1957).

2. Mayer, C. H., McCullough, T. P., and Sloanaker, R. M., Astrophys. J. 135, 656 (1962).

3. Morris, D., Radhakrishnan, V., and Seielstad, G. A., Astrophys. J. 139, 560 (1964).

4. Seielstad, G. A., Astrophys. J. 147, 24 (1967).

5. Branson, N. J. B. A., Nature 213, 1211 (1967).

6. Downs, G. S. and Thompson, A. R., Astrophys. J. 152, L65 (1968).

7. Morris, D. and Whiteoak, J. B., Australian J. Phys. 21, 475 (1968).

8. Seielstad, G. A. and Weiler, K. W., Astrophys. J. 154, 817 (1968).

9. Seielstad, G. A. and Weiler, K. W., Astrophys. J. Suppl. 18, No.158 (1969).

10. O'Brien, P. A., Monthly Notices Roy. Astron. Soc. 113, 597 (1953).

11. Ryle, M., Nature 194, 517 (1962).

12. Morris, D., Radhakrishnan, V., and Seielstad, G. A., Astrophys. J. 139, 551 (1964).

13. Read, R. B., Trans. Inst. Radio Engrs. AP-9, 31 (1961).

14. Moffet, A. T., Astrophys. J. Suppl. VII, No. 67 (1962).

15. Korchak, A. A. and Syrovatskii, S. I., Soviet Astronomy A.J. 5, 678 (1962).

16. Ginzburg, V. L. and Syrovatskii, S. I., The Origin of Cosmic Rays (New York: The Macmillan Company, 1964), pp. 53-115.

17. Legg, M. P. C. and Westfold, K. C., Astrophys. J. 154, 499 (1968).

18. Ryle, M. and Smith, F. G., Nature 162, 462 (1948).

19. Brown, R. H., Palmer, H. P., and Thompson, A. R., Monthly Notices Roy. Astron. Soc. 115, 487 (1955).

20. Mayer, C. H., Hollinger, J. P., and Allen, P. J., Astrophys. J. 137, 1309 (1963).

21. Mayer, C. H. and Hollinger, J. P., Astrophys. J. 151, 53 (1968).

22. Seielstad, G. A. and Weiler, K. W., Astron. J. 73, 1 (1968).

23. Fomalont, E. B., Astrophys. J. Suppl. 15, No. 138 (1968).

24. Maltby,P. and Moffet, A. T., Astrophys. J. Suppl. VII, No. 67 (1962).

25. Pauliny-Toth, I. I. K., Wade, C. M., and Heeschen, D. S., Astrophys. J. Suppl. XIII, No. 116 (1966).

26. Day, G. A., Shimmins, A. J., Ekers, R. D., and Cole, D. J., Australian J. Phys. 19, 35 (1966).

27. Shimmins, A. J., Day, G. A., Ekers, R. D., and Cole, D. J., Australian J. Phys. 19, 837 (1966).

28. Bolton, J. G., Gardner, F. F., and Mackey, M. B., Australian J. Phys. 17, 340 (1964).

29. Bartlett, J. F., Private Communication, 1967.

30. Kellermann, K. I., Private Communication, 1967.

31. Kellermann, K. I., Astron. J. 69, 205 (1964).

32. Conway, R. G., Kellermann, K. I., and Long, R. J., Monthly Notices Roy. Astron. Soc. 125, 261 (1962).

33. Seielstad, G. A. and Wilson, R. W., Nature 198, 274 (1963).

34. Seielstad, G. A., Morris, D., and Radhakrishnan, V., Astrophys. J. 138, 602 (1963).

35. Morris, D. and Berge, G. L., Astron. J. 69, 641 (1964).

36. Bologna, J. M., McClain, E. F., Rose, W. K., and Sloanaker, R. M., Astrophys. J. 142, 106 (1965).

37. Gardner, F. F. and Davies, R. D., Australian J. Phys. 19, 441 (1966).

38. Maltby, P. and Seielstad, G. A., Astrophys. J. 144, 216 (1966).

39. Sastry, Ch. V., Pauliny-Toth, I. I. K., and Kellermann, K. I., Astron. J. 72, 230 (1967).

40. Fomalont, E. B., Private Communication, 1967.

41. Bracewell, R. N., Proc. Inst. Radio Engrs. 46, 97 (1958).

42. Fomalont, E. B., Publications of the Owens Valley Radio Observatory 1, No. 3 (1967).

43. Bracewell, R. N., The Fourier Transform and Its Applications (New York: McGraw-Hill Book Company, 1965), p. 111.

44. Baldwin, J. E., Radio Astronomy and the Galactic System (I.A.U. Symposium No. 31), ed. Hugo van Woerden (New York: Academic Press, 1967), p. 337.

45. Mulhall, B. D., Private Communication, 1969.

46. Kellermann, K. I., Pauliny-Toth, I. I. K., and Williams, P. J. S., Astrophys. J. 157, 1 (1969).

47. Hobbs, R. W. and Haddock, F. T., Astrophys. J. 147, 908 (1967).

48. Hobbs, R. W. and Hollinger, J. P., Astrophys. J. 154, 423 (1968).

49. Hollinger, J. P. and Hobbs, R. W., Astrophys. J. 151, 771 (1968).

50. Gardner, F. F. and Whiteoak, J. B., Astrophys. J. 154, 807 (1968).

51. Maltby, P., Astrophys. J. 144, 219 (1966).

52. Brown, R. H. and Hazard, C., Nature 170, 364 (1952).

53. Minkowski, R., Paris Symposium on Radio Astronomy (I.A.U. Symposium No. 9), ed. R. N. Bracewell (Stanford: Stanford University Press, 1959), p. 315.

54. Minkowski, R., Nebulae and Interstellar Matter (Stars and Stellar Systems Vol. VII), ed. B. M. Middlehurst and L. H. Aller (Chicago: University of Chicago Press, 1968), p. 623.

55. Menon, T. K., and Williams, D. R. W., Astron. J. 71, 392 (1966).

56. Reifenstein, E. C. III, Brundage, W. D., and Staelin, D. H., Astrophys. J. 156, L125 (1969).

57. Higgs, L. A. and Ramana, K. V. V., Astrophys. J. 154, 73 (1968).

58. Horton, P. W., Conway, R. G., and Daintree, E. J., Monthly Notices Roy. Astron. Soc. 143, 245 (1969).

59. Fomalont, E. B., Obs. of the Owens Valley Radio Observatory 3 (1969).

60. Kesteven, M. J. L., Australian J. Phys. 21, 739 (1968).

61. Poveda, A. and Woltjer, L., Astron. J. 73, 65 (1968).

62. Milne, D. K. and Hill, E. R., Australian J. Phys. 22, 211 (1969).

63. Minkowski, R., Annual Review of Astronomy and Astrophysics (Vol. 2), ed. Leo Goldberg (Palo Alto: Annual Reviews Inc., 1964), p. 247.

64. Shklovsky, I. S., Soviet Astronomy A.J. 4, 355 (1960).

65. Ryle, M., Elsmore, B. and Neville, A. C., Nature 205, 1259 (1965).

66. Ginzburg, V. L. and Syrovatskii, S. I., Annual Review of Astronomy and Astrophysics (Vol. 3), ed. Leo Goldberg (Palo Alto: Annual Reviews Inc., 1965), p. 297.

67. Burbidge, M. E. and Burbidge, G. R., Paris Symposium on Radio Astronomy (I.A.U. Symposium No. 9), ed. R. N. Bracewell (Stanford: Stanford University Press, 1959), p. 323.

68. Shklovsky, I. S., Supernovae (New York: John Wiley and Sons Ltd., 1968), pp. 1-20.

69. Gardner, F. F. and Whiteoak, J. B., Annual Review of Astronomy and Astrophysics (Vol. 4), ed. Leo Goldberg (Palo Alto: Annual Reviews Inc., 1966), p. 245.

70. Gardner, F. F. and Davies, R. D., Australian J. Phys. 19, 129 (1966).

71. Seielstad, G. A., Morris, D., and Radhakrishnan, V., Astrophys. J. 140, 53 (1964).

72. Gardner, F. F. and Whiteoak, J. B., Nature 197, 1162 (1963).

73. Smith, F. G., Nature 220, 891 (1968).

74. Radhakrishnan, V., Cooke, D. J., Komesaroff, M. M., and Morris, D., Nature 221, 443 (1969).

75. Ekers, R. D., Lequeux, J., Moffet, A. T., and Seielstad, G. A., Astrophys. J. 156, L21 (1969).

76. Milne, D. K., Australian J. Phys. 21, 201 (1968).

77. Davies, R. D., Nature 218, 435 (1968).

78. Bologna, J. M., McClain, E. F., and Sloanaker, R. M., Science 154, 1656 (1966).

79. Bologna, J. M., McClain, E. F., and Sloanaker, R. M., Astrophys. J. 156, 815 (1969).

80. Burn, B. F., Monthly Notices Roy. Astron. Soc. 133, 67 (1966).

81. Shklovsky, I. S., Soviet Astronomy A. J. 6, 162 (1962).

82. van der Laan, H., Monthly Notices Roy. Astron. Soc. 124, 125 (1962).

83. Shklovsky, I. S., Soviet Astronomy A. J. 4, 243 (1960).

84. van der Laan, H., Monthly Notices Roy. Astron. Soc. 124, 179 (1962).

85. Verschuur, G. L., Phys. Rev. Lett. 21, 775 (1968).

86. Davies, R. D., Booth, R. S., and Williams, A. J., Nature 220, 1207 (1968).

87. Elsmore, B., Kenderdine, S., and Ryle, M., Monthly Notices Roy. Astron. Soc. 134, 87 (1966).

88. Kenderdine, S., Ryle, M., and Pooley, G. G., Monthly Notices Roy. Astron. Soc. 134, 189 (1966).

89. Macdonald, G. H., Kenderdine, S., and Neville, Ann. C., Monthly Notices Roy. Astron. Soc. 138, 259 (1968).